On the effects of nozzle spacing ratio on statistical properties of twin low-aspect-ratio rectangular jets

by

Ramin Naseri Oskouie

A Thesis submitted to the Faculty of Graduate Studies of

The University of Manitoba

in partial fulfillment of the requirements of the degree of

DOCTOR OF PHILOSOPHY

Department of Mechanical Engineering

University of Manitoba

Winnipeg, Manitoba, Canada

Abstract

An experimental study was performed to investigate the effects of the spacing ratio between the nozzles on evolution and interaction of twin rectangular jets. The velocity measurements were conducted using particle image velocimetry (PIV) technique. The measurements were performed on the symmetry plane of the rectangular jets. A total of 5 test cases of S/d_e = 1.8, 2.8, 3.7, 5.5 and 7.3 were examined with Reynolds number being fixed and equal to Re_{de} = 10,000. The effects of the spacing ratio on the mean flow in terms of its mixing characteristics (*e.g.*, decay and spread rates) and turbulence statistics (*e.g.*, turbulence intensities and Reynolds stresses) were investigated. The focus was then on large-scale structures (LSS). The evolution of LSS was studied along the shear layers and the symmetry line in order to investigate the effects of nozzle spacing and interactions. For doing so, various techniques such as Galilean decomposition, two-point correlation and swirling strength were applied on the flow field. The conditionally-averaged mean streamwise velocity profiles were also extracted around the turbulent/non-turbulent interface (TNTI) and results were compared with twin round jet counterpart.

The results showed that changing the spacing ratio directly affects some characteristics of the mean flow, turbulence statistics and LSS. For instance, it was observed that increasing the spacing ratio, linearly increases the streamwise locations of the merging and combined points though with different slopes. Turbulence intensity profiles along the symmetry line showed a peak downstream of the merging point, where its value decreased as the spacing ratio increased. Also, interestingly for $S/d_e \leq 3.7$, the peak of the transverse component was larger than the streamwise component. Regarding the integral length scale of turbulence along the symmetry line, a linearly increasing trend was observed. Whilst no effects of nozzle spacing was observed on the streamwise

component, the trend for the transverse component showed to increase by increasing the spacing ratio.

Due to the importance of the shear layers in free shear flows, a special attention was paid to the inner and outer shear layers. In the converging region, jet half-velocity widths were identical for the shear layers. In the merging region however, while the outer shear layer continued to spread similarly to its single jet counterpart, the half-velocity width of the inner shear layer rapidly increased before becoming unstable by the interactions. Study of coherent structures showed that the effects of interactions become more pronounced as the inner shear layer develops in the merging region. For instance, $0.1d_e$ downstream of the merging point, the streamwise spatial correlation of the outer and inner shear layers were identical. By progressing into the merging region however, this reduced for the inner shear layer while expectedly increased for the outer shear layer. In a similar fashion, at the TNTI the difference between conditionally- and unconditional- averaged profiles of mean streamwise velocity increased as the inner shear layer developed in the merging region. As a result, the conditional profile jumped to a larger value upon entering the turbulent region.

Acknowledgment

I would like to express my sincere and warm gratitude to my supervisors, Dr. Tachie and Dr. Wang, for their continuous support of my Ph.D. study and research, and for their patience and encouragement.

To my committee, Dr. Ghaemi, Dr. Dow and Dr. Kuhn, I am profoundly grateful for your suggestions and feedback throughout my project.

Special Thanks to my brother and sister, Shahin and Nassim, and my friends for their unconditional support and love during this time.

I am more than grateful to have my partner, Mahdis Ghorbanzade, beside me during this time. She was and is the one who dedicated all her support and love and helped me overcome the challenges I faced along the way.

Last but not least, I dedicate my thesis to my parents, Shahin and Masoud. It was through their sacrifices and self-devotion that I could achieve to the highest level of academic education.

Contents

List of Figures

List of Tables

Nomenclature

English symbols

A	Amplitude
a_j^{in}	Slope of the jump profiles of the inner shear layer with respect to streamwise distance
a_{xuu_I}	Slope of longitudinal integral length scale along the inner shear layer
a_{xuu_O}	Slope of longitudinal integral length scale along the outer shear layer
a_{xuu_S}	Slope of longitudinal integral length scale along the symmetry line
a_{yvv_I}	Slope of transverse integral length scale along the inner shear layer
a_{yvv_O}	Slope of transverse integral length scale along the outer shear layer
a_{yvv_S}	Slope of transverse integral length scale along the symmetry line
B	Biased error
C_s	Geometric virtual origin
C_x^*	Mean convection along the streamwise direction
C_y^*	Mean convection along the transverse direction
d	Nozzle height
d_e	Equivalent diameter
d_p	Particle diameter
d_{pitch}	Pixel pitch
E	Total error
f	Shedding frequency
f_s	Sampling frequency

g	Gravitational acceleration
$I^{x}_{uu\_I}$	Longitudinal integral length scale along the inner shear layer
$I^{x}_{uu\_O}$	Longitudinal integral length scale along the outer shear layer
$I^{x}_{uu\_S}$	Longitudinal integral length scale along the symmetry line
$I^{y}_{vv\_I}$	Transverse integral length scale along the inner shear layer
$I^{y}_{vv\_O}$	Transverse integral length scale along the outer shear layer
$I^{y}_{vv\_S}$	Transverse integral length scale along the symmetry line
k	Turbulence kinetic energy
K_s	Spreading rate
K_u	Decay rate
L_0	length of the camera view in the plane object
L_i	width of the digital image
l_0	Characteristic length scale
M_f	Magnification factor
N	Sample size
P	Precision error
p	Pressure fluctuations
Q_1	First quadrant
Q_2	Second quadrant
Q_3	Third quadrant
Q_4	Forth quadrant
R	Radius of the trajectory of centerline

R_{uu}^{x}	Correlation of streamwise velocity fluctuation along the streamwise direction
R_{vv}^{y}	Correlation of transverse velocity fluctuation along the transverse direction
R_{uv}^{x}	Cross-correlation coefficient in the streamwise direction
R_{uv}^{y}	Cross-correlation coefficient in the transverse direction
S	Spacing between nozzles
S_f	Scale factor
s_{in}	Slope of the quasi-linear region
t	Exponential decay rate
u	Streamwise velocity fluctuations
u_0	Characteristic velocity
U^*	Normalized conditionally-averaged mean streamwise velocity
U_{cl}	Centerline mean streamwise velocity
U_{conv}	Convection velocity
U_e	Jet exit velocity
U_{ins}	Instantaneous streamwise velocity
U_m	Local maximum streamwise mean velocity
U_{max}	Maximum mean streamwise velocity
U_{sym}	streamwise mean velocity along the symmetry line
u_{rms}	Streamwise turbulence intensity
u_{rms_c}	Streamwise turbulence intensity along the centerline
u_{rms_s}	Streamwise turbulence intensity along the symmetry line
u_s	Settling velocity
v	Transverse velocity fluctuations

v_{rms}	Transverse turbulence intensity
v_{rms_c}	Transverse turbulence intensity along the centerline
v_{rms_s}	Transverse turbulence intensity along the symmetry line
w	Nozzle width
x	Streamwise direction
x_0	Kinematic virtual origin
x_{cp}	Combined point location
x_{mp}	Merging point location
x_{pc}	Potential core length
x_{pU}	Location of maximum streamwise mean velocity along the symmetry line
x_{pu}	Location of maximum streamwise turbulence intensity along the symmetry line
x_{pv}	Location of maximum transverse turbulence intensity along the symmetry line
x_{ref}	Reference streamwise location
y	Transverse direction
y^*	Normalized transverse direction
y_i	Transverse location of the turbulent/non-turbulent interface
$y_{0.5}^-$	Jet half velocity-width along the inner shear layer
$y_{0.5}^+$	Jet half velocity-width along the outer shear layer
y_{cl}	Transverse location of the jet centerline
y_{ref}	Reference transverse location
z	Spanwise direction
Z_c	Confidence coefficient
$\langle u^2 \rangle$	Streamwise Reynolds normal stress

$\langle v^2 \rangle$	Transverse Reynolds normal stress
$\langle uv \rangle$	Reynolds shear stress

Greek symbols

ν	Kinematic viscosity
Δt	Time between pulses
ΔU^*	Jump value of conditionally-averaged mean streamwise velocity
Δx	Streamwise spatial separation
Δy	Transverse spatial separation
ρ_f	Density of the fluid
ρ_p	Density of particles
μ_f	Viscosity of fluid
τ_r	Response time
τ_f	fluid characteristics time scale
λ	Wave length
θ	sensitivity coefficient
ε_U	precision error for streamwise mean velocity
ε_V	precision error for transverse mean velocity
$\varepsilon_{u_{rms}}$	precision error for streamwise turbulence intensity
$\varepsilon_{v_{rms}}$	precision error for transverse turbulence intensity
$\varepsilon_{<uv>}$	precision error for Reynolds shear stress
ω_z	Spanwise mean vorticity
σ_u	Root-mean-square value of streamwise velocity fluctuations

σ_v	Root-mean-square value of transverse velocity fluctuations
λ_{eg}	Eigenvalue of velocity gradient tensor in x-y plane
λ_{ci}	Swirling strength
λ_{ci}^*	Normalized swirling strength

Acronyms

2D	Two-dimensional
AR	Aspect ratio
CCW	Counter-clockwise
CP	Combined point
CR	Contraction ratio
CW	Clockwise
FFT	Fast Fourier transform
FOV	Field of view
HVAC	Heating, ventilation and air conditioning:
HWA	Hot-wire anemometry:
IA	Interrogation area
JPDF	Joint probability density function
LISHL	Last inner shear layer location
LSS	Large-scale structures
MP	Merging point:
Nd-YAG	Neodinium-YAG
NSERC	Natural Sciences and Engineering Research Council of Canada

PIV	Particle image velocimetry
Re	Reynolds number
SJ	Single jet
St	Strouhal number
Stk	Stokes number
TKE	Turbulence kinetic energy
TNTI	Turbulent/non-turbulent interface

Chapter 1

Introduction and objectives

1.1. Introduction

Turbulent free jets have been studied extensively due to their diverse engineering applications and importance for advancing fundamental understanding of turbulent free shear flows. One can find applications of free jets in heating, ventilation and air conditioning (HVAC) systems, heat transfer and mixing and dissipation of the jet into the ambient. In some of these applications, the need of reduced noise level and mixing of two or more fluids necessitates the use of jets produced from two or more nozzles parallel to each other in order to achieve the desired objective. In this case, the twin or multiple jets interact with each other as they develop downstream. The interaction among these jets will result in a more complicated flow field and transport phenomena, when compared with their single jet counterpart. Furthermore, the degree of complexity and details of the flow characteristics are strongly dependent on initial conditions of the individual jets such as nozzle geometry, nozzle type as well as such parameters as the spacing between the nozzles and the jets velocity ratios [1–3].

Two parallel jets produced from identical nozzles with similar exit conditions are the simplest form of multiple jets. In spite of their relative simplicity, research on twin jets and their inherent complex interaction will provide important insight into the mixing characteristics and turbulent transport phenomena of multiple jets, and to evaluate how the transport processes and flow structure in multiple jets differ from a single jet. Nonetheless, the current understanding of twin jets is deficient compared to single jets owing in part to the comparatively fewer investigations on twin parallel jets compared to free single jets.

A schematic of twin jets revealing some of their salient features and Cartesian coordinate system adopted in this research is shown in Fig. 1-1. The streamwise and transverse directions are denoted by x and y, respectively. The mean and fluctuating velocities in these directions are also U and u and V and v, respectively. In this figure, S and d, respectively, denote the center-to-center distance of the nozzles and width of each nozzle. The existence of the inner and outer shear layers is the result of the velocity gradient between the high-momentum jets and the ambient fluid. The inner shear layers converge toward each other due to jet spreading. As a consequence, they meet at the so-called "merging point" (MP), located on the symmetry line, and the region from the nozzle exit to the MP is referred to as the "converging region". In this region, the spread of the inner and outer shear layers at a given streamwise location is measured using the half-velocity width, defined as the distance from the symmetry line to the position where the mean velocity is one-half the local maximum, U_m. As shown in Fig. 1-1, the half-velocity widths in the inner and outer shear layers are denoted as $y_{0.5}^{-}$ and $y_{0.5}^{+}$, respectively.

Downstream of the MP, the inner counter-rotating vortical structures start to interact with each other. Meanwhile, the trajectory of the local maximum velocity for each jet bends towards the symmetry line in order to compensate for the momentum deficit of the flow between the jets. As the distance from the MP increases, the transverse profile of the streamwise mean velocity transitions from a dual-peak to a single-peak pattern. The exact streamwise location where a single-peak appears in the mean velocity profile of the merged dual jets is referred to as the "combined point" (CP) and the region between the MP and the CP is referred to as the "merging region". Downstream of the CP, the characteristics of the single-peaked streamwise mean velocity profile become increasingly similar to those of a self-similar single jet. One can expect that higher-order

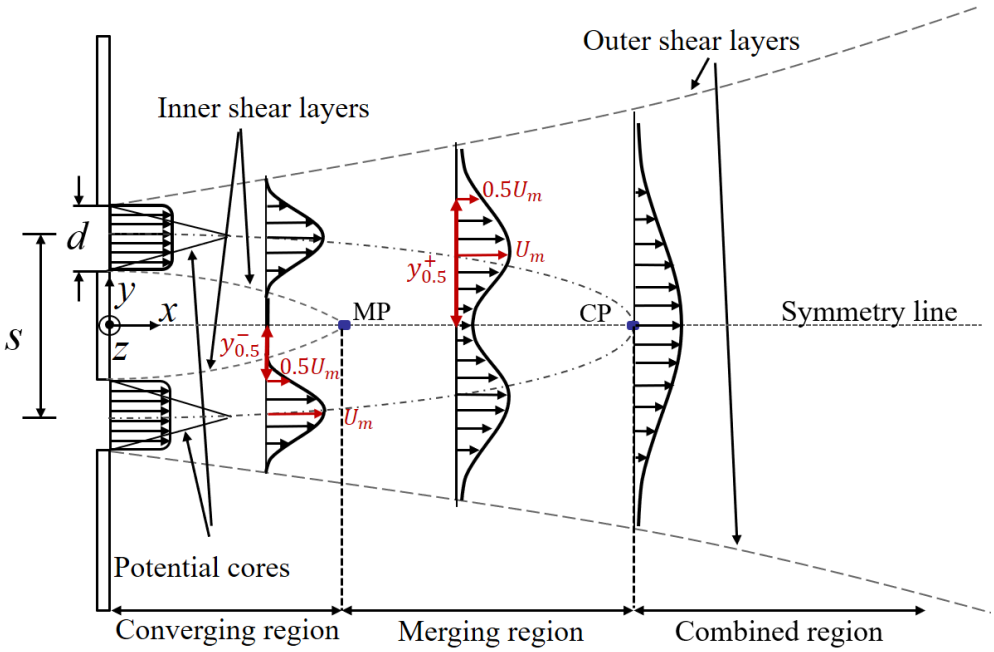

Fig. 1-1. Schematics of the flow field in twin jets.

(i.e., second and higher order) turbulence statistics will continue developing and eventually show a full resemblance to a self-similar single jet in the far downstream region [4].

The flow development and the regions discussed above are the same for two-dimensional (2D) parallel plane jets and three-dimensional (3D) twin jets, except for the converging region and the merging point. In the case of 2D parallel jets, due to the lack of fluid entrainment in the lateral direction, two recirculation zones, which are symmetric with respect to the plane of symmetry, are formed in the converging region. Therefore, negative streamwise mean velocity occurs in this region. The merging point is then defined as the streamwise location at which the streamwise mean velocity reaches zero on the plane of symmetry. For this reason, the merging point is sometimes referred to as the stagnation point in 2D parallel plane jets studies [4]. As there is no region with negative streamwise mean velocity in 3D twin jets, the merging point is defined as a streamwise location in which the mean flow on the plane of symmetry tends to accelerate [5].

1.2. Governing equations

Similar to research on other turbulent shear flows, different experimental and numerical techniques can be adopted for the study of twin jets. While there are differences between numerical and experimental approaches, all of them conform to the continuity and the Navier-Stokes (momentum) equations in order to resolve the flow field. Due to the random nature of turbulence, the averaged version of the Navier-Stokes equation is more commonly solved. In this averaged equation, which is called the Reynolds averaged Navier-Stokes (RANS) equation, the averaging introduces a new term called Reynolds stresses. This term, in three-dimension, forms a symmetric tensor. The off-diagonal components of the tensor represent the shear generated by turbulence fluctuations of any two perpendicular direction and are called Reynolds shear stresses. The diagonal components on the other hand are called Reynolds normal stresses, and their summation is the turbulent kinetic energy. Transport equations can also be derived for the Reynolds stresses and turbulent kinetic energy, tke. Eqn (1-1), Eqn (1-2), Eqn (1-3) and Eqn (1-4) are, respectively, the continuity (conservation of mass), RANS, Reynolds stresses transport and tke transport equations. In these equations, the upper case letters represent the mean flow while the lower case letters are the corresponding fluctuating velocities. Also, all of the parameters are in averaged form.

$$\frac{\partial U_i}{\partial x_i} = 0 \qquad \text{Eqn (1-1)}$$

$$U_j \frac{\partial U_i}{\partial x_j} = -\frac{1}{\rho}\frac{\partial P}{\partial x_i} + \frac{\partial}{\partial x_j}\left(\nu \frac{\partial U_i}{\partial x_j} - \overline{u_i u_j}\right) \qquad \text{Eqn (1-2)}$$

$$U_k \frac{\partial \overline{u_\iota u_J}}{\partial x_k} = -\left(\overline{u_\iota u_k}\frac{\partial U_j}{\partial x_k} + \overline{u_J u_k}\frac{\partial U_i}{\partial x_k}\right) + \overline{\frac{p}{\rho}\left(\frac{\partial u_i}{\partial x_j} + \frac{\partial u_j}{\partial x_i}\right)} - 2\nu\overline{\frac{\partial u_\iota}{\partial x_k}\frac{\partial u_J}{\partial x_k}} + \quad \text{Eqn (1-3)}$$

$$\frac{\partial}{\partial x_k}\left(\nu\frac{\partial \overline{u_\iota u_J}}{\partial x_k} - \overline{u_\iota u_J u_k} - \frac{1}{\rho}\left[\overline{pu_\iota}\delta_{jk} + \overline{pu_J}\delta_{ik}\right]\right)$$

$$U_j \frac{\partial k}{\partial x_j} = -\overline{u_\iota u_J}\frac{\partial U_i}{\partial x_j} - \frac{\partial}{\partial x_j}\left[\frac{1}{\rho}\overline{u_J p} + \frac{1}{2}\overline{u_J u_\iota u_\iota} - \nu\frac{\partial k}{\partial x_j}\right] - \nu\overline{\frac{\partial u_\iota}{\partial x_J}\frac{\partial u_\iota}{\partial x_J}} \quad \text{Eqn (1-4)}$$

1.3. Research motivation and objectives

Twin turbulent jets were shown to play an important role in several engineering applications. Yet they have not been studied as extensive as free single jets, due to various complications they introduce. For instance, the inner mixing of the jets, downstream of the MP is a complex non-linear momentum transport process between two initially turbulent free shear flows which is totally absent in a free single jet.

Despite the fundamental and remarkable studies, which will be discussed in details, the following chapter will show that there is still room to add to our understanding of twin jets both in terms of the mean flow and turbulence structures. For such, nozzle spacing effects can be a candidate as it directly affects the location of the MP [1]. In other words, changing the spacing ratio in some sense advances or retards the momentum transport process between the jets. On the other hand, as the MP can lie within different regions of individual jets (*i.e.* potential core, transition and self-similar regions), changing the spacing ratio can also affect the mechanisms involved in momentum transport process in the merging region. These two examples emphasize the importance of initial spacing between the jets on their far-field development and mixing. The topic is hence of interest in the study of twin jets.

The literature review in the next chapter shows that, the majority of the studies have brought their focus on the case of 2D parallel plane jets. These jets are produced by two slots that have the

length of the test section. The confinement of the side walls then prevents the jets from spreading in the lateral direction. As an outcome, the jets can only spread in the transverse direction. More importantly, due to lack of entrainment of ambient fluid into the space between the jets in the converging region, a recirculation region forms between the jets' inner shear layers. In a 3D twin-jet case, this negatively-pressurized region is absent, as the converging region is exposed to the entrainment from its surroundings. It is clear that the impact of the existence/lack of such a region on flow physics is too greater to ignore. In other words, not only the mean flow, but also the turbulence structures can develop in totally different ways in the cases of 2D and 3D twin jets.

To address the shortcomings and issues discussed in the above paragraphs, in the present research, twin rectangular jets with low aspect-ratio have been selected. The objectives of the research are as follow:

a) A basic understanding on the evolution of twin rectangular jets
b) A systematic investigation on the effects of the spacing ratio between the nozzles on:
    - The mean flow characteristics such as merging and combined points, decay and spread rates
    - Turbulence statistics such as turbulence intensities and Reynolds stresses
    - Large-scale coherent structures both qualitatively and quantitatively, by the means of various eduction methods (Galilean decomposition, two-point correlation, swirling strength, *etc.*)
c) Comparison of flow physics along the inner and outer shear layers specially in the merging region where the inner shear layer is exposed to interactions and the outer shear layer is freely developing
d) Comparing the results with the literature on free single jet as well as twin round jets

e) Providing a benchmark for future experimental and numerical studies

1.4. Organization of the thesis

Following the "sandwich" style, this thesis is comprised of two journal papers (one of them has been published and the other one is under review) and organized in six chapters. The introduction, motivations and objectives of the present study were provided in this chapter. In chapter 2, a detailed literature review of previous studies on 2D and 3D twin jets is presented. The experimental setup, including details on the test facility, flow measurement technique and test conditions, is presented in chapter 3. The first paper is included in chapter 4. In this paper preliminary results on the effects of nozzle spacing ratio on the mean flow, and second order turbulence statistics are provided and discussed. The contributions of this paper are:

- Extracting the locations of the MP and CP and investigating their relationship with spacing ratio.
- Studying the mean flow in terms of decay and spread rates as well as momentum flux.
- Providing normalization parameters to remove the spacing effect from mean streamwise velocity profiles along the symmetry line.
- Studying the progress of 1D mean streamwise velocity, turbulence intensities and Reynolds shear stress profiles across the jet, and their development towards a self-similar single jet profile in the combined region.
- Investigating nozzle spacing effects on suppression of Reynolds shear stress along the inner shear layer.

The second paper is provided in chapter 5. In this paper, more detailed analyses regarding twin jets and nozzle spacing effects are discussed. The focus of the paper is on coherent structures.

Various techniques such as two-point correlation, swirling strength and joint probability density function (JPDF) are adopted to achieve the objective of the paper. Also, an innovative technique is applied to investigate the turbulent/non-turbulent interface (TNTI). The contributions of this paper are as follow:

- Qualitative study of vortices behavior through swirling strength and Galilean decomposition.
- Investigating the effects of nozzle spacing and interactions on spatial correlation of Reynolds stresses.
- Thorough study on the size of integral length scale along outer and inner shear layers as well as the symmetry line.
- Providing insight on the contribution of events (*i.e.* ejection, sweep, and entrainment) on production of Reynolds shear stress at different flow regions.
- Studying the suppression of inner shear layer vortices through 1D profiles of swirling strength at various streamwise locations, covering converging and merging regions.
- Extracting the interface location along the outer and inner shear layers through TNTI detection technique.
- Studying the conditionally-averaged mean streamwise velocity profiles around the interface.

The conclusion of the research as well as suggestions for future work are provided in chapter 6. In Appendix A, spatial resolution and convergence tests results are provided. In Appendix B, the uncertainty estimates are discussed. This includes the biased and precision errors as well as the total error of the experiment. Due to brevity, some results were not provided in the second journal publication. These can be found in Appendix C.

Chapter 2

Literature review

2.1. Overview

In this chapter a detailed literature review on twin jets is provided. In order to maintain consistency and provide a coherent review on the available literature, this chapter consists of two subsections. In line with the first objective of the present study, the first subsection reviews the previous literature on the effect of nozzle spacing ratio on flow characteristics. More specifically, this subsection first provides literature review on 2D twin jets and then discusses the available literature on 3D twin jets. In order to update the state of knowledge on the second objectives of the study, in the second subsection, the literature is reviewed based on the similarities and/or contrasts that were observed between twin and single jets.

2.2. Nozzle spacing effects

Tanaka [1, 6] investigated the effect of nozzle spacing for S/d = 8.5, 10, 12, 14, 16, 18, 20 and 25 at Re_d = 4290 – 8750. In the converging region, the curvature of the jets and the merging point location as well as decay and spread rates showed two different trends for $S/d < 16$ and $S/d > 16$. The trajectory of local maximum velocity was located on an arc of a circle. The radius of the arc was observed to be constant and equal to R/d = 17.1 for $S/d < 16$, while for $S/d > 16$ the radius increased linearly with nozzle spacing at the rate of 1.10. It was argued that for $S/d < 16$, the merging points were located close to nozzle exit and in the developing region of the jets ($x/d <$ 10). Therefore, the convergence of the jets was severely affected by the high velocity gradient existed between individual inner shear layers and the recirculation region. For $S/d < 16$, the decay and spread rates increased as the spacing ratio was increased and for $S/d > 16$, they were nearly

independent of nozzle spacing ratio. Within the combined region ($30 < x/d < 110$), one-dimensional profiles of streamwise mean velocity showed self-similarity irrespective of nozzle spacing. For $S/d < 14$, the one-dimensional profiles of streamwise Reynolds normal stresses were independent of downstream distance although the peaks were increasing as the nozzle spacing increased. For $S/d > 14$, the peak values were increased by increasing the spacing ratio and/or the downstream distance. Similar to the observation made in the converging region, the spread and the decay rates increased by increasing nozzle spacing ratio for $S/d < 16$, while they held a constant value for $S/d > 16$.

Anderson *et al.* [7] used HWA to investigate the periodic behavior of twin parallel plane jets in the near-field region for $S/d = 1.50$, 1.63, 1.83, 2.25 and 2.67. For all of the test cases, a distinct peak in power spectrum of instantaneous velocity field was observed. The peak was attributed to bluff body shedding mode of the inner shear layer. The reduced frequency of the peak (fS/U) was observed to decrease as nozzle spacing (S/d) decreased. For instance, a 25% decrease was observed for $S/d = 1.50$ compared to $S/d = 2.67$. The authors argued that there is an asymptote for the reduced frequency as nozzle spacing approaches zero. A second peak was observed for all test cases except for $S/d = 2.67$. The existence of the second peak was attributed to the interaction between the outer shear layer mode and bluff-body shedding mode of the inner shear layer. Therefore, the difference between these two peaks was observed to increase as nozzle spacing was decreased.

In the numerical study by Spall *et al.* [8], the effect of nozzle spacing ($S/d = 3$, 5, 7, 9 and 11) on total momentum flux of twin parallel plane jets were examined by employing a standard k-ε model. As it was also reported by Tanaka [1], the total momentum flux which consists of the integral of the momentum of the mean and fluctuating velocities as well as the pressure across the

jet, is constant. However, it was shown that the integral constant decreases as the spacing increases. For instance, the integral constant for S/d = 11 was 15% lower than observed for S/d = 3.

Hsu *et al.* [9] adopted district vortex method on twin parallel plane jets for S/d =1.3, 1.7, 2 and 4. In the near-field region, a dominant frequency in streamwise turbulence fluctuations only exists for S/d = 1.7 and 2. Strouhal number corresponding to this dominant frequency was observed to be 33% lower for S/d = 1.7 compared to S/d = 2. This shows that as the nozzle spacing increases, Strouhal number increases as well. In order to confirm that the dominant frequency and subsequently the periodic behavior of vortical structures exist for only a specific range of nozzle spacing, contour plots of instantaneous streamwise fluctuating velocity was compared for S/d = 2 and 4. It was observed that only S/d = 2 showed distinct vortical structures in the neighborhood of the merging point, which proved the argument mentioned above.

A more recent numerical study by Mondal *et al.* [10] investigated the effect of nozzle spacing on coherent structures in twin parallel plane jets for S/d = 1.5, 1.6, 1.8, 2.2, 2.4 and 2.5. Similar to the findings of Hsu *et al.* [9], a periodic vortex shedding behavior was observed from the instantaneous streamlines in the recirculation region for S/d = 1.6 and 2.4. The instantaneous vorticity field also revealed the existence of counter-rotating vortices within the inner shear layers for $1.6 \leq S/d \leq 2.4$. The vortex street of the inner shear layers also destabilizes the outer shear layer vortices through Kelvin-Helmholtz (K-H) instability for $1.8 \leq S/d \leq 2.4$. The reason for the lack of K-H instability for S/d = 1.6 was attributed to the lack of strength of the von Karman vortices to destabilize the outer shear layers. In contrast to [9], it was observed that as the spacing increases, the vortices require more time to grow in size and strength in order to draw the opposite vortex before shedding away and as a consequence, the Strouhal number of the vortices decrease.

Based on the results of previous studies on twin parallel plane jets [2, 4, 11–13], and their 2D twin jet study with S/d = 3.07, Hassan and Lee [14] proposed two different trends for the location of the merging point with respect to nozzle spacing ratio. For $S/d < 3$, a non-linear power trend between the merging point and nozzle spacing was suggested in which the length of the converging region was lower than nozzle spacing. For $S/d \geq 3$, a linear trend was proposed in which the merging point location was 1.15 times of the nozzle spacing. It was argued that in the potential core region, the jets do not diverge linearly but they maintain a straight pattern. It was argued that when the jets are close to each other, the relationship between the merging point location and nozzle spacing is non-linear.

Harima *et al.* [15, 16] studied the effect of nozzle spacing on twin round jets with S/d = 2, 4 and 8 at Re_d = 25,000. Similar to the findings of Tanaka [1], Harima *et al.* [15] observed that the trajectory of the local maximum streamwise mean velocity is located on an arc of a circle, the radius of which increases with nozzle spacing. However, due to the existence of the recirculation region in the case of 2D twin jets, the length of the arc (radius of the circle) was shorter for the former compared to the latter. For instance, the radius in the study of Harima *et al.* [15] for S/d = 8 was 66 times the one in the study of Tanaka [1]. The streamwise location at which these arcs coincide on the symmetry line was considered as the combined point. Evidently the combined point location moved downstream as the nozzle spacing increased. The effect of nozzle spacing was also observed on volumetric flow rate. At any streamwise location, the volumetric flow rate was higher for larger spacing ratios. However, the increase in volumetric flow rate with respect to streamwise distance was shown to be constant and equal to the one on single jet. Regarding the location of maximum streamwise turbulence intensity along the jet centerline and the symmetry line, two opposing trends were observed. Along the jet centerline, the location of maximum

streamwise turbulence intensity was observed to move downstream by decreasing the spacing ratio. It was argued that the interactions suppress the development of the streamwise component of turbulence intensity and hence, by decreasing the spacing ratio, the location of its maximum moves further downstream. For instance, the location of the maximum decreased by 17% for S/d = 8 compared to S/d = 2. Meanwhile, it was observed that by increasing the spacing ratio the location of maximum streamwise turbulence intensity along the symmetry line increases. In here, the location of the maximum was increased by 255% in the case of S/d = 8 compared to S/d = 2.

Zang and New [17] studied the near-field region of twin round jets with small nozzle spacing ratios of S/d = 1.5, 2 and 3 at Re_d = 3,300. The contour plots of instantaneous vorticity up to x/d = 7 showed that, for S/d = 1.5 and 2, the vortical structures of the inner shear layers formed a staggered pattern of positive and negative vortices, similar to those in the wake behind a bluff body. Due to its higher spacing, the staggered pattern was not observed for S/d = 3. Frequency analysis showed one distinct peak for each of the inner and outer shear layers. For any spacing ratio, the corresponding Strouhal number for the peak frequency of the outer shear layer was St = 0.69, which was comparable to values reported for free single jets. The Strouhal number in the inner shear layer was however, observed to decrease as the spacing was decreased. This trend was in agreement with the findings of Hsu *et al.* [9]. Strouhal numbers of the inner shear layer was obtained to be St = 0.52, 0.57 and 0.59 for S/d = 1.5, 2 and 3, respectively. These results show that as the spacing increases, the inner shear layers are less confined by each other's interactions and therefore, their respective Strouhal numbers approach the one in single jet (outer shear layer). In other words, it is expected that as spacing increases, the difference between Strouhal numbers of the inner and outer shear layers decrease. A similar observation was reported by Anderson *et al.* [7]. It was argued that the lower frequency of the vortical structures in the inner shear layer

compared to the outer shear layer, which was also the case in [7], is due to the differences in mechanisms that are responsible for the formation of the vortices in the inner and outer shear layers. Proper orthogonal decomposition analysis showed that as nozzle spacing increases, the cumulative turbulence kinetic energy decreases. This was attributed to the existence of less energetic coherent structures as a result of limited interactions between the jets' inner shear layers for larger values of nozzle spacing. The reconstructed velocity vector field for mode 5 of the POD analysis provides credence to the above argument, as larger and more coherent structures within the inner shear layers were visualized for smallest spacing (S/d = 1.5) compared to the largest spacing (S/d = 3). The POD analysis also revealed that for small nozzle spacing, there exists a train of counter-rotating coherent structures within the jets' inner shear layers, which resemble the von Karman vortex street behind a bluff body. Frequency analysis on the symmetry line at x/d = 7 also showed two distinct peaks at 4.2 Hz and 2.1 Hz for S/d = 1.5. The authors attributed the first peak to vortex formation frequency of the inner shear layer as 4.2 Hz was close to 4.4 Hz reported for vortex generation frequency of the inner shear layer at nozzle exit. The second peak was, however, attributed to the shedding frequency of the inner shear layer structures, as it corresponds to St = 0.34 which is close to St = 0.24 to 0.34, reported for vortex shedding frequency of a bluff body [18].

2.3. Comparison with single jet

In their pioneering experiments, Miller and Comings [4] used hot-wire to investigate the converging and combined regions of twin parallel plane jets at Re_d = 17,800 with nozzle spacing of S/d = 6. The spread rate of the jets in the converging region was found to be K_s = 0.09, which agrees well with their single jet results [19]. The spread and decay rates in the combined region were also identical to single jet values [19]. For x/d > 20, self-similarity was observed in the

streamwise mean velocity profiles. This, for streamwise Reynolds normal stress was only observed in the vicinity of the shear layers.

In contrast to [4], Tanaka [1] observed that the decay rate in the converging region was higher compared to the single jet. For instance, the decay rate for S/d = 18 was observed to be 54% higher than its single jet counterpart. This was also the case in the combined region. For instance, for S/d = 18 the spread and decay rates were 78% and 270% higher than their single jet counterparts. The reason for this increment was attributed to higher downstream increment of static pressure respect to momentum diffusion.

Elbanna *et al.* [20] investigated the combined region of twin parallel plane jets with S/d = 12.5 at Re_d = 20,000 using hot-wire. In line with findings of Miller and Comings [4], in the combined region, it was observed that the decay and spread rates were almost similar to those reported in the single jet study of Gutmark [21].

Lin and Sheu [22] investigated the mean flow and turbulence statistics of twin parallel plane jets at Re_d = 9,000 and S/d = 30 and 40 using hot-wire with a split film probe in order to identify the flow direction in the converging region. Similar to the findings of Tanaka [1] it was observed that in the converging and combined regions, the decay rate of maximum streamwise mean velocity, is respectively 133% and 15% higher than the single jet of Gutmark [21]. Indeed, the spread rates of the inner and outer shear layers in the converging region as well as the spread rate of the outer shear layer in the combined region were respectively 16%, 80% and 53% higher than their counterparts in the single jet study of Gutmark [21]. The values suggest that in the converging region, the spread rate of the outer shear layer is 55% greater than the one for the inner shear layer. The authors attributed this difference to higher amount of fluid that can be entrained into the jet envelop via the outer shear layer, as the inner shear layer is confined by the jets.

The decay and spread rates in the study of Harima *et al.* [15] were also compared with their single jet counterparts. For all of the test cases, the decay rate in the combined region was observed to be identical to the one in single jet and equal to $K_u = 0.125$. As for jet half-velocity width in the transverse and lateral directions, it was observed that upstream of the combined point, their values are smaller than the single jet counterparts. For instance, for $S/d = 2$, at any location upstream of the combined point, the jet half-velocity width in the transverse direction was 10% lower than its single jet counterpart. Downstream of the CP location however, the lateral component of the jet half-velocity width initially adopts higher values and then equals its single jet counterpart. The transverse component on the other hand shows similar values as the ones on single jet.

2.4. Summary of the literature

In this chapter, the literature pertinent to twin jets was reviewed. The review shows that even though the main body of the literature is on 2D twin jets, there still exist differences between the reported quantities. For instance, some discrepancies between studies were observed for the decay and spread rates of 2D twin jets and how they differ from their single jet counterparts [1, 4, 22]. On the other hand, the review shows that fewer studies have focused on 3D twin jets. In particular, there are only three studies [15–17] that investigated the effect of nozzle spacing ratio on 3D twin jets all of which employed round nozzles. Regarding the coherent structures, some recent studies have thoroughly investigated this matter on 2D twin jets [10, 14, 23, 24], while a necessity for such studies on 3D twin jets is evident.

In conclusion, the review, provided in this chapter, revealed that on one hand there exists a lack of systematic study on the effect of nozzle spacing ratio on 3D twin jets and, on the other hand, such a study must thoroughly investigate the flow field in terms of the mean flow, turbulence quantities and coherent structures. The present PIV study is then able to address these issues by

providing mean flow and turbulence results in one-dimension to investigate the evolution of the corresponding quantities along streamwise and transverse directions. Contour plots of the mean flow, higher order turbulence statistics and coherent structures, on the other hand, make it feasible to investigate the flow physics in the whole measurement field.

Chapter 3

Experimental setup and test conditions

3.1. Overview

In this chapter detailed information regarding the experimental procedure are provided. In the first subsection, details of the test facility are provided. The test conditions, including the details of nozzles, test cases and initial conditions, are discussed in the second subsection. In the third subsection, different parts of the PIV setup are discussed. Further details regarding the measurement procedure and uncertainty estimates can be found in Appendices A and B.

3.2. Test facility

Fig. 3-1 shows the schematics of the test facility. The main body of the test facility was an air chamber with length, height and width of 1,100 mm, 734 mm and 534 mm, respectively. In order to provide optical access, the top wall and one of the side walls of the air chamber were made of transparent acrylic glass. The remaining walls were painted black to minimize laser light reflection. Filtered and compressed air with the maximum pressure of 660 kPa, was introduced to the test facility. The air temperature and pressure were monitored upon entering the test facility in order to provide identical initial flow condition for all the test cases. An aerosol generator used to introduce 1 μm olive oil particles to the air flow. Also, a bypass valve was installed in order to control the amount of particles injected into air. A settling chamber was installed upstream of the test section to decrease the turbulence level of the flow by directing the seeded air through several perforated stainless steel plates and polycarbonate honeycomb. This process breaks down the large-scale turbulence structures and improves the homogeneity of the flow. The exit of the test

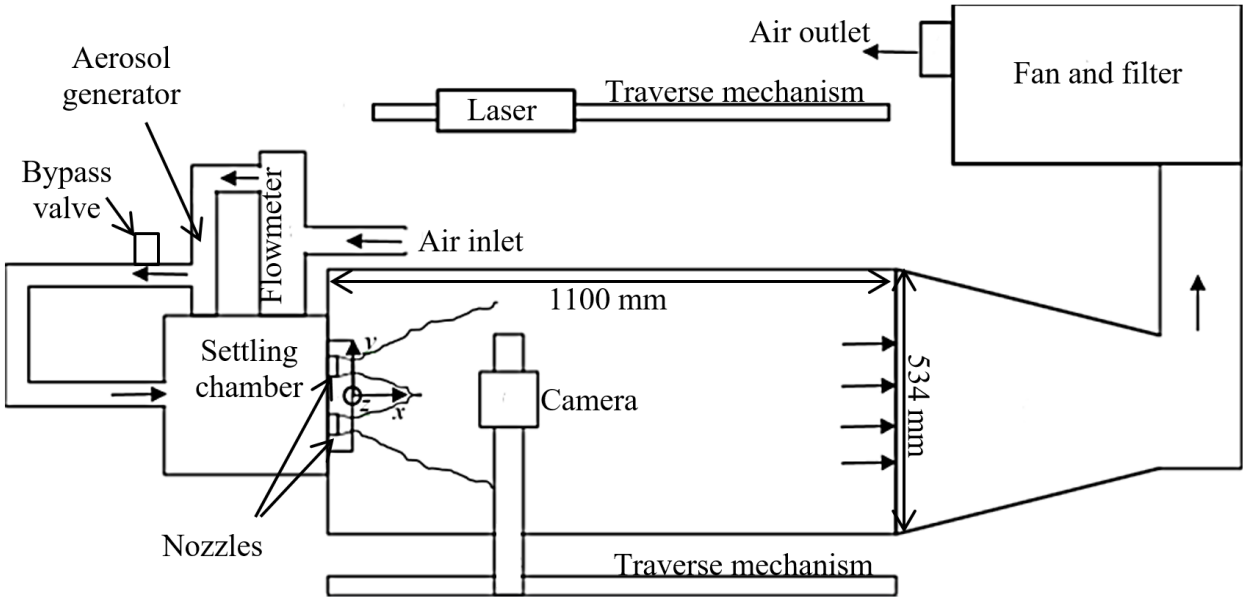

Fig. 3-1. Schematics of the test facility.

section was attached to a 600 mm long converging aluminum duct and a fan and filter assembly in order to direct and discharge the air flow into the room and remove its seeding particles.

3.3. Test conditions

As was discussed in chapter 1, the present study investigates the effect of nozzle spacing on twin jets issuing from low aspect-ratio rectangular nozzles. Therefore, the nozzles as well as the test cases were designed to satisfy this objective.

3.3.1. Nozzles

Two identical nozzles were installed at the end of the settling chamber to provide jets of air into the test section. Fig. 3-2 shows the detailed dimensions of the nozzles. The contraction length of the nozzles was 9 mm with a contraction ratio of 4. This led to a sharp contraction nozzle type, which is intermediate to an orifice nozzle (with sudden contraction) and a smooth contraction

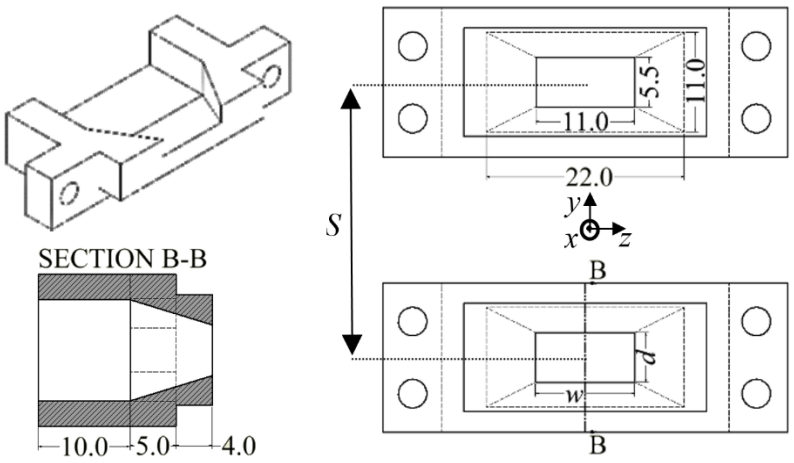

Fig. 3-2. Detailed dimensions of each nozzle in millimeters and the schematics of nozzles configuration.

nozzle. There were two reasons for selecting this type of nozzle. First, it provides higher mixing characteristics compared to smooth contraction nozzles [25], which is desirable in several engineering applications especially in HVAC systems. Second, similar nozzle type was used to perform experiments on free single jets. Therefore, using this particular nozzle type would facilitate a reliable comparison of the present results to previous results for single jet and twin free jets produced from different nozzle geometries. The dimensions of nozzles were $d \times w = 5.5 \times 11$ mm^2 which is equivalent to an aspect ratio of AR = 2.

3.3.2.Test cases

A total of 5 spacing between the nozzles were tested. As it is shown in Fig. 3-2, the center-to-center distance between the nozzles is denoted by *S*, and the following spacing between the nozzles were selected: *S* = 16.50 mm, 24.75 mm, 33.00 mm, 49.50 mm and 66.00 mm. To facilitate comparison of the present results with other studies with different nozzle geometries, an equivalent diameter, $d_e = 2\sqrt{\frac{d \times w}{\pi}}$ was adopted as a characteristic length scale. Thus, the nozzle spacing ratios were S/d_e = 1.8, 2.8, 3.7, 5.5 and 7.3. This covers a wide range of spacing such that the

highest spacing is about 4 times the lowest spacing. Also, the difference between successive spacing ratios is at least 33%. Therefore, significant effect of nozzle spacing on the results should be expected. Cartesian coordinate system was adopted with *x*, *y* and *z*, respectively representing the streamwise, transverse and lateral directions. As it is shown in Fig. 3-2, the origin of the coordinate system is located on the plane of the nozzles and in between of them. Therefore, $x = y = z = 0$ is where the symmetry line between the jets coincides with exit plane of the jets (see also Fig. 1-1).

3.3.3. Initial conditions

As mentioned earlier, one of the objectives of the present study is to compare the results with the ones on single jet [25, 26] performed in the same facility. Therefore, in order to remove the effect of initial conditions by employing identical nozzles, Reynolds number similarity was also considered. For all of the experiments, the jet exit velocity was kept constant and equal to U_e = 16.5 m/s, which corresponds to a Reynolds number based on equivalent diameter of Re_{de} = 10,000. It should be noted that matching the exit Reynolds number in the present study and previous single jet experiments leads to dissimilarity of the momentum fluxes in the present experiment and the single jet experiment. This dissimilarity in momentum flux between the two studies is not expected to affect comparison between the results because Aleyasin *et al.* [27] investigated the effects of Reynolds number and observed no significant differences between the flow characteristics for Re_{de} = 10,000 to 20,000. In other words, although the total momentum flux from the twin jets is twice the corresponding value for the single jet experiment at Re_{de} = 10,000, the single jet results for Re_{de} = 20,000 (which has similar momentum flux as in the present study) compared reasonably well with the results obtained at Re_{de} = 10,000.

Profiles of the one-dimensional streamwise mean velocity and streamwise turbulence intensity at x/d_e = 0.1 are shown in Fig. 3-3. In here, y_{cl} and U_{cl} are, respectively, the location of the jet centerline and its streamwise mean velocity at this location. As the profiles were extracted very close to nozzle exit (x/d_e = 0.1), they were identical for different spacing ratios, thus, for brevity, the profiles are only shown for S/d_e = 1.8. Also, the profiles are only shown for the lower jet as symmetry was observed between the lower and the upper jets. In Fig. 3-3a, the streamwise mean velocity profile is almost flat within the jet envelop. However, on the edges of the profile, where the shear layers are located, small peaks (overshoots) can be observed. The former is the characteristics of a top-hat velocity profile, generated by a smooth contraction nozzle, while the latter is for a saddle-back velocity profile, generated by an orifice nozzle. Hence, as it was the case for the nozzle type, the velocity profile is also intermediate to the top-hat and saddle-back profiles. However, as the overshoots are as low as 1%, it can be concluded that the jet-exit velocity resembles the top-hat profile more than the saddle-back.

Turbulence intensity at nozzle exit is an indication of the homogeneity of the releasing jet. Therefore it is required to keep its value as low as possible to make sure that no large scale structures are formed prior to nozzle exit. Fig. 3-3b shows the streamwise turbulence intensity at x/d_e = 0.1. Expectedly, within the jet envelope, where the streamwise mean velocity profile was almost flat, the turbulence intensity level is low and equal to $\frac{u_{rms}}{U_{cl}}$ = 3%. This region however, is enclosed by two peaks at the edges of the jet which, due to the strong mean shear between the jet and the ambient fluid, are as high as $\frac{u_{rms}}{U_{cl}}$ = 18%.

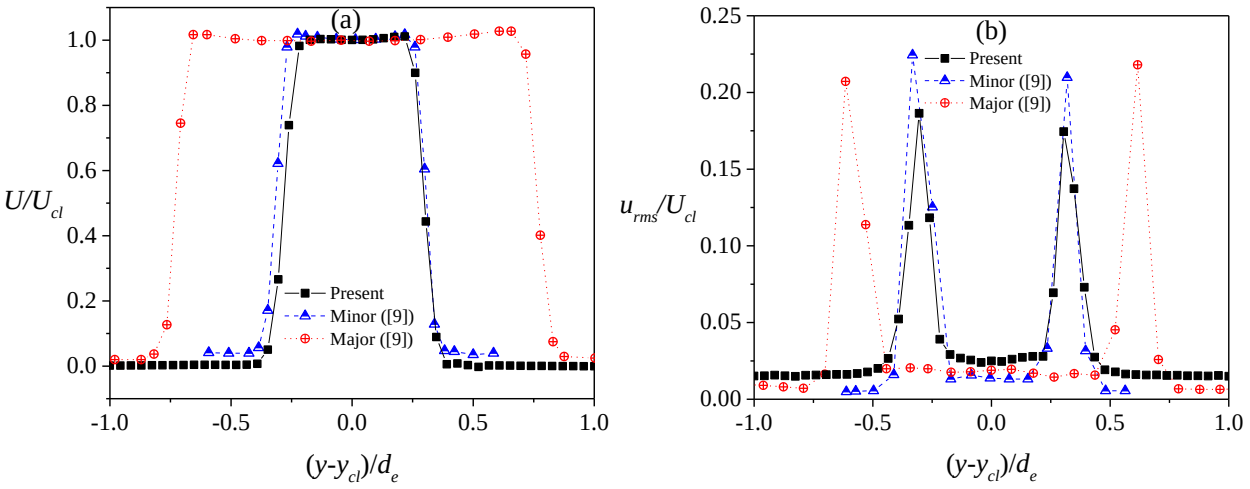

Fig. 3-3. One-dimensional profile of (a) streamwise mean velocity and (b) streamwise turbulence intensity at $x/d_e = 0.1$.

As one can notice in Fig. 3-3a and Fig. 3-3b, the single jet profiles of Aleyasin *et al.* [25] in the minor and the major planes are also provided. Except from 17% difference in turbulence intensity level in Fig. 3-3b, the profiles of the present study are identical to [25]. This shows that even for the lowest spacing ratio, where early interactions between the jets are expected; inlet conditions are identical to the ones in single jet. Comparison between the results of the present study and those on single jet (*e.g.* [25]) is provided on several of the results discussed in the upcoming section.

3.4. Particle image velocimetry

The velocity measurements were performed using a particle image velocimetry (PIV) technique. The technique is a non-intrusive, whole-field optical method in which the velocity vector of the flow at any measurement location is accessible. A PIV system has three main components. A laser which illuminates the flow, a camera which records the images of the illuminated flow, and a data acquisition system which acquires the data and post-processes the recorded images.

In a PIV technique, the flow field is seeded with small particles prior to the measurements. The particles, must meet two general conditions. First, they must be able to scatter light and second, they must be able to follow the trajectory of the flow with good accuracy. The seeded flow then enters the measurement section in which it is illuminated by the laser light. Two pulses of laser with time interval of Δt illuminate the flow and at the same time, the camera records two images of the flow field. A color filter (depending on the light emitted by the laser) is installed on the camera's lens in order to bypass the light scattered by the particles and remove any other background light. The recorded images are then divided into a matrix of grids which are called the interrogation areas (IA). For each of the IAs, a numerical correlation method (*e.g.* cross-correlation or auto-correlation) is used to evaluate the displacement of the particles, Δd, and hence determine the velocity vector of the IA by $V = \frac{\Delta d}{\Delta t}$. Therefore, the velocity vector map of the measurement field is obtained.

3.4.1. Seeding particles

As mentioned earlier, the particles used for PIV must meet two general conditions. First they must be small enough to follow the trajectory of the flow with adequate accuracy and second, they must be large enough to scatter enough light for the sake of image processing. For gaseous fluids, oil droplets such as silicon oil or organic oils are used [28]. However, due to the large density difference between the working fluid and the seeding particles, the size of the droplets must be in the order of microns to result in small settling velocity which is based on Stokes drag law for around a sphere under gravity [29]. In order to calculate the settling velocity, u_s, Eqn (3-1) was used. In this equation, ρ_p and ρ_f are respectively the density of the particles and working fluid, g

is the gravitational acceleration, d_p is the mean diameter of the particles and μ_f is the viscosity of the working fluid.

$$u_s = \frac{(\rho_p - \rho_f) g d_p^2}{18\mu_f} \quad \text{Eqn (3-1)}$$

In the present study, ρ_p = 913 kg/m^3, ρ_f = 1.2 kg/m^3, d_p = 1 μm and μ_f = 1.85×10^{-5} kg/ms. The resultant settling velocity was then evaluated to be u_s = 2.7 × 10^{-5} m/s, which is 6 order of magnitudes smaller than jet exit velocity of U_e = 16.5 m/s. The tendency of the particles to attain velocity equilibrium with the flow is characterized by the response time, τ_r, [30]. Similar to the settling velocity, the response time of the particles must be low. In order to calculate the response time, Eqn (3-2) was used.

$$\tau_r = \frac{\rho_p d_p^2}{18\mu_f} \quad \text{Eqn (3-2)}$$

In the present study, the response time was calculated to be τ_r = 2.7 × 10^{-6} s. In order to examine whether τ_r is small enough for the particles to follow the flow faithfully, Stokes number, which is the ratio between particles' response time, τ_r, and fluid characteristics time scale, τ_f, is used. The latter is defined as the ratio between representative velocity and length scales of the flow, shown respectively as u_0 and l_0 in Eqn (3-3).

$$\tau_f = \frac{l_0}{u_0} \quad \text{Eqn (3-3)}$$

Following [30], the characteristic velocity and length scales of the flow in the present study are the exit velocity, U_e = 16.5 m/s, and equivalent diameter, d_e = 9 mm. The resultant Stokes number is Stk$_{de}$ = 5× 10^{-3}. As Stokes number is much smaller than unity, it can be concluded that the particles follow the trajectory of flow streamlines reasonably well.

3.4.2. Measurement procedure

In PIV, the particle displacement is required to be equal or less than one quarter of the interrogation area in order to ensure a good signal-to-noise ratio, reduced peak-locking effect and consequently increased dynamic velocity range. The laser pulse separation time, Δt, was then calculated by Eqn (3-4). In here, N is the interrogation window size and $M_f = \frac{1}{S_f}$ is the magnification factor.

$$\Delta t = \frac{N \times d_{pitch}}{4 M_f U_e} \qquad \text{Eqn (3-4)}$$

Using the values provided above, time between pulses was set to Δt = 23.5 μs. The convergence test results regarding of the streamwise mean velocity, streamwise and transverse turbulence intensities and Reynolds shear stress (presented in Appendix A) showed that 7,500 images are sufficient to have the results independent of the sample size. In order to obtain statistically independent snapshots, the sampling frequency was set to f_s = 2.5 Hz.

The measurements were performed for $0 < x/d_e < 42$. This range contains four measurement planes as the field of view was set to FOV = 100 × 100 mm^2. Based on the calibrations and the assigned FOV, the scale factor of the camera was S_f = 6.612. A 5 mm overlap in the streamwise direction was allowed between successive FOVs in order to remove the loss of velocity data on the boundaries of the measurement planes.

A spatial resolution test showed that at x/d_e = 5.0, there exists a difference between the results for IA = 32 × 32 and 32 × 16. Irrespective of the spatial resolution applied, consecutive IAs had 50% overlap in the x and y directions. The vector spacing was then $0.087d_e \times 0.043d_e$ and $0.087d_e \times 0.087d_e$ for IA = 32 × 16 and IA = 32 × 32 respectively. At x/d_e = 5 along the jet centerline, where

IA = 32 × 16, the size of Taylor microscale in the *x* and *y* directions was, respectively, 2.18 and 4.36 times the vector spacing. For Kolmogorov length scale, this however was reduced to 0.07 and 0.14 times the vector spacing in the *x* and *y* directions respectively. At $x/d_e = 25$, the size of Taylor microscale and Kolmogorov length scale were 3.67 and 0.14 times the vector spacing. Thus, as was expected, the adopted spatial resolutions were only able to capture Taylor microscale and not the Kolmogorov length scale.

Details regarding the sources of error and uncertainty calculations are provided in Appendix B.

Chapter 4

Effect of nozzle spacing on turbulent interaction of low-aspect-ratio twin rectangular jets

4.1. Introduction

In many engineering applications such as heating, ventilation and air conditioning (HVAC) systems, fuel injectors, mixing chambers and pollution dispersion stacks, multiple nozzles are often installed to either increase the mass flow rate or enhance the mixing of the fluid. The jets issued from these nozzles interact with each other as they develop downstream of the exit plane. This mutual interaction typically results in a significantly more complex shear flow pattern compared to a free single jet. In spite of their practical importance, the available literature on twin-jet interaction is limited and, as a consequence, our knowledge on this subject is deficient compared with that on the canonical single free jet. The early studies on twin jets date back to experimental studies by Miller and Comings [4] and Tanaka [1, 6]. These studies used hot-wire anemometry (HWA) to investigate two-dimensional (2D) twin parallel plane jets. The former, [1], adopted single nozzle spacing ratio of S/d = 6 (see Fig. 1-1) to investigate the mean flow, streamwise Reynolds normal stress and pressure distribution at different downstream locations, while Tanka [1, 6] used several large spacing ratios to investigate the effect of nozzle spacing on the mean flow and turbulence intensities. Although these studies successfully revealed some salient features of twin-jet interactions, they were limited to 2D case of twin jets, which will be shown to have major differences with its three-dimensional (3D) counterpart. Also due to the limitations of the measurement technique, they did not thoroughly investigate the flow quantities in the whole flow-field.

Fig. 1-1 shows the schematic of two parallel jets. The center-to-center spacing between the nozzles and the width of each nozzle are denoted by S and d, respectively. The streamwise, transverse and lateral directions are denoted by x, y and z, respectively. The existence of the inner and outer shear layers is the result of the velocity gradient between the high-momentum jets and the ambient fluid. The inner shear layers converge toward each other as a result of jet spreading. As a consequence, the inner shear layers meet at the so-called "merging point" (MP) located on the symmetry line and the region from the nozzle exit to the MP is referred to as the "converging region". In this region, the spread of the inner and outer shear layers at a given streamwise location is measured using the half-velocity width, defined as the distance from the symmetry line to the position where the mean velocity is one half the local maximum. As shown in Fig. 1-1, corresponding to the inner and outer shear layers, the half-velocity width is denoted as $y_{0.5}^{-}$ and $y_{0.5}^{+}$, respectively.

Downstream of the MP, the inner counter-rotating vortical structures start to interact with each other. Meanwhile, the trajectory of the local maximum velocity for each jet bends towards the symmetry line in order to compensate for the momentum deficit of the flow between the jets. As the distance from the MP increases, the transverse profile of the mean streamwise velocity transitions from a dual-peak to a single-peak pattern. The exact streamwise location where the single-peak pattern appears in the mean velocity profile of the merged dual jets is referred to as the "combined point" (CP) and the region between the MP and the CP is called the "merging region". Downstream of the CP, the characteristics of the single-peaked mean streamwise velocity profile become increasingly similar to those of the self-similar single jet. One can expect that higher-order (second order and above) turbulence statistics will continue developing and eventually show a full resemblance to a self-similar single jet in the far downstream region [4].

The mixing and turbulent characteristics of twin jets are strongly dependent on the nozzle spacing ratio (*S/d*) and other key parameters such as Reynolds number and nozzle geometry. Tanaka [1, 6] investigated the effects of nozzle spacing ratio of $8.5 \leq S/d \leq 25$ and Reynolds number of ($4{,}290 \leq \mathrm{Re}_d \leq 8{,}750$) on the flow characteristics of twin parallel plane jets. The results showed that the location of the maximum pressure and the magnitude of the maximum mean streamwise velocity along the symmetry line were independent of Reynolds number. The decay rate of the maximum velocity, evaluated for a streamwise extent of $0 < x/d < 15$, was higher for the twin jets than for its single jet counterpart, and the disparity between the observed decay rate for the twin jets and single jet increases with an increase in nozzle spacing. For example, the decay rate increased from 0.147 for $S/d = 8.5$ to 0.173 for $S/d = 16$. However, for $S/d > 16$, the decay rate was no longer dependent on the nozzle spacing ratio. It was also observed that the transverse development of the local maximum velocity is located on the arc of a circle, and the radius of this arc is constant and independent of the nozzle spacing ratio for $S/d < 16$. It was argued that for $S/d < 16$, the converging region is so short that the jets are still in their developing stage and therefore, high velocity with large gradients are expected. In this fashion, the negative pressure region within the jets is solely dependent on the dynamic pressure of the discharged jets. As a result, the curvature of the jets is not a function of the spacing between the nozzles, but the jet exit conditions.

In the numerical study conducted by Spall *et al.* [8], the effect of nozzle spacing ratio (S/d = 3, 5, 7, 9 and 11) on the total momentum flux of twin parallel plane jets was examined. Although Tanaka [1] indicated that the total momentum flux, which comprises the integral of the mean momentum, pressure and turbulence fluctuations is constant, it was shown that the constant decreases as the spacing increases [8]. For instance, it was observed in Spall *et al.* [8] that the integral constant for the largest spacing ratio was 15% lower than the smallest spacing ratio. This

is not surprising, because the interaction of twin jets is a dynamic and nonlinear process, which is accompanied with enhanced turbulent mixing of fluid momentums and increased viscous dissipation. As nozzle spacing decreases, more intense interactions are expected, hence larger total momentum integral constant.

Hassan and Lee [14] in a PIV study, investigated the flow field of twin parallel plane jets in the vicinity of the merging point for $S/d = 3.07$ and at $Re_d = 4{,}900$. Based on the results of previous studies on twin parallel plane jets in which $S/d < 10$, two trends for the location of the merging point with respect to nozzle spacing was proposed. For $S/d < 4$, a non-linear trend between the merging point and nozzle spacing was suggested in which the length of the converging region was lower than nozzle spacing. For $S/d > 4$, a linear trend was proposed in which the merging point location was 1.15 times of the nozzle spacing. In the potential core region, the jets do not diverge linearly but they maintain a straight pattern. It was then argued that when the jets are spaced closely, the relationship between the merging point location and nozzle spacing is not linear.

Okamoto *et al.* [5] investigated the effect of nozzle spacing on mixing characteristics of twin round jets and compared the performances of the twin round jets with that of a single round jet. The experiments were performed for $S/d = 5$ and 8.06 at a fixed Reynolds number of 100,000. The decay of the local maximum velocity was independent of the nozzle spacing ratio. The transverse spreads of the inner and outer shear layers were evaluated with respect to the jet centerline and to the point where the mean streamwise velocity is 10% of its local maximum. In the converging region, the spread of the inner shear layer for $S/d = 5.00$ and 8.06 of the twin jets was reported to be lower than and similar to that of a single jet, respectively. The spread rate of the outer shear layer on the other hand was independent of the nozzle spacing ratio but 14% lower than that of a single jet up to $x/d = 20$. Downstream of this location, the spread rate showed a similar trend as

that of a single jet. The measured static pressure for both spacing ratios was slightly higher (about 13%) compared to that of a single jet for $x/d \geq 40$. Based on these observations, it was concluded that twin jets show a faster recovery to the ambient pressure than does the single jet.

Harima *et al.* [15] performed hot-wire measurements of twin round jets for S/d = 2, 4 and 8 at Re_d = 25,000. They observed that in the combined region, the values of jet half-velocity width in lateral direction were larger in the region immediately after the CP then eventually became comparable to that of a single jet. The values of jet half-velocity width in the transverse direction on the other hand were comparable to that of a single jet downstream of the CP. The authors attributed this switching tendency of the jet half-velocity width in the lateral and transverse directions to a phenomenon similar to the axis-switching of asymmetric jets, although on a smaller scale.

In their follow-up study, Harima *et al.* [16] focused on the effect of nozzle spacing on turbulent statistics of twin round jets. They observed that the streamwise location of the maximum streamwise turbulence intensity, moves downstream as the spacing increases. This was attributed to the suppression effect of jets interactions on the development of streamwise turbulence intensity along the jet centerline. For the largest nozzle spacing (S/d = 8) the location of the maximum decreased by 17% compared to S/d = 2. The location, however, was comparable to the one in single jet. The authors argued that for S/d = 8, jet interactions have no pronounced effect upstream of the location of maximum turbulence intensity.

In a more recent study, Zang and New [17] performed 2D time-resolved particle image velocimetry (TR-PIV) measurements to provide insight into the flow structure in twin round jets. The experiments were performed at a fixed Reynolds number of Re_d = 3,300 and three nozzle spacing ratios of S/d = 1.5, 2 and 3. The results revealed the existence of counter-rotating

structures, similar to the flow behind a bluff body, within the inner shear layers of S/d = 1.5 and 2. They observed two different trends for the frequency peak of the outer and inner shear layers. As the jet envelope in the outer shear layer develops freely, the peak frequency was observed to be f = 5.8 Hz, which is similar to that of a single jet. However, relatively lower frequencies of f = 4.4, 4.8 and 5.0 Hz for the inner shear layer were reported for S/d = 1.5, 2 and 3, respectively. This trend shows that as the nozzle spacing increases, the vortical structures in the inner shear layers are less confined by the suppression region within the jets and as a result, their frequency approaches typical values in a single jet. Therefore, as the spacing increases, the peak frequency of the inner shear layer increases as well and approaches the one on the outer shear layer.

It is clear from the above review that there exist major differences in the development of 2D and 3D twin jets, especially in their mixing characteristics. On the other hand, the limited studies on 3D twin jets were only focused on axisymmetric jets. In the present study, however, low-aspect-ratio rectangular nozzles were employed in order to investigate the effect of nozzle spacing on twin asymmetric jets, which to the authors' knowledge, is the first of its kind. To achieve this, a PIV experiment was performed on twin low aspect-ratio rectangular nozzles for 5 spacing ratios. The type of the nozzles was identical to those used in the same test facility for the study of single rectangular jet [25], in order to have a legitimate comparison of twin jet results with the ones on single jet. The remainder of the paper is organized as follows. In section 4.2, the effects of nozzle spacing on the mean flow characteristics, turbulence intensities and Reynolds shear stresses are investigated. In section 4.3, the research findings and conclusions of this study are summarized.

4.2. Results and discussion

In order to qualitatively discuss some of the salient features of twin jets of the present study, the mean velocity vectors field superimposed with the contours of the mean streamwise velocity

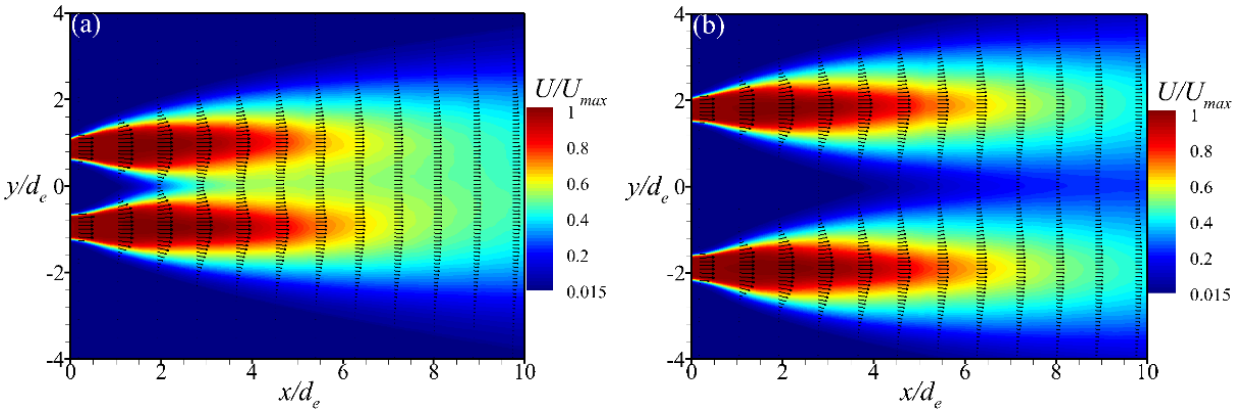

Fig. 4-1. Velocity vectors field embedded into the contour plots of mean streamwise velocity for (a) S/d_e = 1.8 and (b) S/d_e = 3.7.

are shown in Fig. 4-1. For brevity, the plots are only shown for S/d_e = 1.8 and 3.7 in Figs.4-1a and 4-1b, respectively. Apparently, with respect to the mean velocity field, the twin jets show identical behavior and symmetry about y/d_e = 0. As sharp contraction nozzles were used for this study, one can notice the well-known vena contracta effect. As a result, U_{max} is not located at jet exit, but further downstream at x/d_e = 0.8. The length of the potential core region, where the gradient of mean streamwise velocity in the streamwise direction is almost zero, was then evaluated from nozzle exit up to the point where jet centerline velocity, U_{cl}, reduces to 98% of U_{max}. Based on this criterion, the potential core length was evaluated to be x_{pc}/d_e = 3.0, 3.1, 2.9, 3.0 and 2.9 for S/d_e = 1.8, 2.7, 3.7, 5.5 and 7.3, respectively. The difference is negligible which implies that changing the spacing between the nozzles does not affect the length of the potential core. These values are also comparable to x_{pc}/d_e = 3.4 and x_{pc}/d_e = 3.1 reported by [25] and [31], respectively for a free single jet issued from sharp contraction and orifice plate rectangular nozzles with AR = 2.

The studies on 2D twin parallel plane jets showed that due to the spanwise homogeneity, there is no entrainment in the lateral direction, and this results in the existence of recirculation region within the jets in the converging region. In the present study, the ratio between the width of the

chamber to length of the nozzle (w) was 67 times. Also, the length of the side walls (height of the chamber) was 25 and 7.5 times the smallest and the largest spacing ratios (S/d_e = 1.8 and 7.3 respectively). The jets are then not bounded to the side walls (as it was the case in 2D parallel plane jets), and hence, there exists lateral entrainment. As a result, there is no negative velocity vectors field region within the jets in Figs.4-1a and 4-1b. This introduces a challenge in locating the MP, as in previous studies on 2D parallel plane jets, the MP was determined as a point on the symmetry line where the mean streamwise velocity changes its sign from negative to positive. Based on the definition, the MP is the streamwise location at which the mean streamwise velocity along the symmetry line obtains a positive non-zero value. In PIV, this is constrained by the minimum resolvable particle displacement or the PIV dynamic velocity range. For the present PIV setup, with IA = 32 × 32 pixels, the maximum particle displacement was 8 pixels and the sub-pixel accuracy of the camera was 0.1, leading to the dynamic velocity range of 80. Thus, in order to confidently locate the MP, the streamwise location on the symmetry line where $\frac{U}{U_{max}}$ = 0.015 was selected in the present study, which is shown by the lowest contour level in Figs.4-1a and 4-1b. Hence the streamwise location where these contour levels meet on the symmetry line was considered as the MP location.

Based on the above-mentioned criterion, the location of the MP was determined to be at x_{mp}/d_e = 1.1, 2.3, 3.7, 7.5 and 10.8 for S/d_e = 1.8, 2.8, 3.7, 5.5 and 7.3, respectively. The location of the CP on the other hand was evaluated to be at x_{cp}/d_e = 10.0, 17.1, 24.8 and 40.7 for S/d_e = 1.8, 2.8, 3.7 and 5.5, respectively. It should be mentioned that for S/d_e = 7.3 the jets did not combine in the range of the PIV measurements and therefore, no combined point location was reported for this test case. Figs.4-2a and 4-2b, respectively, show the locations of the MP and the CP with respect to nozzle spacing ratio. Evidently, both the merging and combined points move downstream as the

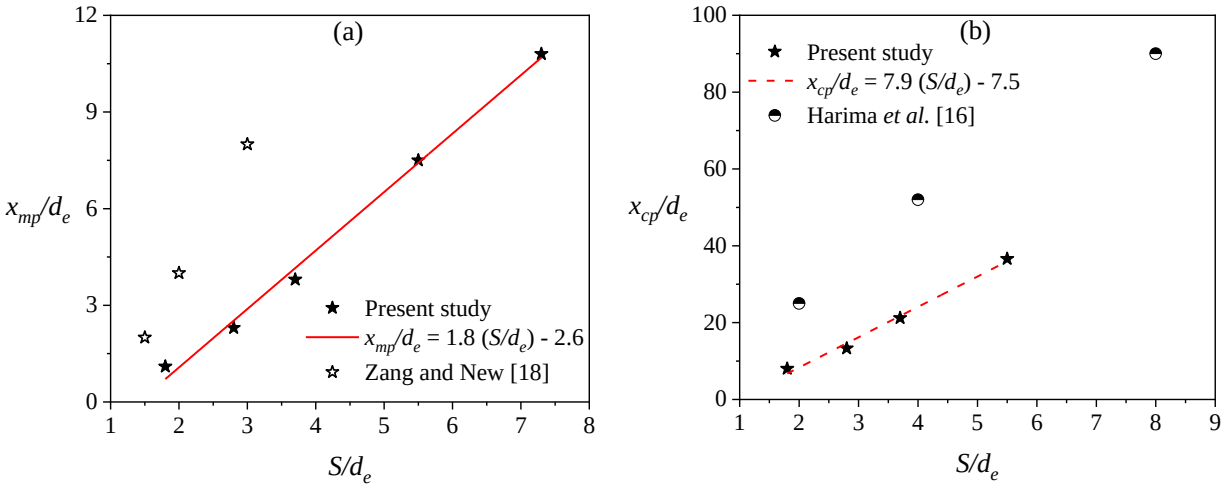

Fig. 4-2**.** (a) Merging point and (b) combined point locations respect to nozzle spacing.

spacing between the nozzles increases. The trends in Figs.4-2a and 4-2b show that the MP and the CP locations are linear functions of nozzle spacing ratio. However, as the slopes of the lines suggest, the latter is more affected by the change in nozzle spacing than the former. As discussed earlier, the MP is located on the symmetry line where the inner shear layers meet. Therefore, it is not only a function of nozzle spacing but also the spread rates of the jets' inner shear layers in transverse direction. On the other hand, the combined point is defined as a streamwise location at which the trajectory of the jet centerline velocity coincides with the symmetry line (see Fig. 1-1). The trajectory has been shown to be on the arc of a circle whose radius is a function of nozzle spacing [1, 15]. Therefore, compared to the merging point, the combined point location is more affected by the change in nozzle spacing. In Fig. 4-2a, the twin round jet results of Zang and New [17] are also provided for comparison. As it is clear from the trends in this figure, for a similar nozzle spacing ratio, the merging point is located further downstream in the case of twin round jets compared to twin rectangular jets of the present study. In other words, for a specific nozzle spacing ratio, the inner shear layers in the present study merge faster compared to the study of Zang and New [17]. Previous studies on free single jet showed that the jets issued from rectangular

nozzles show higher mixing characteristics (*e.g.* higher spread of the shear layers) compared to their round counterparts [25, 31]. Thus, as low-AR rectangular nozzles were used in the present study, the inner shear layers show faster convergence towards the symmetry line compared to the study of Zang and New [17]. Lee and Hassan [14] argued that for $S/d < 3$, the length of the converging region is shorter than nozzle spacing. It was argued that as the jets are close to each other, the inner shear layers are not developing freely but their respective counter-rotating vortical structures behave in a way similar to the wake flow behind a bluff body. Although in the present study, the normalization was done with respect to the equivalent diameter, d_e, one can still see in Fig. 4-2a that for $S/d_e < 3$, the length of the converging region is shorter than nozzle spacing. In Fig. 4-2b, the CP locations reported by Harima *et al.* [15] are presented for comparison. Similar to the MP location (Fig. 4-2a) the CP is located further downstream in the case of twin round jets, compared to the present study. This was expected, as delayed merging of the jets' inner shear layers also delays the location of the CP. Therefore, from Figs. 4-2a and 4-2b it can be concluded that for a specific nozzle spacing ratio, in comparison to twin round jets, the jets issued from low-AR rectangular nozzles not only merge sooner, but also show faster mixing in the merging region which advances the appearance of the combined jet.

Figs. 4-3a and 4-3b show the contour plots of mean transverse velocity, V, normalized by U_{max} for $S/d_e = 1.8$ and 3.7 respectively. The MP location is shown by a dashed line in these figures. From the nozzle exit up to $x/d_e = 0.8$, which was reported as the axis-switching point in the single jet study of Aleyasin *et al.* [25], the value of V/U_{max} on jets' shear layers increases. High levels of mean transverse velocity are located on jets' shear layers. Therefore, while an advanced merging for $S/d_e = 1.8$ results in immediate spatial suppression of V/U_{max} contours of the inner shear layers,

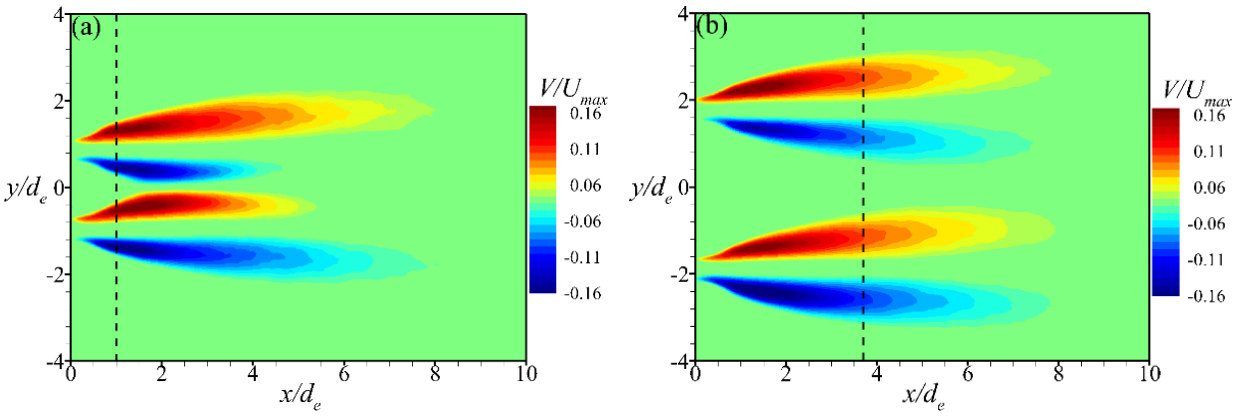

Fig. 4-3**.** Normalized mean transverse velocity for (a) S/d_e = 1.8 and (b) S/d_e = 3.7.

a retarded merging for S/d_e = 3.7 results in higher level of symmetry in the spatial development of the V/U_{max} contours between the inner and the outer shear layers.

Fig. 4-4a shows the downstream development of the normalized jet half-velocity width for the outer shear layer, $y_{0.5}^{+*}$. The jet half-velocity width profile of Aleyasin *et al.* [26] (shown as S-J [26]), which was obtained for a single jet with identical nozzle to the present study, is also provided for comparison. For a legitimate comparison, the $y_{0.5}^{+}$ values for the present study were subtracted from half of the spacing, ($y_{0.5}^{+*} = \frac{y_{0.5}^{+} - S/2}{d_e}$). Close to nozzle exit and up to x/d_e = 10.0, one can notice that the profiles of $y_{0.5}^{+}$ for twin jets of the present study collapse on the single jet profile of [26]. It is also noticeable that similar to profile of [26], upon exiting from the nozzles, the jets show high spread rates which is followed by a decrease and an increase again. This trend, which was also observed in previous single jet studies of [31–33], is due to the well-known axis-switching phenomenon, which is the characteristics of the jets issued from asymmetric nozzles. Downstream of x/d_e = 10.0 and in the converging and merging regions, there is a linear relationship between $y_{0.5}^{+}$ location and the streamwise distance which is of the form $y_{0.5}^{+*} = K_s(\frac{x}{d_e} + C_s)$. In here, K_s is the spreading rate and C_s is the geometric virtual origin of the jet. Based on the profiles of S/d_e =

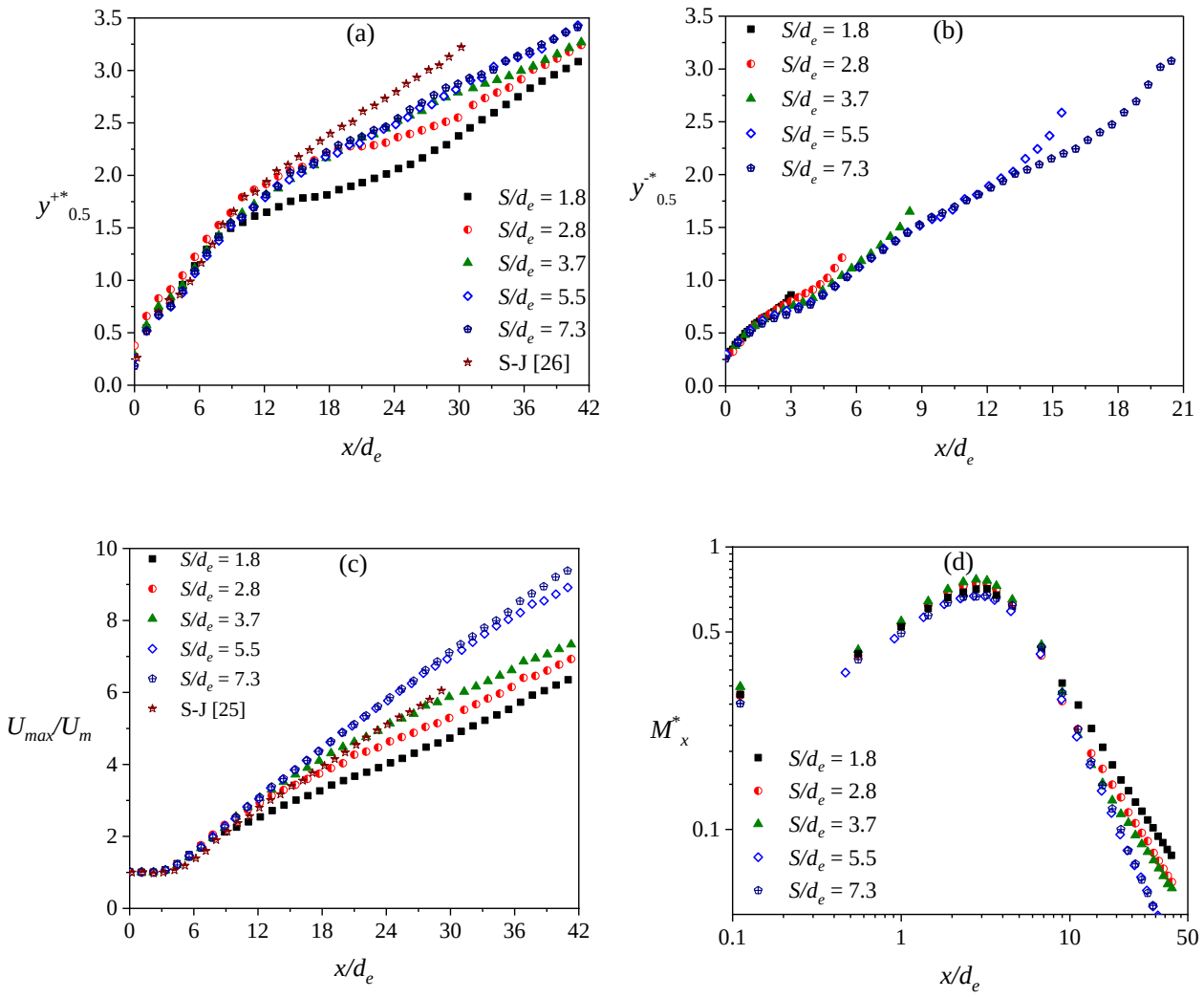

Fig. 4-4**.** Streamwise development of (a) jet half-velocity width in the outer shear layer, (b) jet half-velocity width in the inner shear layer, (c) Decay rate of the local maximum mean streamwise velocity and (d) momentum flux in the streamwise direction.

5.5 and 7.3, which have the longest monotonic region in the converging and the merging regions, the spread rate was evaluated to be $K_s = 0.06$ with $C_s = 1.16$ and 1.29 respectively. Although not quantified, one can still see that the slope of the profile of Aleyasin *et al.* [26] in the monotonic region is qualitatively similar to the one in the present study. As decreasing nozzle spacing decreases the distance of the CP location from jet exit, one can observe how the spread rate is affected in the combined region by following the profiles of $S/d_e = 1.8$ and 2.8. Upon approaching

the CP location, the profiles start to deviate from their trends and as a result the spread rate decreases. This is followed by an inflection point, downstream of which the spread rate increases once more. Take $S/d_e = 2.8$ (red circles) for instance; at $x/d_e = 13.3$, which is in the vicinity of $x_{cp}/d_e = 17.1$, the spread rate tends to deviate. Further downstream, roughly at $x/d_e = 21.0$, an inflection can be identified in the profile. This is finally followed by a linear region downstream of $x/d_e = 26.0$. Based on the profiles of $S/d_e = 1.8$ and 2.8, the spread rate in this region was evaluated to be $K_s = 0.07$ and $C_s = 0.25$ and 0.62 respectively. The spread rate in this region is comparable to its counterpart in the converging and the merging regions evaluated for $S/d_e = 5.5$ and 7.3. Compared with the trend observed due to axis-switching in the initial region ($0 < x/d_e < 8$), the spread rate of the outer shear layer qualitatively show similar trend downstream of the combined point. Thus, it can be speculated that upon entering the combined region, the jets go through a phenomenon which is qualitatively similar to the axis-switching of the vortex rings. A similar argument was also made by Harima *et al.* [15].

Fig. 4-4b shows the spread of the inner shear layer, $y_{0.5}^{-*}$. A similar normalization as in Fig. 4-4a was also applied in this figure. The profiles follow similar trends upstream of the merging point. Also, in this region, the spread of the inner shear layer is identical to outer shear layer which suggests that due to the entrainment of the ambient fluid from the spanwise direction, the jets spread symmetrically in the inner and outer shear layers. Downstream of the merging point however, a higher spreading of the jets inner shear layers is observed. This is an indication of intense interactions between the jets in the merging region.

Fig. 4-4c shows the decay of the local maximum velocity, U_m, with respect to the streamwise distance from the nozzles' exits. The results of Aleyasin *et al.* [25] (shown as S-J [25]) are also provided for comparison. Three distinct regions can be identified in this figure. In the potential

core region ($0 < \frac{x}{d_e} < 3$), as the center of the jet is intact of the momentum transfer with the shear layers, no decay can be observed and the plots in Fig. 4-4c show a constant value of $\frac{U_{max}}{U_m} \cong 1$. Further downstream, a linear decay region of the form $\frac{U_{max}}{U_m} = K_u\left(\frac{x-x_0}{d_e}\right)$ can be observed. In here, K_u is the decay rate and $\frac{x_0}{d_e}$ is the kinematic virtual origin of the jet. As one can notice, the decay rate upstream and downstream of the CP location is different. A linear fit on the profiles of S/d_e = 5.5 and 7.3, which have the latest CPs, shows that the decay rate for $3 < \frac{x}{d_e} < \frac{x_{cp}}{d_e}$ is identical and equal to K_u = 0.22, which is almost 15% higher than K_u = 0.192 reported by [25]. The kinematic virtual origin on the other hand changes with nozzle spacing ratio and is equal to $\frac{x_0}{d_e}$ = 0.42 and 0.33 for S/d_e = 5.5 and 7.3 respectively.

Downstream of the CP location, as the profiles of S/d_e = 1.8, 2.8 and 3.7 suggest, the decay rate decreases to K_u = 0.13, with kinematic virtual origin of $\frac{x_0}{d_e}$ = 0.95, 1.37 and 1.96 respectively. The explanation for the change in the trend of decay rate upstream and downstream of the CP is as follows. As mentioned earlier the trajectory of jet centerline from nozzle exit to the combined point forms an arc of a circle the radius of which is a function of nozzle spacing [1, 15]. The angle of the velocity vector of the jet centerline with respect to the *x* axis increases as the distance from nozzle exit increases. Therefore, it is expected that the projection of the velocity vector on the *x* axis, which is U_m, diminishes as the jets develops downstream. In other words, as the mean flow must compensate the momentum deficit within the jets, momentum of the jet centerline is not only in the *x* direction, but also in the transverse direction as well. Hence, it can be said that in the converging and the merging regions, there are two reasons for the decay of the local maximum velocity. First and similar to single jet, the spreading of the jet and entrainment of the ambient fluid

into flow field decays the local maximum velocity. Second, the velocity vector of the jet centerline is not parallel to the streamwise direction. Therefore, it is its projection along the streamwise direction that gives U_m. The absence of the second reason in a single jet results in its lower decay rate in a self-similarity region compared to the converging and merging regions of twin jets. This difference is more pronounced for S/d_e = 5.5 and 7.3 as they have longer converging and merging regions compared to the other test cases. In the combined region, as the jets' centerlines are merged and there is no momentum deficit within the jets to compensate anymore, the decay rate decreases compared to the converging and merging regions.

Downstream decay of the momentum of the jet centerline in the streamwise direction, $M^*_x = \frac{U_m^2 y_{0.5}^+}{U_{max}^2 d_e}$, is shown in Fig. 4-4d. Due to vena contracta effect (see Fig. 4-1), flow accelerates close to nozzle exit and hence M_x increases. Further downstream, M_x starts to decrease as the mean flow decays. A deviation from its upstream trend however, can be observed at similar streamwise locations in which the decay rate of mean flow changed its trend. In total, once the jets are combined, their mixing performance, with respect to spread and the decay rates decreases and so the momentum decay in the streamwise direction. Therefore, within a fix distance from the nozzles' exit, smaller spacing ratios result in faster merging and mixing of the jets, while larger spacing ratios result in higher mixing of individual jet envelops with the ambient fluid.

Along the symmetry line, as it is shown in Fig. 4-5a, the mean streamwise velocity increases downstream of the MP location. As the normalization was performed using $U_{max,}$ the peak value decreases as the spacing ratio between the nozzles increases. The profiles peak at x_{mU}/d_e = 4.4, 7.6, 11.3, 19.6 and 30.8 for S/d_e = 1.8, 2.7, 3.7, 5.5 and 7.3 respectively. Although x_{mU}/d_e locations move away from the MP location as nozzle spacing ratio increases, they are almost located within

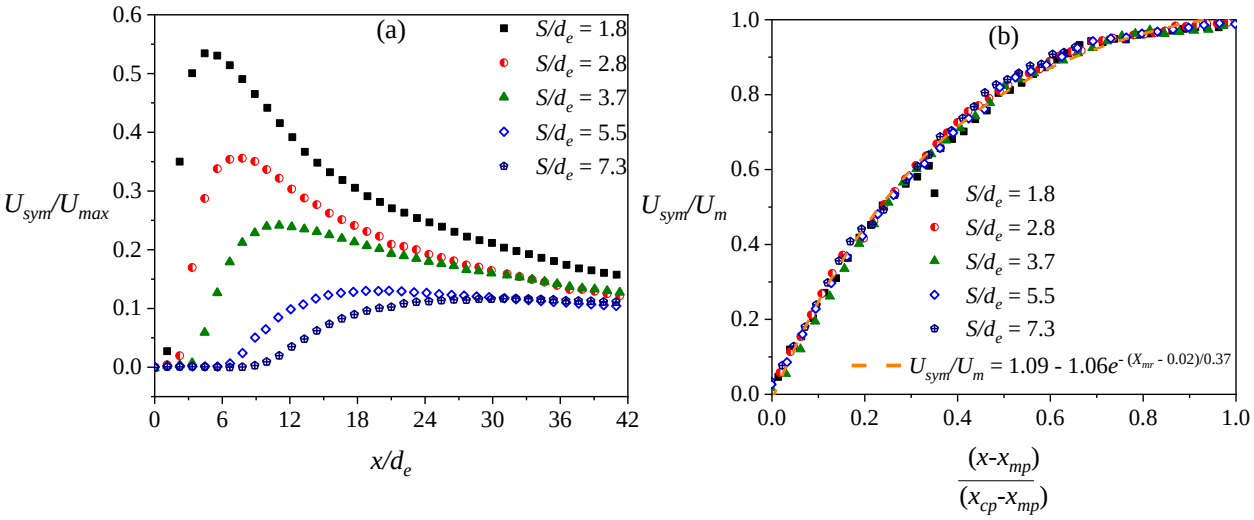

Fig. 4-5**.** (a) Downstream evolution of the mean streamwise velocity along the symmetry line, normalized by maximum mean streamwise velocity. (b) Increment in mean streamwise velocity along the symmetry line within the merging region.

36% of the merging region length for all of the test cases ($\frac{x_{mU-x_{mp}}}{x_{cp-x_{mp}}} \approx 0.36$). This independency suggests that normalizing with respect to the length of the merging region can remove the effect of nozzle spacing ratio on the development of the mean streamwise velocity along the symmetry line. To examine this, a new normalization technique was adopted in which the velocity scale was normalized by U_m and the streamwise distances were first subtracted from the MP location and then divided by the length of the merging region. The results are shown in Fig. 4-5b. As it was expected, the profiles collapse on top of each other. This interestingly shows that despite the effect of nozzle spacing ratio on the MP and the CP locations, and hence the length of the merging region, the increment of the mean streamwise velocity along the symmetry line with respect to jet centerline velocity, $\frac{U_{sym}}{U_m}$, is universal within the merging region. In other words, at any specific portion of the merging region, (from 0% at the MP to 100% at the CP), $\frac{U_{sym}}{U_m}$ results in a similar value for any spacing ratio between the nozzles. In order to quantitatively discuss this universality,

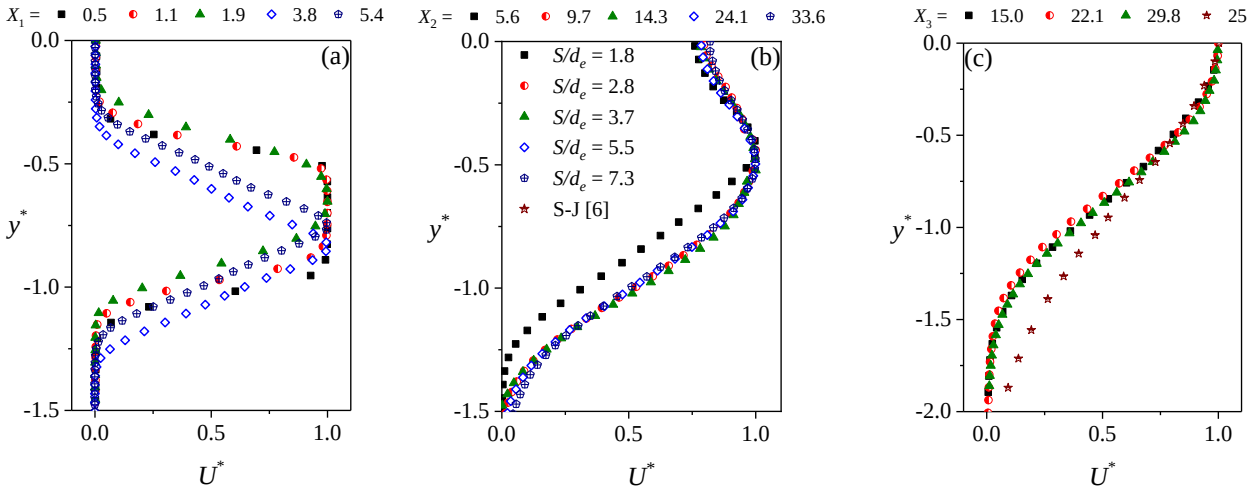

Fig. 4-6. Transverse profiles of the mean streamwise velocity at (a) the middle of the converging region, $X_1 = \frac{x_{mp}}{2d_e}$, (b) the middle of the merging region, $X_2 = \frac{x_{cp}+x_{mp}}{2d_e}$ and (c) $5d_e$ downstream of the combined point, $X_3 = \frac{x_{cp}}{d_e} + 5d_e$.

an exponential trend of the form $\frac{U_{sym}}{U_m} = y_0 + Ae^{-\frac{(X_{mr}-x_0)}{t}}$ was fitted to the curves in Fig. 4-5b. In here, $X_{mr} = \frac{x-x_{mp}}{x_{cp}-x_{mp}}$ and x_0 and y_0 are the offset values, A is the amplitude and t is the decay constant, which are respectively equal to 0.02, 1.09, -1.06 and 0.37.

Figs.4-6a, 4-6b and 4-6c show the normalized one-dimensional mean streamwise velocity profiles in the middle of the converging region, $X_1 = \frac{x_{mp}}{2d_e}$, middle of the merging region, $X_2 = \frac{x_{mp}+x_{cp}}{2d_e}$ and $5d_e$ downstream of the combined point location, $X_3 = \frac{x_{cp}}{d_e} + 5d_e$, respectively. The transverse locations and the mean velocity are normalized by $y^+_{0.5}$ and U_m, respectively. It should be mentioned that as X_3 is located out of the range of PIV measurements for $S/d_e > 3.7$, the profiles are only shown for S/d_e = 1.8, 2.7 and 3.7 in Fig. 4-6c. Due to symmetry, the velocity profiles are only shown for the lower jet. It should be remarked that the X_1 location corresponds to x/d_e = 0.5, 1.1, 1.9, 3.8 and 5.4 for S/d_e = 1.8, 2.7, 3.7, 5.5 and 7.3, respectively. These locations are in the

potential core region for S/d_e = 1.8, 2.7 and 3.7 but in the developing region for S/d_e = 5.5 and 7.3. Since these locations are in the middle of the converging region, one distinct peak is observed. In the middle of the merging region, at X_2, due to the momentum exchange, the streamwise mean velocity on the symmetry line obtains 80% of the local maximum velocity. This is not surprising as the profiles in Fig. 4-5b showed that there is no effect of nozzle spacing ratio on the value of $\frac{U_{sym}}{U_m}$ within the merging region. At this location all the profiles collapse on top of each other for -0.5 < y^* < 0. However, as the jets' outer shear layer is still in its developing stage (see Fig. 4-4a), the velocity profile of S/d_e = 1.8 is not collapsing on top of the others for -1.5 < y^* < -0.5. The collapse of the profiles for S/d_e = 2.7, 3.7, 5.5 and 7.3 suggests that in addition to proper scaling with respect to $y^+_{0.5}$ and U_m, the extraction location with respect to the merging region must be similar in order to remove any effect of nozzle spacing and collapse the mean velocity profiles. At X_3, the profiles of S/d_e = 1.8, 2.7 and 3.7 collapse on top of each other showing that at 5d_e downstream of the CP, the nozzle spacing effects on the mean velocity are completely removed. For y^* < -0.5, the profiles still deviate from the self-similar single jet profile of [25]. It then can be concluded that although in the early stages of the combined region normalizing with respect to $y^+_{0.5}$ and U_m collapses the mean velocity profiles irrespective of nozzle spacing ratios, the mean flow still needs more downstream distances to show a behavior indistinguishable from a self-similar single jet.

Figs.4-7a and 4-7b show the downstream evolution of streamwise and transverse turbulence intensities along the jet centerline, respectively. The profiles are normalized by U_{max}. The streamwise turbulence intensity, u_{rms_c}, in Fig. 4-7a follows the single jet profile of [25] reasonably well. As it is evident from this figure, irrespective of the nozzle spacing, the streamwise turbulence intensity peaks at x/d_e = 5.3. The increase is due to the diffusion of turbulence, produced in the

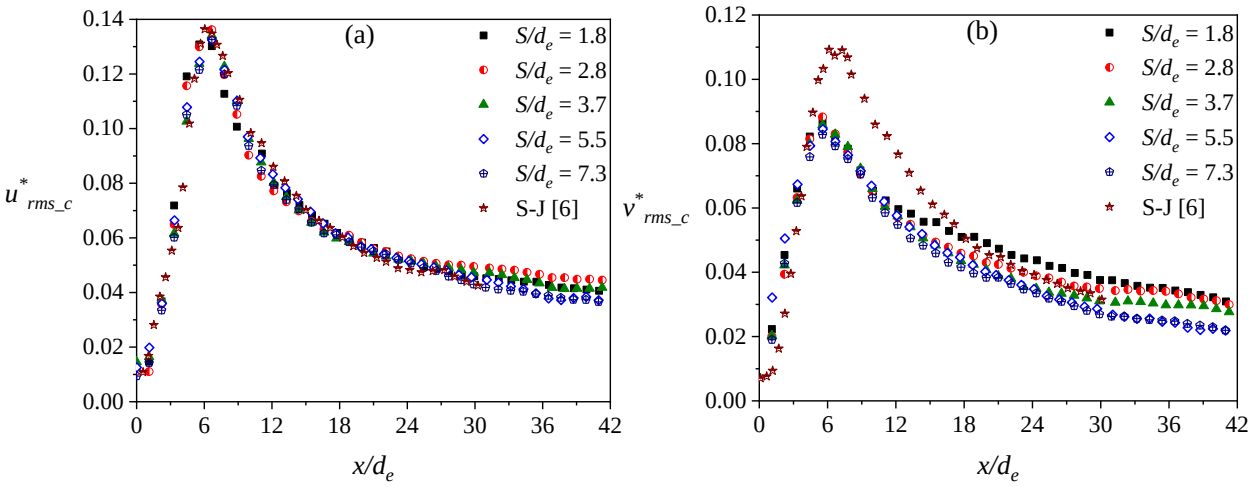

Fig. 4-7. Streamwise development along the jet centerline for (a) streamwise and (b) transverse turbulence intensities.

shear layers, towards the centerline of each jet [34]. Also, the location of the peak is downstream of the potential core region, where the breakdown of the vortical structures results in increased turbulence intensities on the centerline of the jets [25]. The peak location and values are, respectively, comparable to x/d_e = 6.0 and u_{rms_c}/U_{max} = 0.14 reported by [25]. The transverse turbulence intensity, v_{rms_c}, on the other hand, is affected by the merging of the jets centerlines in the combined point. As it is evident from Fig. 4-7b, downstream of the CP location, v_{rms_c} tends to decay slower at a smaller nozzle spacing, which means that as the jets' centerlines merge, the decay of large-scale fluctuations in the transverse direction reduces. In the present study, transverse turbulence intensity peaks to v_{rms_c}/U_{max} = 0.09 which is 18% lower than the peak observed in the single jet study of [25]. Its location is also 1d_e upstream at x/d_e = 5.6.

Figs.4-8a and 4-8b respectively show the downstream evolution of the streamwise, $u^*_{rms\_s}$, and transverse, $v^*_{rms\_s}$, turbulence intensities along the symmetry line, normalized by U_{max}. In comparison, it can be observed that the peak of $u^*_{rms\_s}$ is not only lower than $v^*_{rms\_s}$ but is also located further downstream for $S/d_e \leq 3.7$. The opposite holds for $S/d_e > 3.7$. For instance, the

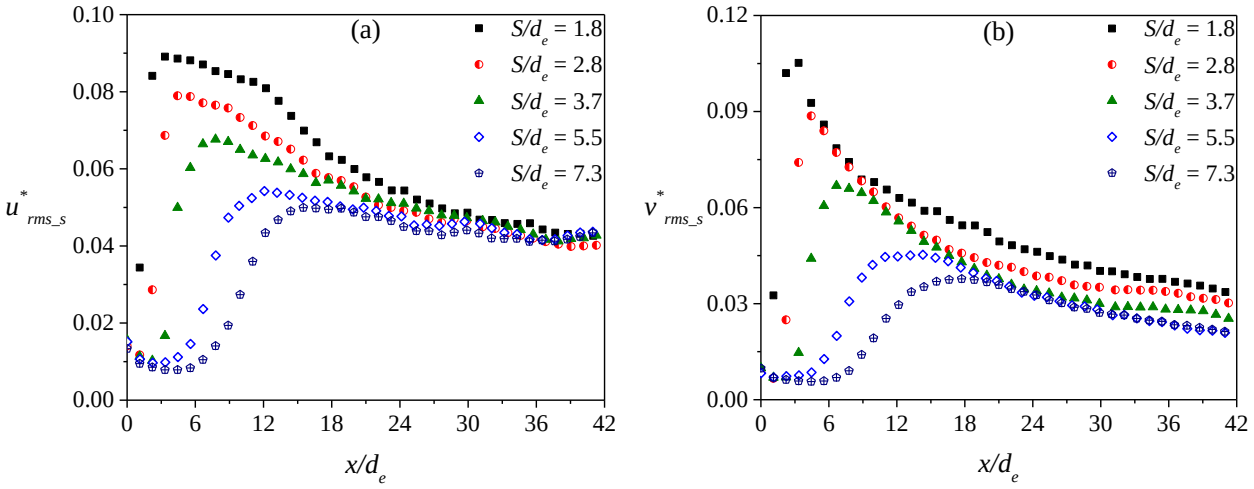

Fig. 4-8. Streamwise development along the symmetry line for (a) streamwise and (b) transverse turbulence intensities.

peaks of $u^*_{rms\_s}$ and $v^*_{rms\_s}$ are equal to $u^*_{rms\_sm}$ = 0.09 and $v^*_{rms\_sm}$ = 0.11, located at x_{mu}/d_e = 3.1 and x_{mv}/d_e = 2.8 for S/d_e = 1.8, while for S/d_e = 7.3, the peaks are equal to $u^*_{rms\_sm}$ = 0.05 and $v^*_{rms\_sm}$ = 0.04, located at respectively x_{mu}/d_e = 15.3 and x_{mv}/d_e = 17.7. As the level of turbulence intensities is an indication of large scale fluctuations, these opposing trends of $u^*_{rms\_s}$ and $v^*_{rms\_s}$ for $S/d_e \leq$ 3.7 and $S/d_e >$ 3.7 show that while the outcome of the interactions between the large scale coherent structures of the inner shear layers, increases the turbulence fluctuations irrespective of the nozzle spacing ratio. For $S/d_e \leq$ 3.7 this increment is more dominated in the transverse direction than the streamwise direction.

Figs.4-9a, 4-9b and 4-9c show the one-dimensional profiles of u_{rms} for the lower jet in the middle of the converging region, X_1, middle of the merging region, X_2 and 5d_e downstream of the combined point, X_3. Similar to the mean velocity profiles (Fig. 4-6), the turbulence intensity and transverse locations are normalized by U_m and $y^+_{0.5}$ and shown as u^*_{rms} and y^* respectively. At X_1, Fig. 4-9a, except for S/d_e = 7.3, all the profiles show two distinct peaks for the lower jet due to the existence of the inner and outer shear layers. The reason why u_{rms} does not show two peaks for

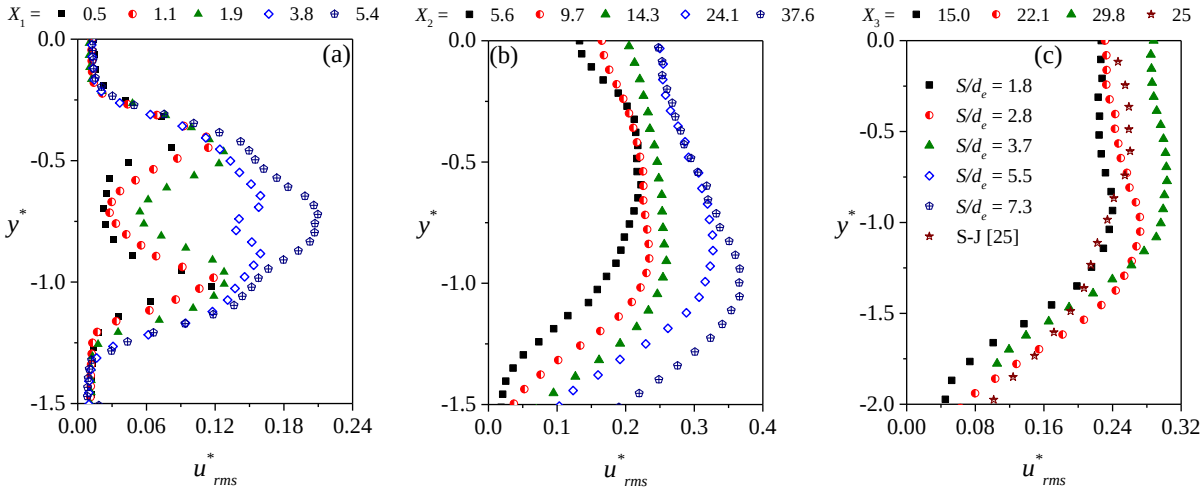

Fig. 4-9. Transverse profiles of the streamwise turbulence intensity at (a) middle of the converging region, $X_1 = \frac{x_{mp}}{2d_e}$, (b) middle of the merging region, $X_2 = \frac{x_{cp}+x_{mp}}{2d_e}$ and (c) 5de downstream of the combined point, $X_3 = \frac{x_{cp}}{d_e} + 5\text{de}$.

S/de = 7.3 is that in this case, the jets are so far from each other that $X_1 = 5.4d_e$ is downstream of the potential core region and in the vicinity of peak of $u^*_{rms\_c}$ (see Fig. 4-7a). As the nozzle spacing increases and the X_1 location moves further downstream, the peaks converge towards the jet centerline. At X_2, the profile of *S/de* = 1.8 shows a local maximum close to the jet centerline (y^* = -0.5) which is due to the turbulence diffused from the shear layers to the jet centerline. For *S/de* = 2.8, 3.7, 5.5 and 7.3, as nozzle spacing ratio increases, the X_2 location moves away from x_{mu}/d_e (the peak location of $u^*_{rms\_s}$). Thus, the difference between the u^*_{rms} values at the outer shear layer (y^* = -1) and the symmetry line (y^* = 0) increases. The lack of Kelvin-Helmholtz instabilities, which is the outcome of the interactions between the inner shear layers' structures, results in an uneven distribution of u^*_{rms} with respect to the jet centerline. This results in further convergence of the outer shear layer peak towards the symmetry line. Despite the profiles of mean streamwise velocity, the profiles of u_{rms} are not collapsing on top of each other at X_3. This was expected as

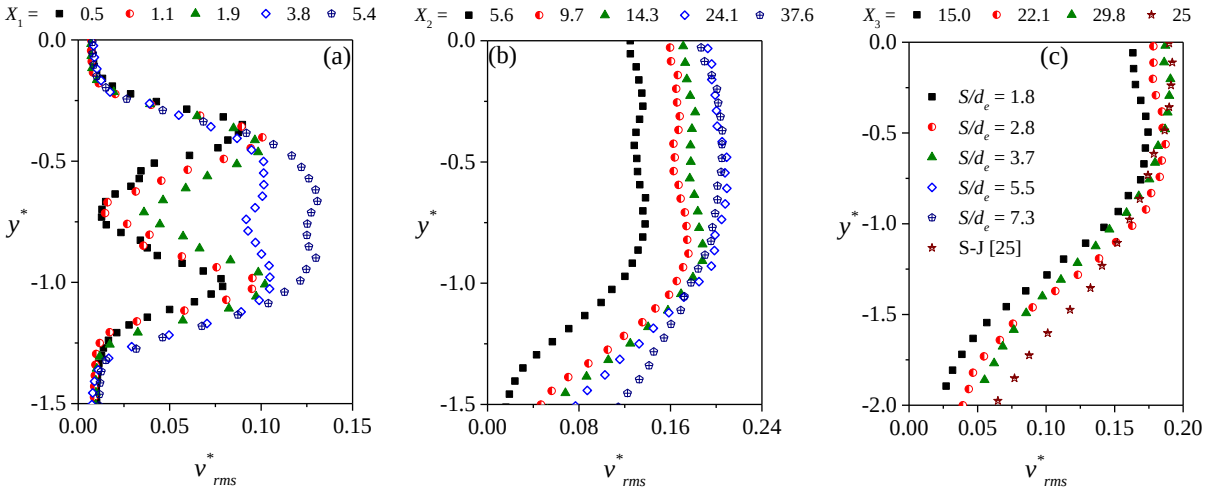

Fig. 4-10. Transverse profiles of the transverse turbulence intensity at (a) middle of the converging region, $X_1 = \frac{x_{mp}}{2d_e}$, (b) middle of the merging region, $X_2 = \frac{x_{cp}+x_{mp}}{2d_e}$ and (c) $5d_e$ downstream of the combined point, $X_3 = \frac{x_{cp}}{d_e} + 5d_e$.

compared to the mean flow, more downstream distances are required to remove the initial conditions effect from turbulence statistics. Figs. 4-10a, 4-10b and 4-10c show the one-dimensional profiles of transverse turbulence intensity. The normalization method as well as the extracted streamwise locations are the same as the ones presented for Figs. 4-6 and 4-9. Similar to u^*_{rms}, the profiles show two distinct peaks at X_1. However, as the profiles were extracted further downstream with the increase in nozzle spacing, the minima, which represent the center of the jet, are increasing and also the peaks are moving towards the centerline. This is dramatically affecting the results for the largest spacing ratio, $S/d_e = 7.3$, in which two peaks are barely observable as the profile was extracted at $X_1 = 5.4d_e$ which is in the vicinity of $x/d_e = 5.6$ reported for the maximum of transverse turbulence intensity along the centerline. In the middle of the merging region, as nozzle spacing increases and hence X_2, the profiles develop closer to self-similarity. Therefore, while the inner peaks are still distinguishable for $S/d_e = 1.8$, 2.8 and 3.7, a plateau is observable for $S/d_e = 7.3$. At X_3, the profiles of $S/d_e = 1.8$ and 2.7 still show the minimum on the symmetry line.

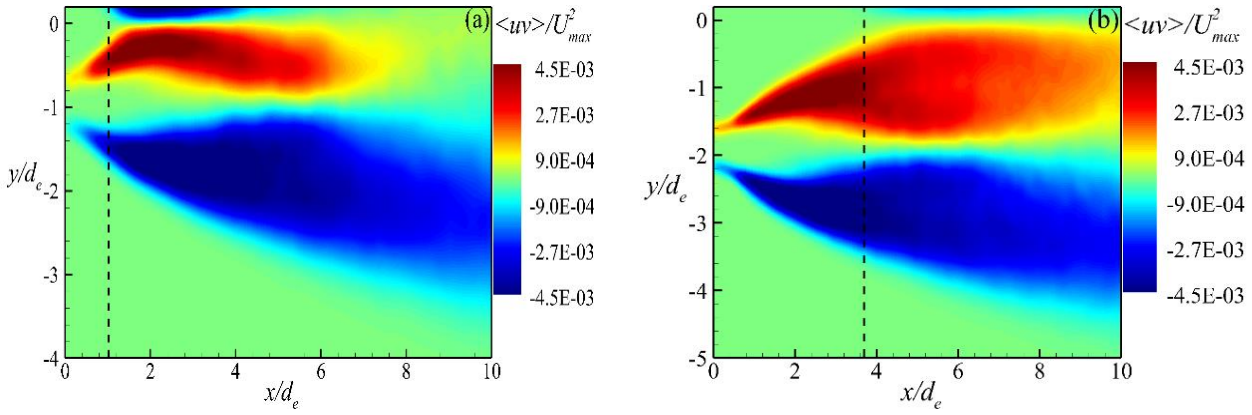

Fig. 4-11. Contour plots of Reynolds shear stress for (a) S/d_e = 1.8 and (b) S/d_e = 3.7.

In comparison to the profiles of streamwise turbulence intensity (Fig. 4-9c), the profiles of transverse turbulence intensity show more resemblance to S-J [25], suggesting that the latter will enter the self-similarity region sooner than the former. Similar sequence was speculated by Miller and Comings [4] for twin parallel plane jets.

Fig. 4-11 shows the contour plots of Reynolds shear stress, $\langle uv \rangle$, normalized by U^2_{max}. For brevity, the plots are only shown for $S/d_e = 1.8$ and $S/d_e = 3.7$ in Figs. 4-11a and 4-11b respectively. Also, due to symmetry, the contour plots are only shown for the lower jet. The dashed lines represent the location of the MP. Similar to free single jet, high absolute values of Reynolds shear stress are located in the shear layers of each jet. Therefore, there are one positive and one negative peak regions in each of the lower jet and upper jet. The Reynolds shear stress of the outer shear layer is intact of the adjacent jet and develops identically for all test cases. Meanwhile the Reynolds shear stress of the inner shear layer is severely affected by the adjacent jet. It can be observed that upon merging, the transverse development of the Reynolds shear stress of the inner shear layer is suppressed and as a result it cannot develop as freely as its counterpart in the outer shear layer. As

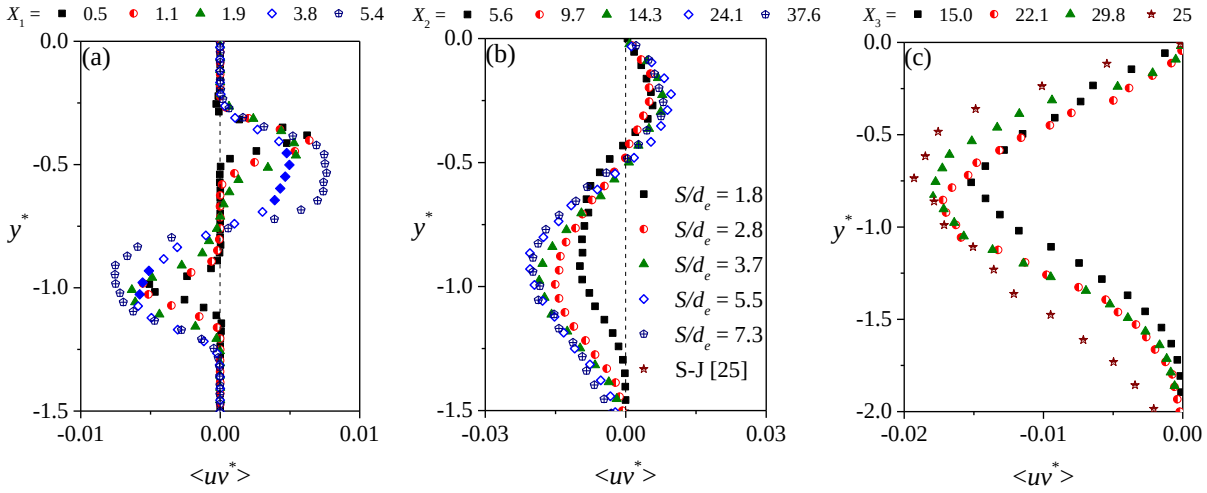

Fig. 4-12. Transverse profiles of the Reynolds shear stress at (a) middle of the converging region, $X_1 = \frac{x_{mp}}{2d_e}$, (b) middle of the merging region, $X_2 = \frac{x_{cp}+x_{mp}}{2d_e}$ and (c) $5d_e$ downstream of the combined point, $X_3 = \frac{x_{cp}}{d_e} + 5d_e$.

the spacing increases, the inner shear layers spread more freely before merging and therefore, the Reynolds shear stresses develop more in both the streamwise and transverse directions. For this reason, the similarity between the Reynolds shear stresses of the inner and outer shear layers increases as the nozzle spacing increases. For $S/d_e = 3.7$ for instance, a reasonable level of similarity can be observed between the inner and outer shear layers which is not the case for $S/d_e = 1.8$. Zang and New [17] also argued that for $S/d_e > 3$, the inner and outer shear layers develop freely in the near-field region ($0 \leq x/d_e \leq 7$).

Fig. 4-12 shows the one-dimensional profiles of Reynolds shear stress using similar scaling adopted for the mean velocity and turbulence intensities. Similar to the turbulence intensities, the Reynolds shear stress shows two distinct peaks which represent the inner and outer shear layers at X_1. For $S/d_e = 1.8$, 2.7 and 3.7 one can notice a zero Reynolds shear stress region between the inner and outer peaks due to the existence of potential core. The peaks of the inner and the outer shear

layers are comparable, showing that the adjacent converging inner shear layers do not suppress the maximum Reynolds shear stress. At X_2, the interactions have resulted in the suppression of the peak of Reynolds shear stress in the inner shear layer. However, compared to the outer shear layer, the peaks are almost collapsing on top of each other. This shows that in the middle of the merging region, the Reynolds shear stress of the inner shear layer is at the same decaying stage irrespective of nozzle spacing ratio. The outer shear layer on the other hand can develop freely upon discharge of the jets from the nozzles. Hence, at X_2, its corresponding Reynolds shear stress not only shows more transverse extent, but it shows higher peak value as nozzle spacing ratio increases. This results in the peak value of $<uv^*>$ = 0.02 for S/d_e = 5.5 and 7.3, which is equal to the peak value reported for the single jet of [25] (see Fig. 4-12c). At X_3 only one peak is present, which is an indication that the inner shear layers are completely merged. The profiles do not collapse on top of each other and still deviate from the self-similar single jet profile of [25]. The implication of this observation is that a longer downstream distance than examined in this study is required for self-similarity of Reynolds shear stress. However, it can be observed that as nozzle spacing increases, the profiles show more resemblance to the single jet profile of [25]. Hence, it is expected that the distance from the CP where Reynolds shear stress obtains self-similarity decreases as nozzle spacing increases.

Figs.4-13a and 4-13b show the contour plots of normalized instantaneous swirling strength for S/d_e = 1.8 and 3.7 respectively. Similar to single jet, the retrograde (counter-clockwise) and prograde (clockwise) vortical structures are formed along the jets' shear layers due to Kelvin-Helmholtz instability. These vortices tend to diffuse towards the jet centerline downstream of the potential core region. The formation of these counter-rotating vortical structures across the jet's shear layers has two outcomes. On one hand, the high momentum flow on jet centerline is advected

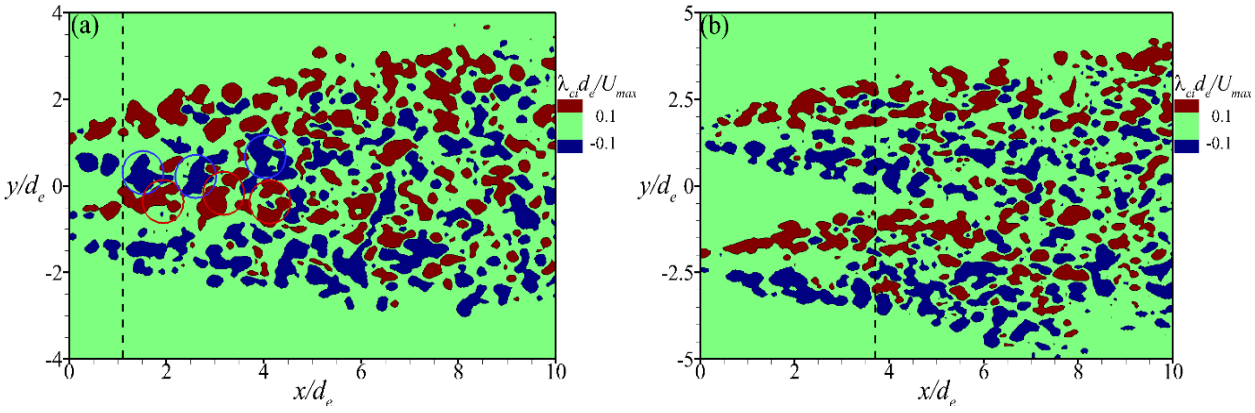

Fig. 4-13. Contour plots of instantaneous swirling strength for (a) S/d_e = 1.8 and (b) S/d_e = 3.7.

towards the shear layers and on the other hand, the ambient fluid is entrained into the jet envelope. The former results in the decay of local maximum velocity, U_m while the latter is responsible for spreading of the jet. Meanwhile, one can notice from Fig. 4-13a that for $1.1 < \frac{x}{d_e} < 5$, where the inner shear layers are in their early stages of interaction in the merging region, an organized staggered pattern of counter-rotating vortical structures is formed (shown by blue and red circles). This qualitatively resembles the von Karman vortex street in a wake of a bluff body. Comparatively speaking, this train of vortical structures cannot be identified in the merging region of S/d_e = 3.7 in Fig. 4-13b. The explanation for this inconsistency is that for S/d_e = 1.8, as the MP location is upstream of the potential core region, the inner and the outer shear layers are isolated and thus do not have any destabilizing effects on each other [10]. Retaining their coherency, the vortical structures tend to form the counter-rotating staggered pattern along the symmetry line as the inner shear layers get in contact with each other in the merging region. For S/d_e = 3.7, the inner shear layer structures are already destabilized by the interactions with the outer shear layer structures and hence the vortex street of counter-rotating vortical structures is not formed in the merging region. The findings are in line with the study of Zang and New [17], in which for S/d_e = 1.5 and

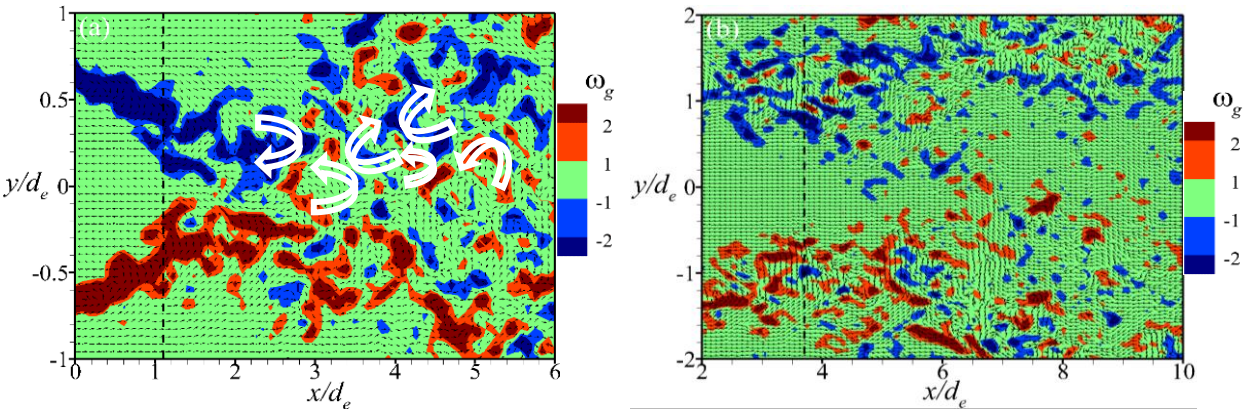

Fig. 4-14. Galilean decomposition of the instantaneous velocity field for (a) S/d_e = 1.8 and (b) S/d_e = 3.7.

2 they observed the formation of counter-rotating vortical structures, while this was not the case for S/d_e = 3.0.

In order to verify the above statement regarding the existence of counter-rotating vortical structures along the symmetry line, the Galilean decomposition method was applied to instantaneous velocity vector field. In this method, a convection velocity, U_{conv}, is subtracted from the instantaneous streamwise velocity in order to visualize the vortex cores that are advecting at the same velocity. Typically, the convection velocity is a fraction of a characteristic velocity in the flow field such as the centerline velocity. In here, a convection velocity of $U_{conv} = 0.58U_{max}$ was applied to the results presented in Fig. 4-14. The decomposed instantaneous vorticity field is also embedded in this figure. Although in Galilean decomposition it is impossible to visualize all vortex cores with a fixed value for advection velocity, one still can identify the existence of some counter-rotating coherent structures in Fig. 4-14a for S/d_e = 1.8. However, in Fig. 4-14b, there is no organized structure within the merging region. Therefore, the instantaneous results of the flow field proves the existence of counter-rotating vortical structures within the merging region for S/d_e < 3.7 only.

4.3. Conclusion

Effects of spacing ratio on the mean flow, turbulence intensities and Reynolds shear stress of rectangular twin jets were experimentally investigated. The spacing between the nozzles were set to S/d_e = 1.8, 2.7, 3.7, 5.5 and 7.3 and Reynolds number was fixed at Re_{de} = 10,000 for all of the test cases. The results showed that the locations of the merging and the combined points increase linearly with increasing spacing ratio. The combined point, however, was more affected by the change in the spacing ratio as the slope of its fitted line was more than 3.5 times of the one for the merging point location. This resulted in a longer merging region for larger nozzle spacing ratios. The mean flow showed a 38% decrease in its decay rate in the combined region compared to the converging and the merging regions. Thus, by increasing the spacing ratio, higher decay and spread rates can be achieved within a specific distance from the nozzle. Along the symmetry line, the streamwise mean velocity as well as turbulence intensities showed an abrupt increase towards a maximum in the immediate vicinity of the merging point location. By increasing the spacing ratio, the slope of the jump as well as the peak value were decreased. This resulted in 77%, 44% and 65% difference between the peaks of S/d_e = 1.8 and 7.3 for $\frac{U_{sym}}{U_{max}}$, ${u^*}_{rms\_s}$ and ${v^*}_{rms\_s}$ respectively. For $S/d_e \leq 3.7$, the transverse turbulence intensity along the symmetry line showed higher peak values compared to its streamwise counterpart while the opposite was observed for $S/d_e > 3.7$. The contour plots of Reynolds shear stress showed that as the spacing ratio between the nozzles increases, the inner shear layer is less suppressed by the converging adjacent shear layer and hence, more symmetry in the spatial development of Reynolds shear stress between the inner and the outer shear layers can be observed. The one-dimensional profiles suggested that by increasing the spacing ratio between the nozzles, the distance between the CP and the location where turbulence intensities and Reynolds shear stress obtain self-similarity, decreases.

Chapter 5

Investigation of large-scale coherent structures and momentum interference of twin rectangular jets

5.1. Introduction

Large-scale structures (LSS) play an important role in sustainability of turbulence. It is through these structures that the cascade of turbulence kinetic energy (TKE) from large to small scales of motion is accomplished. In free turbulent jets, large-scale vortical structures form along the interface between the jet and the ambient fluid. These structures play a dynamic role in the entrainment of ambient fluid into the jet envelop as well as the diffusion of high speed turbulent fluid towards the shear layers. In a free single jet, the shear layers are not confined and as a result, their vortical structures develop freely. Hence, the statistical properties and flow structures are symmetric with respect to the jet centerline and as a consequence, the LSS of the upper and lower shear layers show identical behavior. As shown in Fig. 5-1, the flow topology in a twin-jet configuration is comparatively more complex compared to a single jet. The jets with diameter/width of *d* are separated by the distance *S*. The inner and outer shear layers are shown in the figure. The transverse locations at which the streamwise mean velocity obtains half of its local maximum, are referred to as the jet half velocity-width locations. Therefore, in addition to the shear layers, there exist the jet half velocity-width of the outer and the inner shear layers (denoted as $y_{0.5}^{+}$ and $y_{0.5}^{-}$ respectively). Eventually, the inner shear layers will merge at the so called "merging point" (MP). The region from nozzle exit to the MP is called the "converging region".

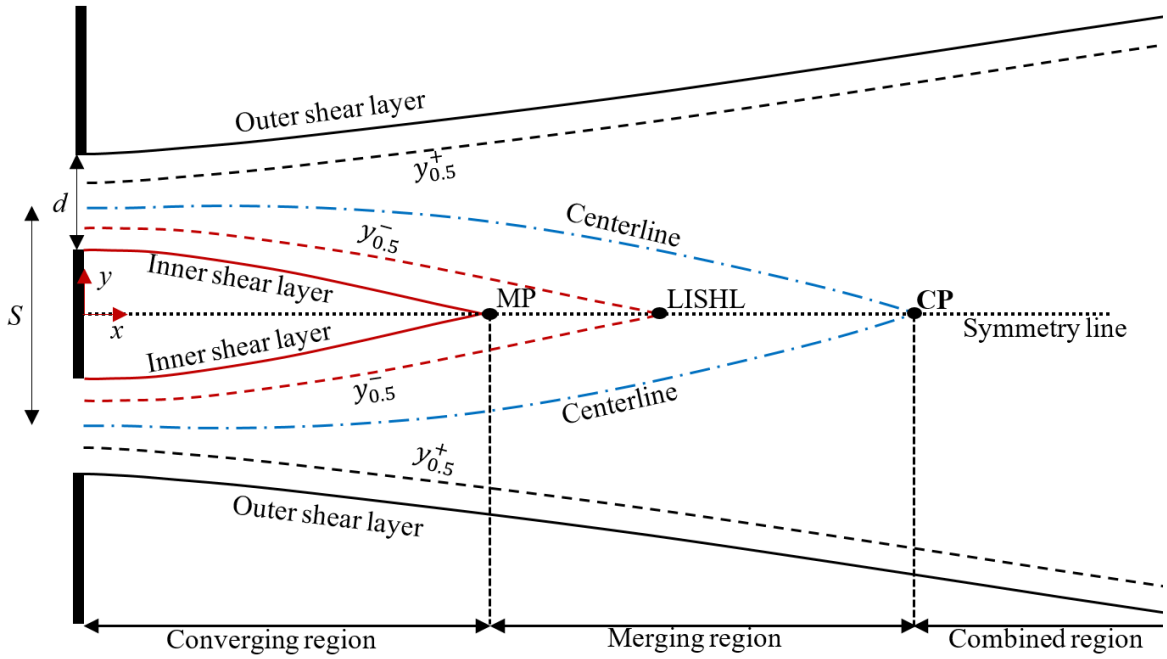

Fig. 5-1. Schematic of twin jets.

By having identical conditions for the jets, the MP is located in between the jets along an imaginary line, called the "symmetry line". In a similar fashion, the half velocity-widths of the inner shear layers, $y^-_{0.5}$, also meet along the symmetry line. Evidently, this is located downstream of the MP and hereafter is referred to as the last inner shear layer location (LISHL). Downstream of the MP location, as the jets are in physical contact, various momentum transport processes occur. The "merging region" starts at the merging point and ends at the streamwise location where there is no momentum deficit between the jets. At this location the flow characteristics are not the ones for two individual jets, but more like a single jet. This location is hence called the "combined point" (CP). Downstream of the CP, lies the combined region in which the newly formed combined jet behaves increasingly similar to a free single jet as it progresses downstream.

The evolution and statistical properties of the outer shear layers of a twin-jet configuration are dynamically similar to those observed in free single jets [15, 16, 20]. In contrast, the mutual

interaction between the adjacent inner shear layers gives rise to confinement effects and turbulent transport phenomena that could be markedly different than in their single jet counterparts, especially for low nozzle spacing ratios. It is also legitimate to expect that the LSS in the inner and outer shear layers of twin jets go through different mechanism. In particular, the LSS in the inner shear layers are expected to interact strongly in the merging region and have a key dynamic role in momentum transfer between the jets. Evidently, the existence of such interactions complicates the flow physics.

In spite of the need to understand the characteristics of the LSS in twin jets, especially within the inner shear layers, and their impact on the flow physics as the nozzle spacing is varied, the literature on this topic is quite limited. Ko and Lau [11] were the first to investigate the LSS in twin jets and examined the converging and merging regions of twin parallel plane jets. It was observed that the peak in power spectral density diminishes as the inner shear layer develops in the merging region. Two different processes were suggested for the pairing of vortical structures along the inner shear layer. In one process, small initial vortices pair up to form a larger structure which is more elongated in the transverse direction and inherits the rotational preferences of its ancestors. In the other process, the successive vortices amalgamate to form a new structure which is more elongated in the streamwise direction. The latter was shown to decay more slowly than the former. Frequency analysis performed in subsequent studies by Anderson *et al.* [7], Hsu *et al.* [9], on twin parallel plane and round jets by Zang and New [17], showed distinct peaks along the shear layers. The corresponding Strouhal (St) numbers of these peaks were shown to be different for the inner and outer shear layers. For instance, in the study of Zang and New [17], the St number in the outer shear layer was independent of the spacing ratio and equal to St = 0.69, a result that was in agreement with the empirical relation of Becker and Massaro [35] for vortex formation at jet shear

layer. In contrast, the St number in the inner shear layer was shown to be a function of the spacing ratio between the nozzles. For example, Hsu *et al.* [9] observed that the St number for the case of S/d = 1.7 is 33% lower than that observed for S/d = 2.0. Similarly, Anderson *et al.* [7] reported a 25% decrease in the St number when the spacing ratio was reduced from S/d = 2.67 to 1.50. The trends in these studies clearly indicate that by increasing the spacing ratio, the progress of LSS along the inner shear layer becomes more similar to the outer shear layer counterpart. Mondal *et al.* [10] and Zang and New [17] reported formation of counter-rotating structures from the inner shear layers in the converging region. They argued that this staggered pattern of vortices with opposite signs, is qualitatively similar to von-Kármán vortex street typically observed in a wake of a bluff body. Further frequency analysis by Zang and New [17] along the symmetry line for S/d = 1.5 revealed two peaks at 4.2 Hz and 2.1 Hz (corresponding to St = 0.68 and 0.34 respectively). The authors attributed the first peak to vortex formation frequency of the inner shear layer (which was close to 4.4 Hz, reported for vortex generation frequency of the inner shear layer at nozzle exit). The second peak was, however, attributed to the shedding frequency of the inner shear layer structures, as it corresponds to St = 0.34 which is close to St = 0.24 to 0.34, reported for vortex shedding frequency of a bluff body [18].

In a recent study by Aleyasin *et al.* [36] the LSS of twin round jets were investigated for S/d_e = 2.8. In the converging region the swirling strength results showed higher peak for the inner shear layer compared to the outer shear layer. At the merging point however, the peaks became similar. The joint probability density function contours revealed that the turbulent flow on the symmetry line is more isotropic compared to the shear layers. Along the inner shear layer, the contours were aligned along the Q_2 and Q_4 quadrants. These quadrants were respectively associated with the entrainment of low-speed fluid from the inner shear layer toward the centerline and diffusion of

Table 5-1. Streamwise and transverse locations used for extraction of the results.

	Streamwise locations (x/d_e)				
Spacing ratio (S/d_e)	Middle of converging region	$0.1d_e$ downstream of the MP	LISHL	Middle of merging region	$1d_e$ upstream of the CP
1.8	0.6	1.2	2.9	4.6	7.0
3.7	1.9	3.8	8.3	12.5	20.2

high-speed fluid from the jet core to the inner shear layer. Further analyses using the weighted joint probability density function showed that the Q_4 event has higher contribution in production of Reynolds shear stress along the inner shear layer.

The above review provides a clear evidence of the effects of the adjacent jets on the development of LSS along the inner shear layers. The main focus in these studies was in the converging region. However, it is in the merging region that the jets get in physical contact through interactions. The aim of the present study is to provide a better understanding of the development of LSS in the converging and merging regions and examine how changing the spacing ratio could affect this. The experiments were conducted using PIV for five nozzle spacing ratios, and the structural analysis was performed using two-point correlation, joint probability density function (JPDF), swirling strength and analysis of the turbulent/non-turbulent interface (TNTI). The remainder of this paper is organized as follows: in section 5.2, the results are presented and discussed, and in section 5.3, major findings of this research are summarized.

The study adopts five spacing ratios. Although all five datasets will be used in our analyses, we highlight two datasets of S/d_e = 1.8 and 3.7. The reason these two datasets are selected is that they are significantly different in value and facilitate a good comparative study of the nozzle spacing effects on LSS. For convenience important parameters and characteristic streamwise locations associated with these two nozzle setups are summarized in Table. 5-1.

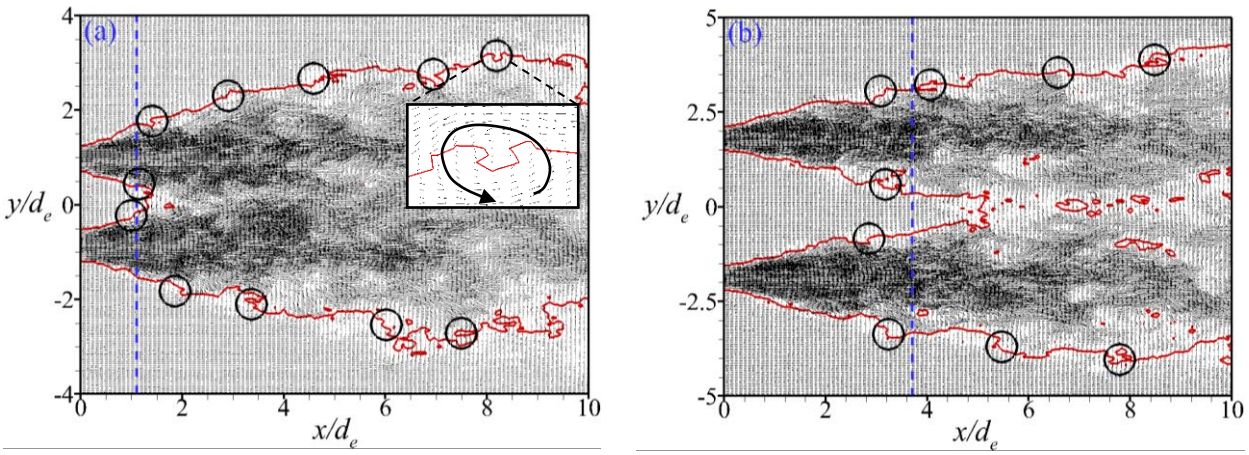

Fig. 5-2. Galilean decomposition of the instantaneous velocity vector field for (a) $S/d_e = 1.8$ and (b) $S/d_e = 3.7$.

5.2. Results and discussion

5.2.1. Instantaneous flow visualization

In order to develop a general understanding of the spatial development of twin jets, the instantaneous velocity vector field is shown in Figs. 5-2a and 5-2b for S/d_e = 1.8 and 3.7, respectively. Galilean decomposition is applied to instantaneous streamwise velocities to reveal the vortical structures in the jets. Evidently, the vortex cores are moving with different speeds. In order to facilitate the discussion, a convection velocity was defined to be $U_{conv} = 0.15U_{max}$, following Tay *et al.* [37]. The red contour lines represent the locations in which the instantaneous velocity is equal to the convection velocity. The cores of vortices moving with this convection velocity can then be identified along these red contour lines. A pattern of recurrent large-scale vortical structures can be identified along the outer shear layers. These regions are shown by circles. Similar phenomenon can be identified in the inner shear layers. The dashed vertical line represents the MP, which is the streamwise location where mean streamwise velocity along the symmetry line becomes $0.015U_{max}$ [38, 39]. Although the same convection velocity is applied to

both S/d_e = 1.8 and 3.7, the streamwise location where the red contour lines merge on the symmetry line is closer to the MP in the case of

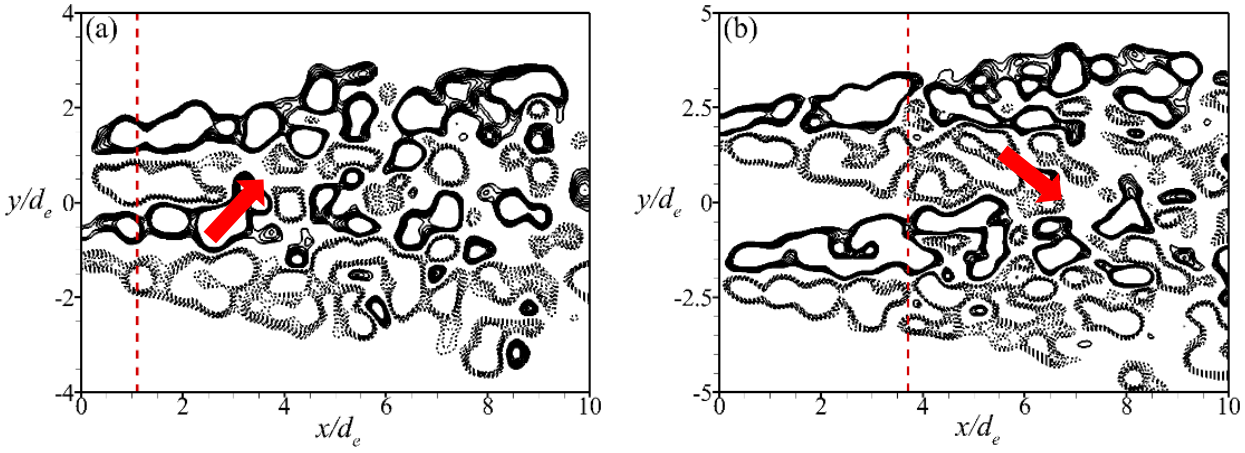

Fig. 5-3. Instantaneous swirling strength contours for (a) S/d_e = 1.8 and (b) S/d_e = 3.7.

S/d_e = 1.8 compared to S/d_e = 3.7. By comparing other test cases (not shown), it was observed that by increasing the spacing ratio the contour lines merge at further downstream of the MP location. For instance, for the case of S/d_e = 2.8 the distance between the MP and merging location of the contour lines is $\frac{\Delta x}{d_e}$ = 0.9, which is in-between $\frac{\Delta x}{d_e}$ = 0.2 and $\frac{\Delta x}{d_e}$ =1.3 for the cases of S/d_e = 1.8 and 3.7 respectively. This shows that the vortical structures that evolve into the merging region have higher convection velocity for a smaller spacing ratio. The higher density of velocity vectors in the merging region in Fig. 5-2a is the result of this difference, and can also be interpreted as a manifestation of more intense interactions in the merging region at a smaller spacing ratio.

The swirling strength is also used to visualize the vortical structures in Figs. 5-3a and 5-3b for S/d_e = 1.8 and 3.7, respectively. Fig. 5-3 shows the topology of counter-rotating vertical structures along the shear layers with solid and dashed contour lines representing the counter-clockwise (CCW) and clockwise (CW) vortices, respectively. Along the outer shear layers, the CCW and CW vortices respectively are dominant in the upper and lower jets within the region that extends

from the nozzle exit down to $x/d_e \cong 3.0$, which was shown to be the end of the potential core region [38]. Further downstream, counter-rotating vortices from the inner shear layers are shed into the outer shear layers and vice versa. As the inner shear layers approach each other, their counter-rotating vortices form a staggered pattern along the symmetry line; this is more clear in the case of $S/d_e = 1.8$ as the inner shear layers are initially closer to each other. Zang and New [17] also observed this train of vortical structures for $S/d_e < 3.0$. As the inner shear layers merge, their counter-rotating vortical structures shed into each other's shear layers, which is similar to the observation made for the outer shear layers. As indicated by arrows in Fig. 5-3, the instantaneous contours show the shedding of a CCW vortical structure from the lower jet into the upper jet for $S/d_e = 1.8$, and vice versa for $S/d_e = 3.7$. The destabilizing effect of these penetrations has two possible outcomes: it diminishes the coherency of inner shear layers, and leads to an amalgamation of counter-rotating structures within the jets.

5.2.2. Two-point correlation

One of the widely adopted methods for extracting spatial information from LSS is two-point correlation. The mathematical formulation for the two-point cross-correlation is given in Eqn (5-1) below:

$$R_{uv}(x_{ref}, y_{ref}, \Delta x, \Delta y) = \frac{\langle u(x_{ref}, y_{ref}) v(x_{ref} + \Delta x, y_{ref} + \Delta y) \rangle}{\sigma_u(x_{ref}, y_{ref}) \sigma_v(x_{ref} + \Delta x, y_{ref} + \Delta y)} \qquad \text{Eqn (5-1)}$$

where $u(x, y)$ and $v(x, y)$ are two fluctuating velocities whose two-point correlation is required; (x_{ref}, y_{ref}) is the reference location; Δx and Δy are the spatial separation between u and v in the streamwise and transverse directions respectively; and σ_u and σ_v are the root-mean-square values of u and v at (x_{ref}, y_{ref}) and $(x_{ref} + \Delta x, y_{ref} + \Delta y)$, respectively. The correlation here is shown in the format of R_{uv}^i, in which i denotes the direction, and u and v are velocity fluctuations. For

instance, R_{uu}^{x} shows the auto-correlation of streamwise velocity fluctuation along the streamwise direction.

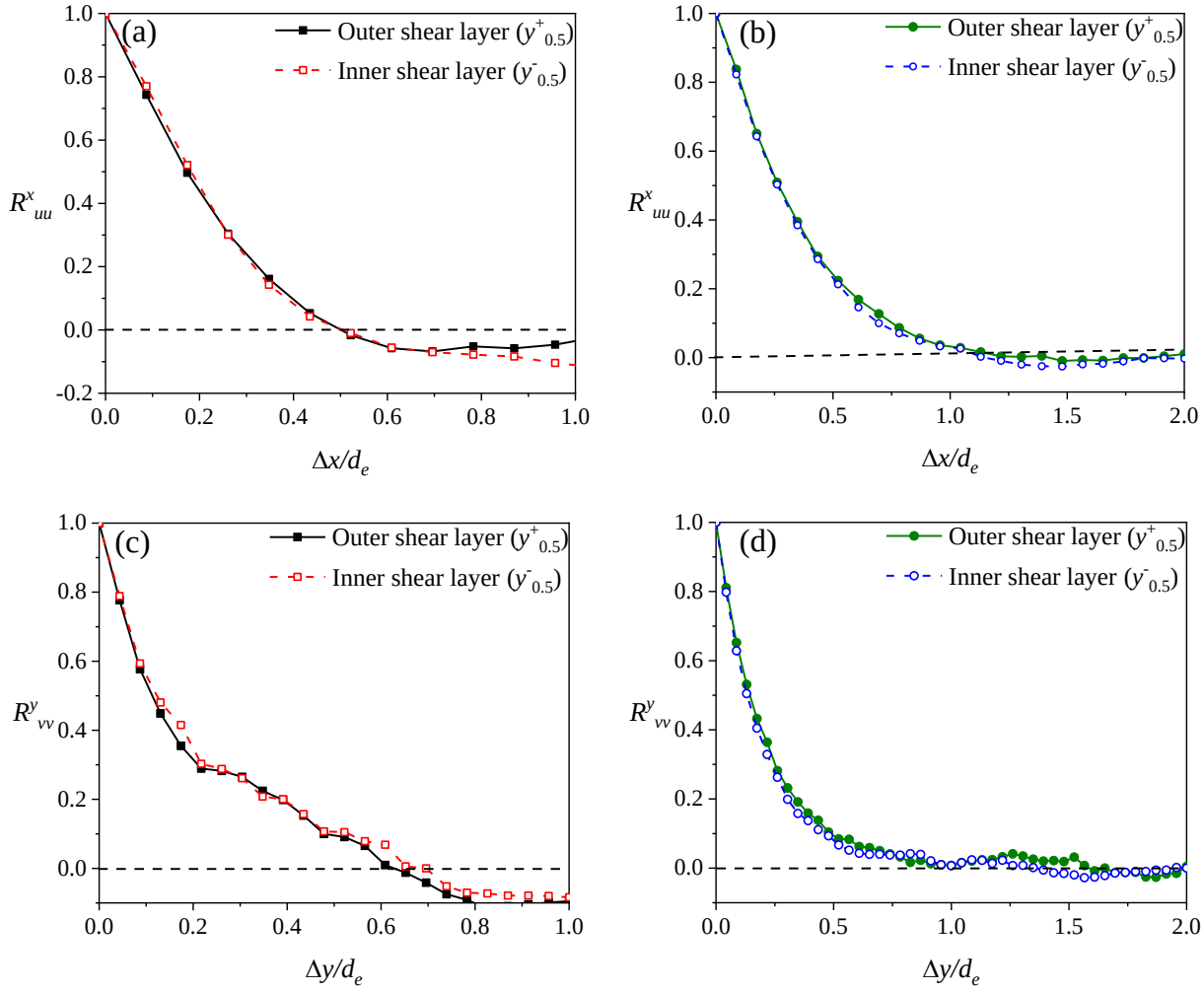

Fig. 5-4. Profiles of two-point correlation coefficient (a) and (b) R_{uu}^{x} for S/d_e = 1.8 and 3.7 respectively and (c) and (d) R_{vv}^{y} for S/d_e = 1.8 and 3.7 respectively.

As remarked earlier, it is expected that the merging of the jets will affect the development of LSS along the inner shear layers. In order to investigate the effect of these interactions, plots of two-point correlation within jet half velocity width of the outer shear layer ($y_{0.5}^{+}$) and inner shear layer ($y_{0.5}^{-}$) in the vicinity of the merging point and at last inner shear layer location (see Fig. 5-1 and Table. 5-1) are shown in Figs. 5-4 to 5-7 respectively. Figs. 5-4a and 5-4b show 1D profiles

of the auto-correlation coefficient of the streamwise fluctuating velocity in the streamwise direction (R_{uu}^{x}) at 0.1d_e downstream of their MP for S/d_e = 1.8 and 3.7, respectively. Since the jets for the case of S/d_e = 3.7 merge later, the R_{uu}^{x} profiles in Fig. 5-4b decay more slowly and their zero-crossing or decorrelation location of $\Delta x/d_e$ = 1 is approximately twice as large as in the case for S/d_e = 1.8. Although the jets are in the merging region, it is interesting to notice that the streamwise correlation for the inner and outer shear layers collapse irrespective of the spacing ratio. Since the merging point for the jets is only at 0.1d_e upstream of the location where these profiles were obtained, the LSS located at $y_{0.5}^{-}$ has not yet been exposed to a strong interaction, a situation that is similar to the outer shear layer. This is also the case for R_{vv}^{y} shown in Figs. 5-4c and 5-4d for S/d_e = 1.8 and 3.7 respectively. Two-point auto-correlation results of Aleyasin *et al.* [36] also showed that at the merging point, the spatial extent of structures along the outer and inner shear layers are comparable.

Fig. 5-5 shows the cross-correlation coefficient in the streamwise direction (R_{uv}^{x}) at 0.1d_e downstream of the MP for S/d_e = 1.8 (Fig. 5-5a) and 3.7 (Fig. 5-5b). Similar to the auto-correlation coefficients (Fig. 5-4), the cross-correlation coefficient along the inner and outer shear layers are identical. Comparing Fig. 5-5a with Fig. 5-5b, however, shows that by increasing the spacing ratio, at the merging point, the maximum cross-correlation coefficient decreases. An identical trend between the outer and inner shear layers is also observed for R_{uv}^{y} in Figs. 5-5c and 5-5d.

A significant effect of interactions on the size of large-scale structures and hence their spatial correlation can be noticed at LISHL, as shown in Fig. 5-6. For example, one can clearly identify a lower decay of R_{uu}^{x} for the outer shear layer for S/d_e = 1.8 and 3.7 in Figs. 5-6a and 5-6b, respectively. Unlike the preceding location, the intense interaction at LISHL causes the large-scale streamwise velocity fluctuations along the inner shear layers become uncorrelated faster than their

outer shear layer counterparts. Aleyasin *et al.* [36] had also similar observation for S/d_e = 2.8. They argued that as the entrainment of the ambient fluid in the merging region is solely through the outer shear

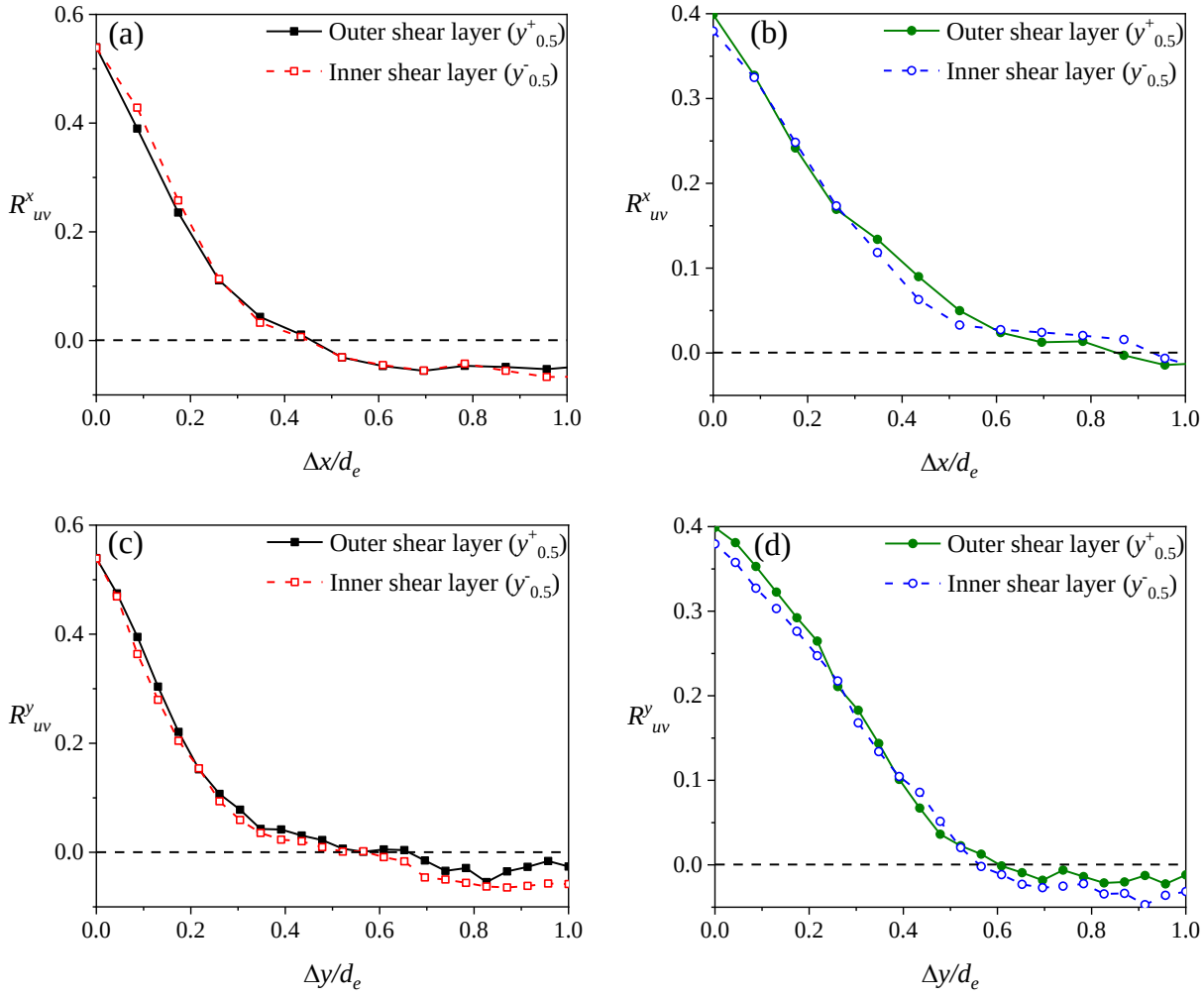

Fig. 5-5. Profiles of cross-correlation coefficient (a) and (b) R^x_{uv} for S/d_e = 1.8 and 3.7 respectively and (c) and (d) R^y_{uv} for S/d_e = 1.8 and 3.7 respectively.

layer, the growth in the size of LSS is faster compared to the inner shear layer. As is evident in Fig. 5-6 for the case of S/d_e = 1.8, the profile of the inner shear layer goes to zero at $\Delta x/d_e$ = 0.8. With an additional separation of 1.5d_e from the reference point, the profile for the outer shear layer also goes to zero at $\Delta x/d_e$= 2.3. For S/d_e = 3.7, the profiles approach zero at larger streamwise

distances, at $\Delta x/d_e$ = 5.5 and 7.0, for the outer and inner shear layers, respectively. Similar to the case of S/d_e = 1.8, the difference between the characteristic length scales (corresponding to $\Delta x/d_e$ = 5.5 and 7.0) of the outer and inner shear layers in the case of S/d_e = 3.7 is also 1.5d_e. This indicates

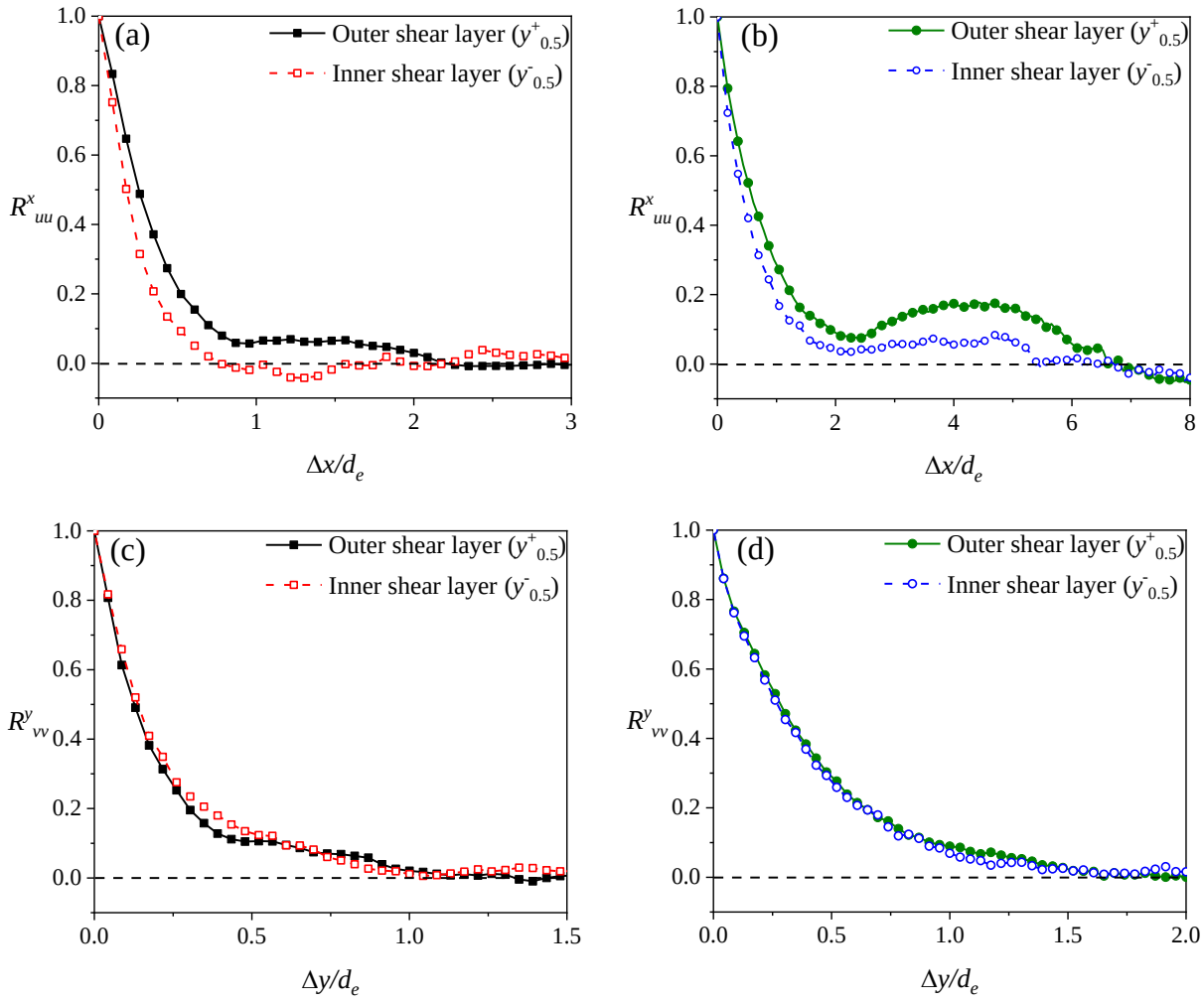

Fig. 5-6. Profiles of two-point correlation coefficient (a) and (b) R^x_{uu} for S/d_e = 1.8 and 3.7 respectively and (c) and (d) R^y_{vv} for S/d_e = 1.8 and 3.7 respectively.

that at LISHL, the difference in the characteristic length scales as represented by the intercepts of R^x_{uu} between the outer and inner shear layers is independent of the spacing ratio. In contrast to R^x_{uu}, the profiles of R^y_{vv} are identical for outer and inner shear layers in Figs. 5-6c and 5-6d. This

shows that the interactions of LSS within the jet do not affect the correlation of their transverse fluctuations (and the associated transverse length scale of turbulence structures).

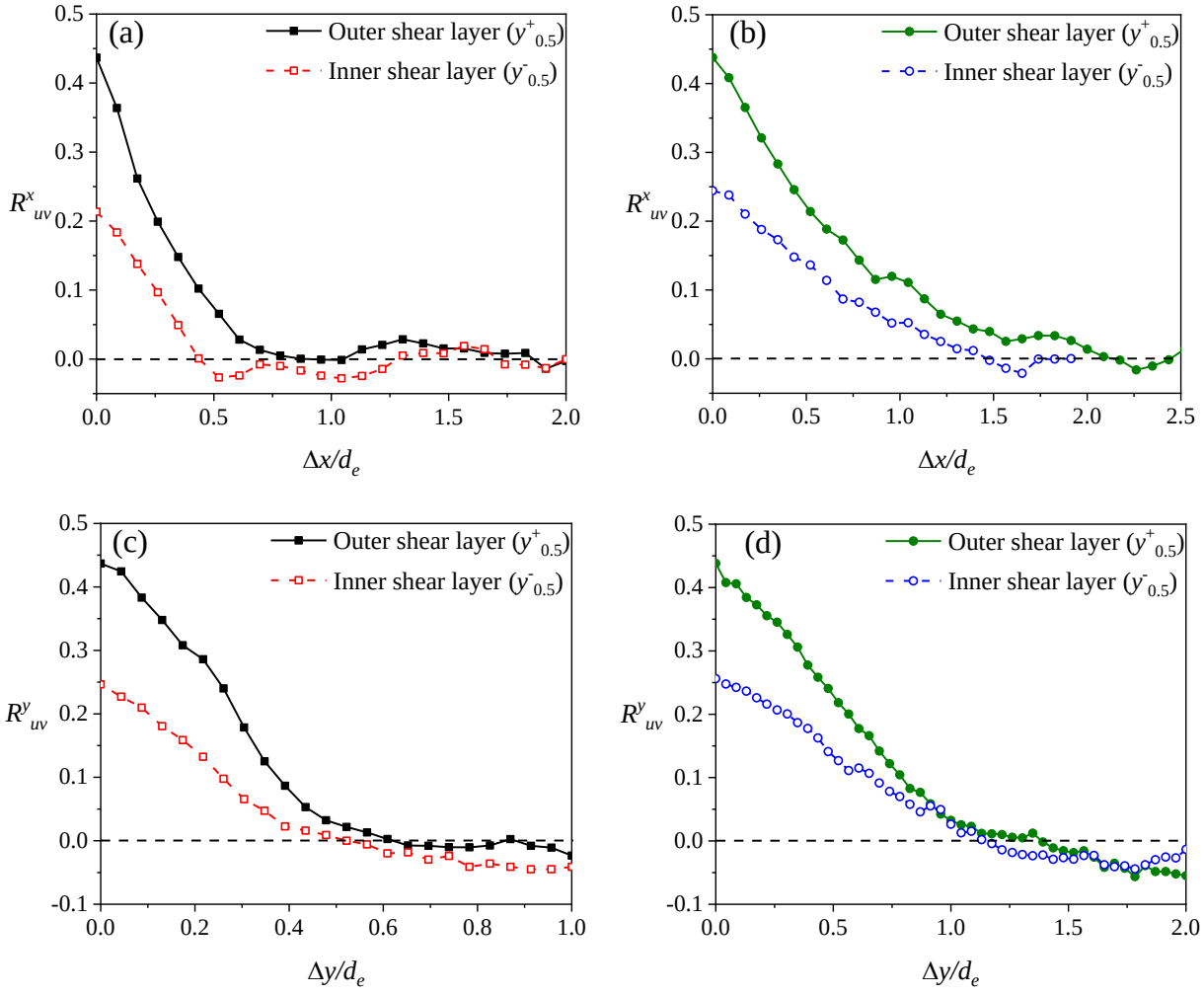

Fig. 5-7. Profiles of cross-correlation coefficient (a) and (b) R^x_{uv} for S/d_e = 1.8 and 3.7 respectively and (c) and (d) R^y_{uv} for S/d_e = 1.8 and 3.7 respectively.

Fig. 5-7 shows the cross-correlation coefficient at LISHL for the inner and outer shear layers for S/d_e = 1.8 and 3.7. For both test cases, it is noticed that R^x_{uv} for the inner shear layer not only decays faster but also has a lower peak value compared to the outer shear layer. Thus, due to interaction between LSS, the streamwise and transverse fluctuations become less correlated both in magnitude and spatial extent. For the case of S/d_e = 1.8, the inner and outer shear layers approach

zero at $\Delta x/d_e$ = 0.4 and 1.0. For the case of S/d_e = 3.7, the value increases to $\Delta x/d_e$ = 1.5 and 2.1 for inner and outer shear layers, respectively. However, the difference is still similar and equal to 0.6d_e. Recall that similar behavior was observed in Figs. 5-6a and 5-6b for R_{uu}^{x}. The effect of nozzle spacing can be observed on the maximum of R_{uv}^{x} for the inner shear layer. For S/d_e = 1.8 and 3.7, the maximum value is R_{uv}^{x} = 0.21 and 0.25, respectively. Hence, by increasing the spacing ratio, as interactions become less intense in the merging region, the maximum correlation between streamwise and transverse velocity fluctuations becomes less affected.

As is indicated by Figs. 5-7c and 5-7d, although the value of R_{uv}^{y} for the inner shear layer still decays faster than the outer shear layer, the location where it crosses zero is not significantly different than that for the outer shear layer. Specifically, the differences are 0.1d_e and 0.2d_e, for S/d_e = 1.8 and 3.7, respectively. These two values are comparatively lower than 0.6d_e for R_{uv}^{x}. This is an indication that the cross-correlation is less sensitive to interactions along the transverse direction compared to the streamwise direction.

5.2.3. Integral length scale

The size of LSS is quantified through integral length scale which is evaluated as the area under the correlation coefficient from the reference or self-correlation point (x_r and y_r) to the first zero-crossing point (x' and y'). Of special interest are the longitudinal and transverse integral length scales which are expressed as respectively:

$$I_{uu}^{x} = \int_{x_r}^{x'} R_{uu}^{x} dx \qquad \text{Eqn (5-2)}$$

$$I_{vv}^{y} = \int_{y_r}^{y'} R_{vv}^{y} dx \qquad \text{Eqn (5-3)}$$

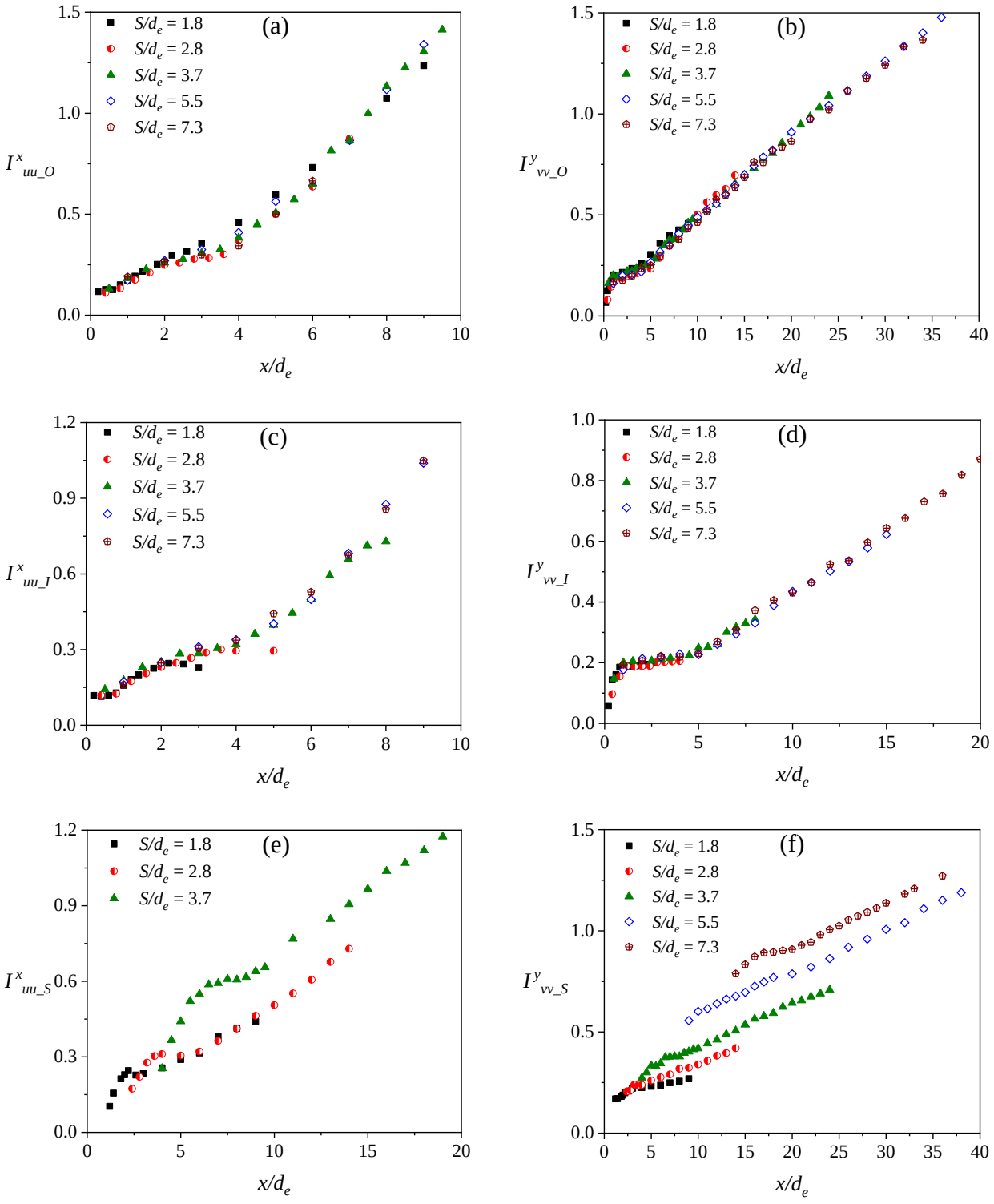

Fig. 5-8. Streamwise development of the integral scales, (a) $I^x_{uu\_O}$, (b) $I^y_{vv\_O}$, (c) $I^x_{uu\_I}$, (d) $I^y_{vv\_I}$, (e) $I^x_{uu\_S}$ and (f) $I^y_{vv\_S}$.

Fig. 5-8 shows I_{uu}^{x} and I_{vv}^{y} values obtained at selected several streamwise locations along the inner and outer shear layers as well as the symmetry line. As was expected, the profiles of $I_{uu\_O}^{x}$ collapse on top of each other (Fig. 5-8a), which implies that nozzle spacing does not affect the development of large-scale structures along the outer shear layer. The development of $I_{uu\_O}^{x}$ consists of an initial region from the nozzle exit down to $x/d_e = 2.0$. This is followed by a transition region, $2.0 < x/d_e < 4.0$, where $I_{uu\_O}^{x}$ is almost constant and equal to $I_{uu\_O}^{x} = 0.28$. Beyond the transition region, $I_{uu\_O}^{x}$ increases linearly with the downstream distance. The slope of this region is independent of spacing ratio and equal to $a_{uu\_O}^{x} = 0.209$. Qualitatively similar trend can be observed for $I_{vv\_O}^{y}$ in Fig. 5-8b. The profiles for different spacing ratios also collapse on top of each other. Compared to Fig. 5-8a, in the linear region, the slope is $a_{vv\_O}^{y} = 0.039$ which is an order of magnitude lower than $a_{uu\_O}^{x}$.

Development of integral length scale along the inner shear layer is shown in Figs. 5-8c and 5-8d. In Fig. 5-8c, $I^{x}_{uu\_I}$ shows a resemblance to its counterpart along the outer shear layer. Thus, as long as the inner shear layer is in the converging region, the value of $I^{x}_{uu\_I}$ is independent of the spacing ratio. However, as the inner shear layer enters the merging region, $I^{x}_{uu\_I}$ tends to decrease. This can be explained by the interactions as they also result in faster decay of R^{x}_{uu} for the inner shear layer in Figs. 5-6a and 5-6b. It was observed in Figs. 5-6c and 5-6d that the interactions do not affect R^{y}_{vv} of the inner shear layer. Similarly, one can observe in Fig. 5-8d that even in the merging region, $I^{y}_{vv\_I}$ does not decrease and follows the same trend observed for $I^{y}_{vv\_O}$. The slope in the linear region for $S/d_e = 5.5$ and 7.3 (as they have the most delayed MP) is $a^{y}_{vv\_I} = 0.040$, which is equal to $a^{y}_{vv\_O}$ reported for the outer shear layer.

In the early merging region, as the reference locations of correlation were close to the MP, an asymmetry was observed in the profiles of R^{x}_{uu} along the symmetry line, with the left tale being

shorter than the right one. Hence, the correlation coefficient decayed faster on left tale compared to the right tale. As a consequence, different values for $I^x_{uu\_S}$ were obtained based on Eqn (5-2).

Table 5-2. Slopes of integral length scale profiles in the linear region.

	Outer shear layer		Inner shear layer		Symmetry line	
S/d_e	$a^x_{uu\_O}$	$a^y_{vv\_O}$	$a^x_{uu\_I}$	$a^y_{vv\_I}$	$a^x_{uu\_S}$	$a^y_{vv\_S}$
1.8	0.209	0.039	-	-	0.048	0.010
2.8	0.209	0.039	-	-	0.048	0.017
3.7	0.209	0.039	-	-	0.048	0.021
5.5	0.209	0.039	-	0.040	-	0.023
7.3	0.209	0.039	-	0.040	-	0.023

Expectedly, as the streamwise distance increases, the value of $I^x_{uu\_S}$ of the right tale decreases while it increases for left tale. After some streamwise distance, the values became identical and R^x_{uu} profiles showed symmetry. The length of the region with asymmetry was observed to increase with an increase in the spacing ratio. For instance, for the case of S/d_e = 1.8, this was x_{asym} = 0.8de, while it increased to x_{asym} = 2.5d_e for S/d_e = 3.7. In Fig. 5-8e, $I^x_{uu\_S}$ is the result of integration of left tale. The results are not shown for S/d_e = 5.5 and 7.3, as their respective correlation plots did not converge to zero within the field of view used in the experiments. Downstream of the region where $I^x_{uu\_S}$ increases initially, there exists a transition region where its values are almost constant. The length of this region also increases as the spacing ratio increases. For instance, in the case of S/d_e = 1.8, this is x_{tran}= 1.0d_e while for S/d_e = 3.7, it increases to x_{tran} = 2.0d_e. Interestingly, the slope of the linear region further downstream is independent of nozzle spacing and equal to $a^x_{uu\_S}$ = 0.048.

Fig. 5-8f shows the results for $I^y_{vv\_S}$, in which the trend is roughly similar to the one observed in Fig. 5-8e. The difference is that the slope in the linear region changes with the spacing ratio. That is $a^y_{vv\_S}$ = 0.010, 0.017, 0.021, 0.023 and 0.023 for S/d_e = 1.8, 2.8, 3.7, 5.5 and 7.3. It is seen that as the spacing ratio increases, the difference between slopes decreases. To summarize, the

slopes of the linear regions are provided in Table 5-2. This table clearly shows that while the spatial growth rate of LSS along the outer shear layer is independent of the spacing ratio, along the symmetry line, the growth rate of LSS along the transverse direction is highly affected by the spacing ratio.

5.2.4. Joint probability density function

Joint probability density function (JPDF) is often used to investigate the most frequent and dominant turbulent motions that contribute to Reynolds shear stress, $<uv>$ at any location in the flow [40]. As the streamwise and transverse fluctuating velocities can be positive or negative, four combinations of signs can be assigned. Each of these combinations is called a quadrant, and is attributed to a unique turbulent motion. For instance, the first quadrant, Q_1 is the region where both u and v are positive. For the outer shear layer $\frac{\partial U}{\partial y} > 0$, and hence Q_1 represents a high speed motion that is directed away from the jet. The opposite holds for the inner shear layer; $\frac{\partial U}{\partial y} < 0$, and hence Q_1 denotes to an inward high speed motion.

Fig. 5-9 shows the contour plots of JPDF for S/d_e = 1.8 and 3.7 at x/d_e = 1.2 and 3.8, which are $0.1d_e$ downstream of the MP location. In Figs. 5-9a and 5-9b, the results are shown in the outer shear layer of the lower jet for S/d_e = 1.8 and 3.7, respectively. In both figures, the contours are inclined towards the Q_1 and Q_3 events, which represent high speed ejection of large-scale fluctuations and low speed entrainment of ambient fluid into jet envelop for the outer shear layer, respectively. This observation is in line with flow visualizations in Figs. 5-2 and 5-3. For S/d_e = 1.8, the most frequent event is Q_3, while for S/d_e = 3.7, Q_1 is the most frequent event. In the inner shear layers (Figs. 5-9c and 5-9d), the contours are inclined towards Q_2 and Q_4 events, which are indication of high speed ejection and low speed entrainment, respectively. The most frequent

events are Q_2 for $S/d_e = 1.8$, and Q_4 for $S/d_e = 3.7$. Along the symmetry line, as the level of Reynolds shear stress is low, the most probable events are the ones with low fluctuating velocities. Also, in

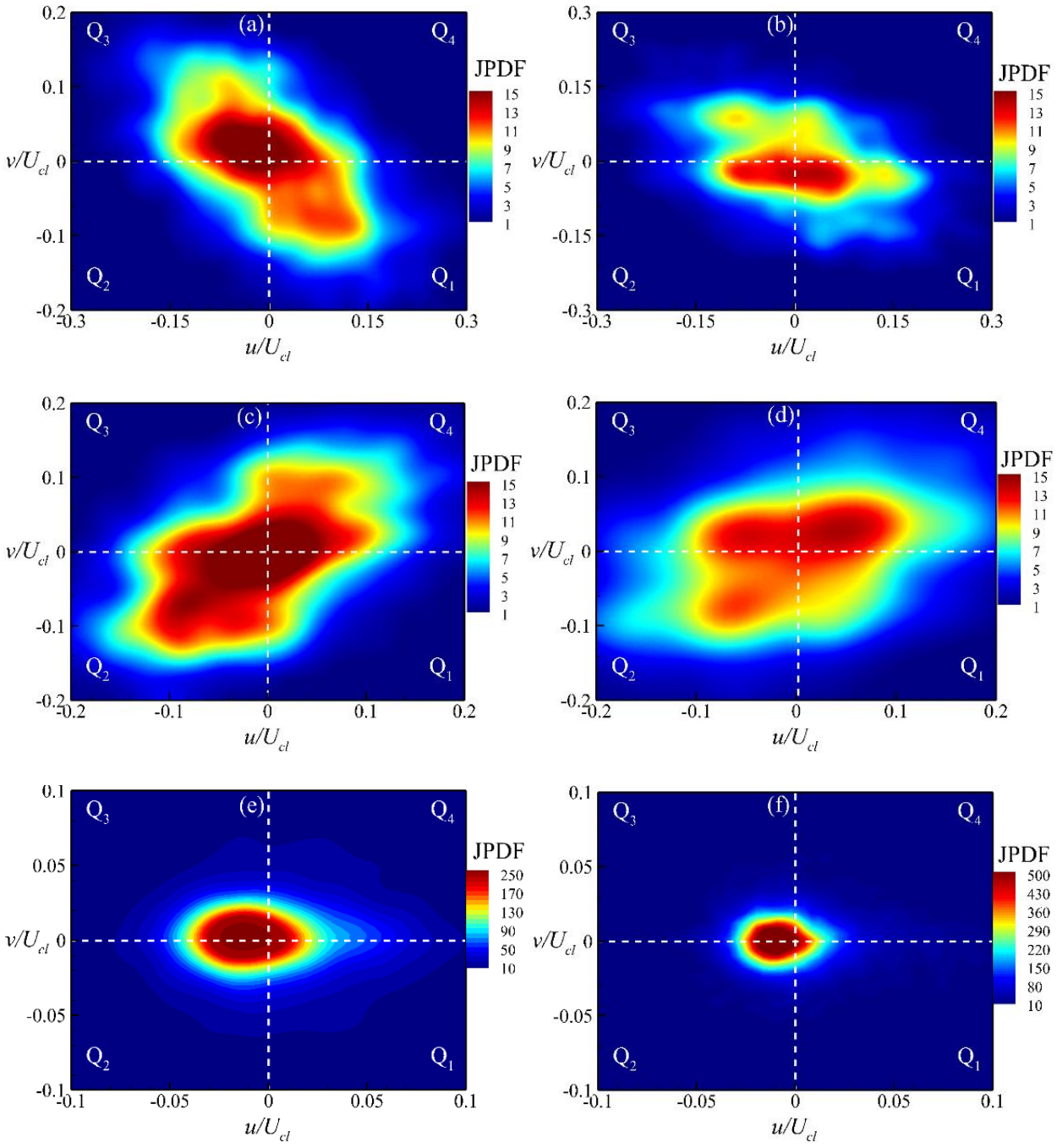

Fig. 5-9. JPDF contours, $0.1d_e$ downstream of the MP location at (a), (b) outer shear layer, (c), (d) inner shear layer and (e), (f) symmetry line for $S/d_e = 1.8$ and 3.7 respectively.

line with the observation of Aleyasin *et al.* [36], the contours are more symmetric which shows that the turbulent field is more isotropic compared to the shear layers. A closer examination of

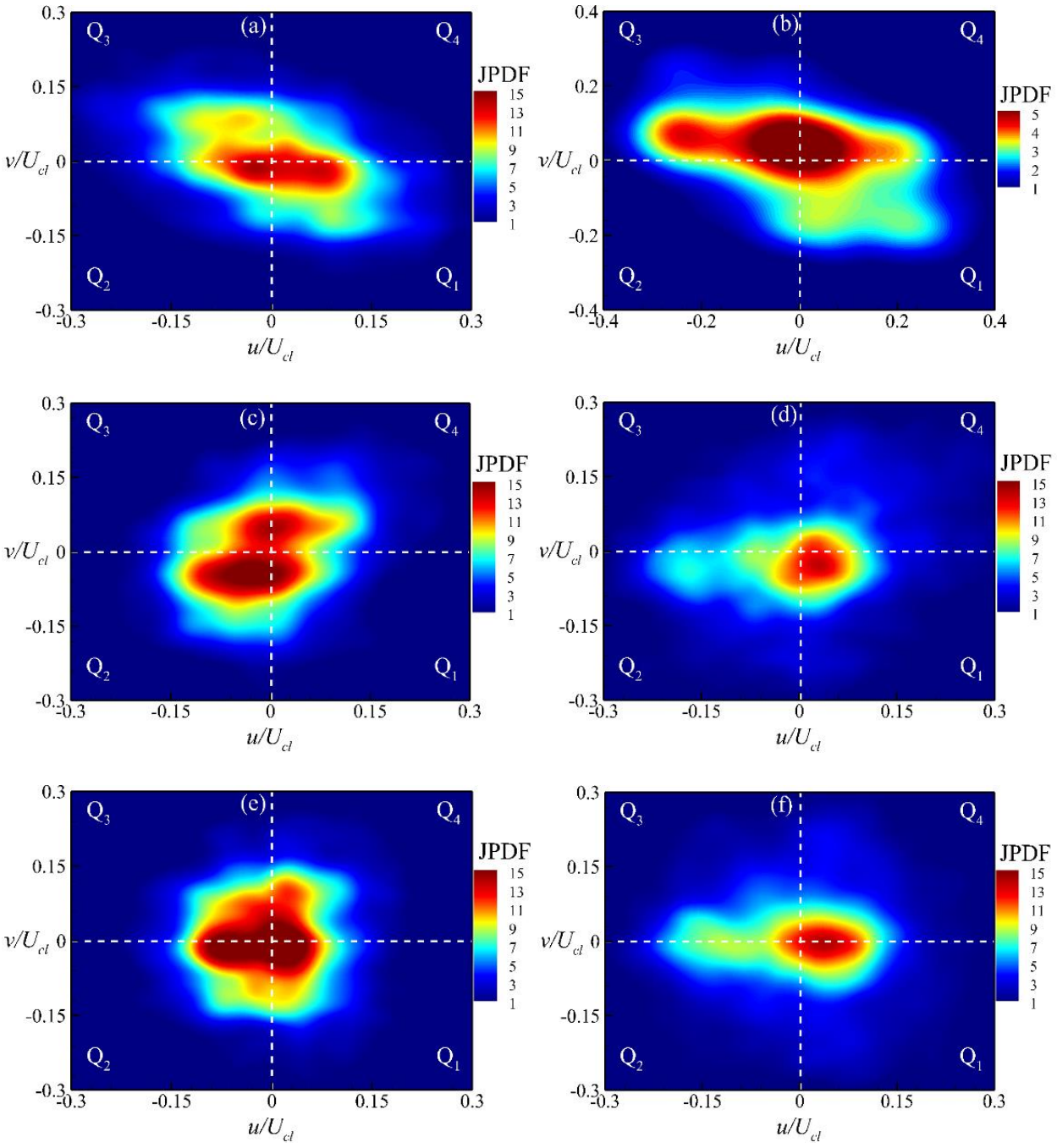

Fig. 5-10. JPDF contours in LISHL at (a), (b) outer shear layer, (c), (d) inner shear layer and (e), (f) symmetry line for S/d_e = 1.8 and 3.7 respectively.

Figs. 5-9e and 5-9f shows that low-speed events are more probable. This can be attributed to early stages of vortex shedding process as the interactions are not as intense yet.

The JPDF results at LISHL are provided in Fig. 5-10, which shows that similar to the previous region, the contours of outer shear layer are oriented towards the Q_1 and Q_3 events. For the case of S/d_e = 1.8, the results are extracted at x/d_e = 2.9 and presented in Fig. 5-10a. This streamwise location is close to x/d_e = 3.8, where the plots for the case of S/d_e = 3.7 were extracted in Fig. 5-9a. Therefore, a similarity can be identified between these two figures. For the case of S/d_e = 3.7, low speed entrainment as represented by the Q_3 events is almost as frequent as high speed sweep motions as represented by the Q_4 events. This suggests that the outer shear layer has entered a region where there is a balance between the entrainment of the ambient fluid and spread of the jet envelop. At LISHL, the transverse location of inner shear layer is close to the symmetry line, which explains the qualitative similarity observed between Figs. 5-10c and 5-10e for the case of S/d_e = 1.8 and Figs. 5-10d and 5-10f for the case of S/d_e = 3.7. The contours in Figs. 5-10c and 5-10e occupy larger extent of the vertical axis compared to Figs. 5-10d and 5-10f. In other words, for S/d_e = 1.8, inward and outward turbulent motions with large transverse velocities are more frequent than in the case of S/d_e = 3.7. Interestingly, in the previous study [38], it was observed that the peak of transverse turbulence intensity downstream of the MP is larger than the streamwise component for S/d_e < 3.7. Therefore, it can be argued that for S/d_e < 3.7 the transverse component of turbulence fluctuations has a major role in the mixing process between the jets. Compared to the preceding region (Fig. 5-9), at LISHL the jets are more involved with interactions and mixing. As a result, the contribution of high-speed events have also become more significant in Figs. 5-10e and 5-10f compared to Figs. 5-9e and 5-9f.

5.2.5. Swirling strength

The imaginary part of the complex eigenvalue of a local velocity gradient tensor is defined as swirling strength [41]. In Planar PIV, the complete velocity gradient tensor is not available. Hence,

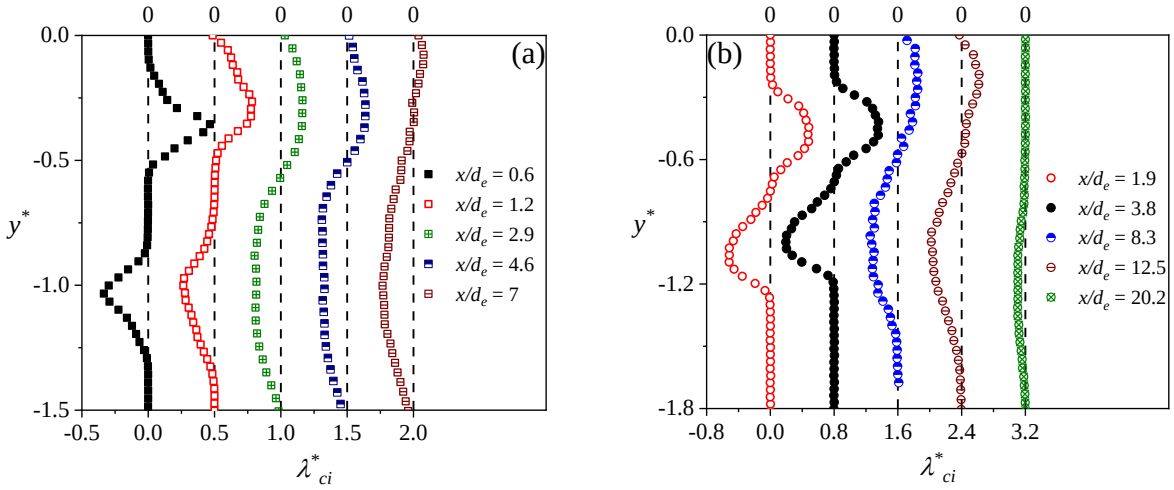

Fig. 5-11. Profiles of swirling strength at different streamwise locations. (a) S/d_e = 1.8 and (b) S/d_e = 3.7.

following [42] and [43], the eigenvalue of the velocity gradient tensor in *x*-*y* plane is determined as follows[42, 43]:

$$\lambda = \frac{1}{2}\left(\frac{\partial U}{\partial x} + \frac{\partial V}{\partial y}\right) \pm \frac{1}{2}\sqrt{\underbrace{\left(\frac{\partial U}{\partial x} + \frac{\partial V}{\partial y}\right)^2}_{b^2} - 4\underbrace{\left(\frac{\partial U}{\partial x}\frac{\partial V}{\partial y} - \frac{\partial V}{\partial x}\frac{\partial U}{\partial y}\right)}_{ac}} \qquad \text{Eqn (5-4)}$$

In order to have a complex solution, $4ac > b^2$. In this case, swirling strength is expressed as:

$$\lambda_{ci} = \frac{1}{2}\sqrt{|b^2 - 4ac|} \qquad \text{Eqn (5-5)}$$

In Eqn (5-5), λ_{ci} is always positive. The sign of instantaneous fluctuating vorticity can then be used to recover the sign of swirling strength. This classifies the vortices into prograde (associated with the negative sign of λ_{ci}) and retrograde (associated with the positive sign of λ_{ci}).

In order to refine our analysis of the strength of the vortices (visualized in Figs. 5-2 and 5-3), the profiles of the one-dimensional swirling strength are presented in Figs. 5-11a and 5-11b for S/d_e = 1.8 and 3.7, respectively. Due to symmetry, the results are only shown for the lower jet. In these figures, the horizontal and vertical axes are respectively $\lambda_{ci}^* = \frac{\lambda_{ci} y_{0.5}^+}{U_m}$ and $y^* = \frac{y}{y_{0.5}^+}$. In order to study the streamwise evolution of swirling strength, the profiles are extracted at 5 streamwise locations corresponding to the middle of the converging region, $0.1d_e$ downstream of MP, LISHL, middle of the merging region, and $1d_e$ upstream of the CP. In the middle of the converging region, negative- and positive-valued peaks exist at the outer and inner shear layers, respectively. As the jets are well within the potential core region, the vortices along the shear layers cannot diffuse into their cores and hence a region with λ_{ci}^* = 0 exists between the two peaks for the case of S/d_e = 1.8. For the case of S/d_e = 3.7, the inner and outer peaks are comparable, however, for the case of S/d_e = 1.8, the inner peak is 40% higher than the outer one. This shows that at smaller spacing ratio the staggered pattern of counter-rotating structures increases the shear and hence the swirling strength of individual vortices along the inner shear layers. As the spacing ratio increases, the jets develop more freely in the converging region and hence they show a more similar behavior along their shear layers.

At the second streamwise location ($0.1d_e$ downstream of MP), the inner peak for S/d_e = 1.8 is still larger than the outer peak. This was expected, as compared to prograde vortices, the swirling strength for retrograde vortices were higher in the preceding region. By comparing the positive and negative peaks, the effects of interactions can be observed. For the case of S/d_e = 1.8, although the inner shear layer peak is still larger than the outer counterpart, the difference is now only 17%. For the case of S/d_e = 3.7, the inner peak is 8% lower. In comparison to the outer shear layer, the inner shear layer is exposed to shedding of vortices with opposite sign from the adjacent jet. As a

result, the mean swirling strength of retrograde vortices decreases and eventually becomes smaller than prograde vortices. The retrograde vortices continue to decay faster than their prograde counterparts. As a result, at LISHL (third streamwise location), the peaks of retrograde vortices are 20% and 29% lower than the prograde ones for $S/d_e = 1.8$ and 3.7, respectively. In the preceding locations, the transverse extent of positive and negative swirling strength were comparable. However, it is seen that the jet's cross-section is more occupied by prograde vortices. These trends continue to progress as the jets develop in the merging region. As a result, in the middle of the merging region (forth streamwise location), compared to prograde vortices, retrograde vortices show 30% and 48% lower peak value for $S/d_e = 1.8$ and 3.7 respectively. At last streamwise location, there is almost no sign of retrograde vortices. This is more evident in the case of $S/d_e = 3.7$ where for $0 < y^* < 0.8$, swirling strength is zero. Also, in the profile of $S/d_e = 1.8$, the transverse region occupied by prograde vortices is 7 times larger than the one for retrograde vortices. This clearly shows the continuous progress of prograde vortices across the jet as retrograde ones weaken.

5.2.6.Turbulent/non-turbulent interface

The interface between the turbulence part of the flow and the ambient fluid is referred to as the turbulent/non-turbulent interface (TNTI) of a jet. Once the TNTI of a jet is determined, it becomes possible to track the spatial development of jet envelope. This also facilitates the study of shear layers in the presence of an adjacent jet. To identify the interface, various techniques have been used in the past. The adopted parameter for the criterion makes one technique different than the other. For instance, in vorticity criterion, the threshold distinguishing the turbulence from the non-turbulence region is set based on the magnitude of the total vorticity vector [44, 45]. Other techniques take advantage of concentration and instantaneous streamwise velocity [46–48].

Following Khashehchi *et al.* [48] and Ghasemi *et al.* [49] in this study, the velocity criterion, shown in Eqn (5-6), was adopted in order to locate the TNTI.

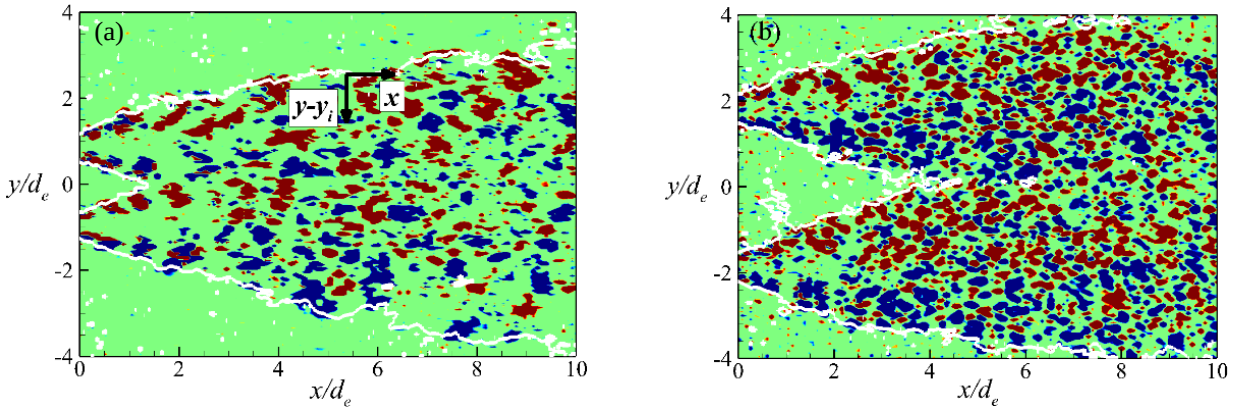

Fig. 5-12. Instantaneous location of TNTI for (a) S/d_e = 1.8 and (b) S/d_e = 3.7.

$$\begin{cases} \dfrac{U_{ins}}{U_{exit}} \geq 0.03 & \text{Flow in turbulent region} \\ \dfrac{U_{ins}}{U_{exit}} < 0.03 & \text{Otherwise} \end{cases} \qquad \text{Eqn (5-6)}$$

For each snapshot, the values of $\frac{U_{ins}}{U_{exit}}$ was calculated for the whole field of view. The flow field was then swept vertically in order to find the transverse location of the TNTI. Consequently, the conditionally-averaged quantities across the interface were calculated by averaging the data from all the snapshots.

Fig. 5-12 shows the instantaneous TNTI location using the above criterion. To validate, the instantaneous contours of swirling strength are also provided. As it is clear, the interface compasses almost all of the vortical structures within the jets. In other words, the velocity criterion was able to successfully locate the transverse extent of the jets' shear layers. As a result, on turbulent side of the interface the instantaneous vorticity is non-zero, while an irrotational ambient

fluid exists on the other side of the interface. The new coordinate system is also provided in Fig. 5-12, which is used in the upcoming figures.

To further investigate the mean flow physics around the TNTI, the conditionally-averaged profiles of mean streamwise velocity are provided in the following figures. The profiles are extracted at two streamwise locations of x/d_e = 2.5 and 8.0. For some spacing ratios these locations lie within the converging region while for the others they are in the merging region. In this fashion, the effects of interactions on the mean flow around the TNTI can be investigated. As similar streamwise locations were selected by Aleyasin *et al.* [36], the conditionally-averaged profiles in the present study can also be compared with the ones for twin round jets.

Figs. 5-13a and 5-13b show the conditionally-averaged mean streamwise velocity profiles at x/d_e = 2.5 for the outer and inner shear layers respectively. In line with previous observations, the profiles of the outer shear layer, Fig. 5-13a, show no effects of the spacing ratio and fairly collapse on top of each other. For $0 < \frac{y-y_i}{d_e} < 0.3$, the values of $\frac{U}{U_{cl}}$ are larger for the present study compared to the study of Aleyasin *et al.* [36]. In other words, in the vicinity of the TNTI, $\frac{\partial U}{\partial y}$ is larger for twin rectangular jets compared to the round counterpart. It is due to this larger shear that the asymmetric jets spread faster than the symmetric ones in the near-field region. The unconditional-averaged profile of S/d_e = 7.3 is also provided in Fig. 5-13a for comparison. By moving across the interface from the non-turbulent to the turbulent side, the unconditional-averaged profile gradually increases from $\frac{U}{U_{cl}}$ = 0.0 to $\frac{U}{U_{cl}}$ = 0.08, while for the conditionally-averaged case, the profile is zero in the non-turbulent side and upon entering the turbulent region it jumps to $\frac{U}{U_{cl}}$ = 0.07. In Fig. 5-13b the profiles are extracted across the inner shear layer. The profile of S/d_e = 1.8 is not shown since no

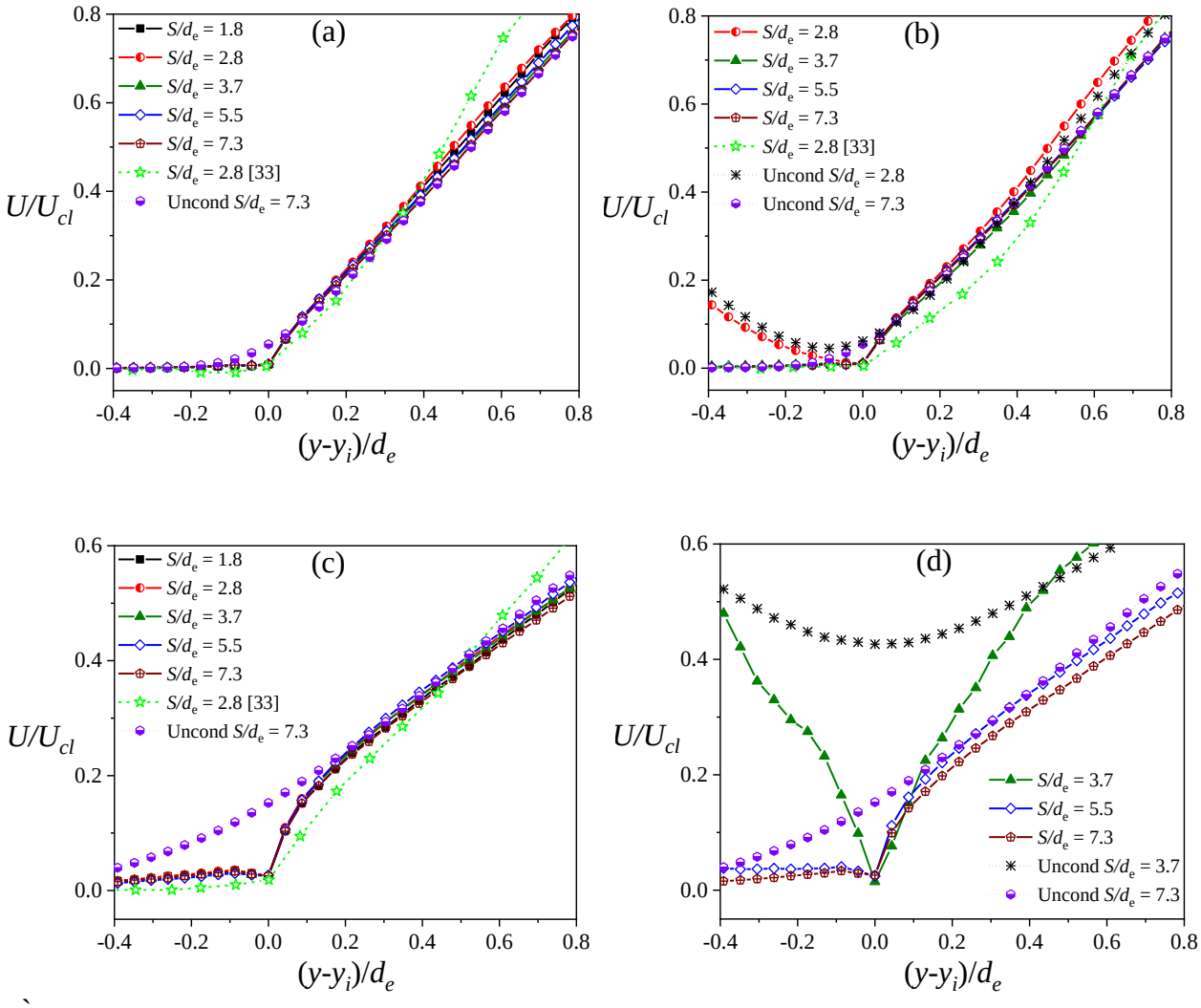

Fig. 5-13. Conditionally-averaged mean streamwise velocity profiles. (a) Outer and (b) inner shear layers at x/d_e = 2.5. (c) Outer and (d) inner shear layers at x/d_e = 8.0.

inner shear layer existed at x/d_e = 2.5 due to interaction between the two inner shear layers. For S/d_e = 3.7, 5.5 and 7.3, the profiles collapse as their inner shear layers are still in the converging region. For S/d_e = 2.8, the inner shear layer is in the merging region (MP for S/d_e = 2.8 is at x/d_e = 2.3) and hence the corresponding profile shows a deviation for $\frac{y-y_i}{d_e} > 0.3$. Interestingly, for $0 < \frac{y-y_i}{d_e} < 0.3$, no deviation can be observed which implies that $\frac{\partial U}{\partial y}$ close to the interface is independent of spacing ratios. This is interesting because the case of S/d_e = 2.8 is in the early merging region

while the others are still in the converging region. Applying similar analogy to the outer shear layer, the transverse spread of the inner shear layers at this point is expected to be independent of the spacing ratio. This indeed is the case, as in the previous study [38] the half-velocity width of the inner shear layers at x/d_e = 2.5 was identical for S/d_e = 2.8, 3.7, 5.5 and 7.3. The inner shear layer profile of Aleyasin *et al.* [36] shows more suppression than its outer shear layer counterpart. As a result, the deviation from the results of present study becomes larger and transverse domain of the difference increases to $0 < \frac{y-y_i}{d_e} < 0.6$. Regarding the jump, similar behavior to the one in Fig. 5-13a can be observed here as well.

At x/d_e = 8.0, Fig. 5-13c, the outer shear layer profiles still fall on top of each other. Compared to the preceding location, the difference between conditional and unconditional profiles in the vicinity of the interface becomes more pronounced and hence, the jump in the conditional profiles is clearer. Similar observations can be made from Fig. 5-13d for S/d_e = 5.5 and 7.3. While the conditional profiles of S/d_e = 2.8 in Fig. 5-13b and S/d_e = 3.7 in Fig. 5-13d are extracted in the merging region, the latter shows more dramatic difference with its unconditional pair. The reason is that at x/d_e = 2.5 the case of S/d_e = 2.8 is only $0.2d_e$ into the merging region while at x/d_e = 8.0, this is more than $4d_e$ for the case of S/d_e = 3.7. In other words, such an increasing difference between the unconditional and conditional profiles is the outcome of progressive interactions in the merging region.

5.3. Conclusion

A PIV study is performed to understand the physical phenomenon of momentum interference of twin jets. The effects of jet separation on the spatial development of large-scale structures (LSS) and interaction of shear layers of the twin jets are investigated. To provide insights into the complex flow physics of twin jet interaction, both qualitative and quantitative tools are applied in

our analysis. Flow visualizations based on Galilean decomposition and swirling strength are used for qualitative characterization of the momentum interference of the twin jets. The results clearly show the shedding of vortices between the jets in the merging region, which facilitates momentum mixing and interaction. Also in this region, two-point auto-correlation functions of transverse velocity fluctuations show identical behavior for the inner and outer shear layers. This however, is not the case for the auto-correlation functions of streamwise velocity fluctuations and the cross-correlation functions of streamwise and transverse velocity fluctuations along the inner shear layer. For the case of cross-correlation streamwise and transverse velocity fluctuations, the effects of interactions are not only on the spatial length of correlation but also on its maximum. This results in a 44% lower peak for the cross-correlation profile of the inner shear layer compared to the outer shear layer.

To further study the LSS, integral length scale is evaluated at several streamwise locations. Along the outer shear layer, no effect of nozzle spacing is observed. Along the symmetry line, however, the rate at which the integral length scale increases with the streamwise distance is shown to be affected by the spacing ratio. For instance, this rate for the case of $S/d_e = 5.5$ is 56% lower than observed for the case of $S/d_e = 1.8$. The effects of spacing ratio are also observed on the frequency of events along the symmetry line. For cases of $S/d_e < 3.7$, events involved with high/low transverse fluctuations are amongst the most frequent ones. It is therefore understood that for small spacing ratios, transverse velocity fluctuations are more actively involved in turbulence transport mechanism between the interacting jets. The interactions are also shown to highly affect the strength of vortices along the inner shear layer. For instance, for the case of $S/d_e = 3.7$, at $4.6d_e$ downstream of the MP location, retrograde vortices show 29% lower peak value compared to prograde ones.

To refine the study of shear layers, the turbulent/non-turbulent interface (TNTI) along the inner and outer shear layers is investigated. Thus far, studies of TNTI have been majorly restricted to a single jet. The present investigation of TNTI of twin jets reveals many new and interesting physical features. To carry out the analysis, conditionally-averaged mean streamwise velocity profiles around the interface are obtained. At any of the streamwise locations, the profiles of the outer shear layer show no effect of the spacing. This is also the case for the inner shear layer profiles of the jets when they are in the converging region. Upon entering the merging region, the profiles of the inner shear layer tend to deviate. By developing into this region the deviation becomes more pronounced. By definition, $\frac{U}{U_{cl}} = 0$ at the interface in the conditional profiles while it obtains a non-zero value for unconditional profiles. It is observed that by increasing the streamwise distance, the difference between these two types of profiles at the interface increases. In other words, the jump in the conditional profiles at the interface increases with streamwise distance for $2.5 < x/d_e < 8.0$.

Chapter 6

Conclusions and future work

6.1. Summary and conclusions

Effects of spacing ratio on the mean flow, turbulence intensities and Reynolds shear stress of rectangular twin jets were experimentally investigated. The spacing between the nozzles were set to S/d_e = 1.8, 2.7, 3.7, 5.5 and 7.3 and Reynolds number was fixed at Re_{de} = 10,000 for all of the test cases. The results showed that the locations of the merging and the combined points increase linearly with increasing spacing ratio. The combined point, however, was more affected by the change in the spacing ratio as the slope of its fitted line was more than 3.5 times of the one for the merging point location. Also, the twin rectangular jets examined in the present study showed earlier merging and combined points compared to twin round jets.

The spread rate of the outer shear layer as well as the decay of local maximum velocity decreased in the combined region. The former however recovered further downstream while the latter kept its 60% lower decay rate compared to its preceding regions. Hence, in terms of mixing characteristics of the jets, it can be concluded that smaller spacing ratios result in a faster mixing within the jets while larger spacing ratios provide a faster mixing between individual jets and the ambient. In comparison, in converging and merging regions, the spread rate of the outer shear layer in the present study was similar to the one for a single jet. The decay rate on the other hand, was 16% higher.

Along the symmetry line, the streamwise mean velocity as well as turbulence intensities showed an abrupt increase towards a maximum in the immediate vicinity of the merging point location. By increasing the spacing ratio, the slope of the jump as well as the peak value were

decreased. This resulted in 77%, 44% and 65% difference between the peaks of S/d_e = 1.8 and 7.3 for $\frac{U_{sym}}{U_{max}}$, $\frac{u_{rms\_s}}{U_{max}}$ and $\frac{v_{rms\_s}}{U_{max}}$ respectively.

For $S/d_e \leq 3.7$, the transverse turbulence intensity along the symmetry line showed higher peak values compared to its streamwise counterpart while the opposite was observed for $S/d_e > 3.7$. The contour plots of Reynolds shear stress showed that as the spacing ratio between the nozzles increases, the inner shear layer is less suppressed by the converging adjacent shear layer and hence, more symmetry in the spatial development of Reynolds shear stress between the inner and the outer shear layers can be observed. The one-dimensional profiles suggested that by increasing the spacing ratio between the nozzles, the distance between the CP and the location where turbulence intensities and Reynolds shear stress obtain self-similarity, decreases.

The LSS were visualized through Galilean decomposition and swirling strength. The plots clearly showed the shedding process of the counter-rotating vortical structures. Within each jet, this was done downstream of the potential core region, while between the two jets, this was expectedly observed downstream of the MP location. For smaller spacing ratios of $S/d_e < 3.7$, the shedding resulted in a formation of counter-rotating structures across the symmetry line, similar to von Karman vortex street.

The auto and cross correlation plots were provided to give an insight regarding the relative size of LSS along the outer and inner shear layers. This was of interest as it was expected that the interactions in the merging region, would result in deviation between the plots. In fact, this was the case for the auto correlation of streamwise velocity fluctuations and the cross correlation between the streamwise and transverse components. To be specific, at last inner shear layer location, the spatial auto and cross correlations for the outer shear layer were delayed by $1.5d_e$ and

0.6d_e respectively, compared to the inner shear layer. Interestingly, these differences were the same for the cases of S/d_e = 1.8 and 3.7, which indicates that the observation is independent of the spacing ratio.

Following the correlation of velocity fluctuations, the integral length scale of turbulence was evaluated along the shear layers and the symmetry line in order to investigate the effects of interactions on the size of LSS. In line with findings on two-point correlation, the llongitudinal integral length scale of the inner shear layer started to decay as the jets entered the merging region. Along the symmetry line, both the longitudinal and transverse integral length scales showed three distinct regions in their downstream developments. This consisted of an initial region, a transition region where the scales kept an almost constant value, and finally, a linear region. As the name suggests, in the linear region, the integral length scales linearly increased with downstream distance. For the longitudinal component, the slope was independent of the spacing ratio and equal to 0.048, however, for the transverse component, a direct relation was observed. Such relation resulted in more than 50% increase in the slope of the linear region when the spacing ratio increased from S/d_e = 1.8 to S/d_e = 5.5.

The probability of events that contribute to the production of Reynolds shear stress was shown via joint probability density contours. Expectedly, along the shear layers, the high-speed ejections and low-speed entrainments were the dominant events. At LISHL, the probability contours of the inner shear layer highly resembled the ones for the symmetry line. This proved the contribution of dominant events along the inner shear layers on facilitating the interactions along the symmetry line. Also at this streamwise location, low speed events were noticeably higher for the case of S/d_e = 1.8 compared to S/d_e = 3.7. In another comparison along the symmetry line, inward/outward

motions showed higher probability for the case of S/d_e = 1.8. This was denoted to more intense interactions for smaller spacing ratios.

The decay of vortical structures along the inner shear layer was clearly shown by the profiles of swirling strength at 5 streamwise locations. These locations were covering the converging region down to $1d_e$ upstream of the CP. As the profiles progressed downstream, the swirling strength of the retrograde vortices, located along the inner shear layer, reduced. This continued to the point where at last extraction location, swirling strength was zero. Meanwhile, the transverse length where the retrograde vortices were active, was also reduced. This was accompanied by noticeable progress of prograde vortices across the jet.

The final touch was on the turbulent/non-turbulent interface (TNTI). The instantaneous contour lines of $\frac{U_{ins}}{U_{exit}}$ = 0.03 enclosed the almost all of the retrograde and prograde instantaneous vortices along the outer and inner shear layers. In other words, the velocity criteria was able to successfully detect the interface between turbulent jet and the non-turbulent ambient fluid. Irrespective of the spacing ratio, the conditionally-averaged velocity profiles of the outer shear layer collapsed on top of each other even in the near-field region at x/d_e = 2.5. The profiles of the inner shear layer however were shown to be manipulated by the interactions in the merging region. In that sense, the difference between $\frac{U}{U_{cl}}$ values of conditional and unconditional profiles at the interface increased by moving further into the merging region. For instance, for S/d_e = 2.8 at x/d_e = 2.5, which is only $0.4d_e$ downstream of its MP, the difference was as low as $\frac{\Delta U}{U_{cl}}$ = 0.06, while for S/d_e = 3.7 at x/d_e = 8.0, which is $4.3d_e$ downstream of its MP, the difference increases to $\frac{\Delta U}{U_{cl}}$ = 0.43.

6.2. Future work

The present research provided thorough discussion regarding the mean flow, turbulence statistics and large-scale structures in twin rectangular jets. This study had a contribution in addressing several aspects of the flow physics, specifically the interactions in the merging region. However, due to complexity of the flow by default, there are still interesting analyses that can be done for the future. Some recommendations are as follow:

- The present research investigated the flow field in minor plane of the rectangular jets. Future experimental studies can focus on the major plane as well as cross-sections of the jets normal to the flow direction. To achieve this, stereo-PIV or tomographic PIV can be used. Such study can provide information regarding the deformation of vortex rings and total entrainment into the jet envelop.
- The present study provided information regarding the convection of the mean flow in streamwise and transverse directions. As a recommendation for future, the energy budgets of turbulence can be studied, especially in the merging region. The results can provide interesting information regarding the turbulent momentum transfer between the jets and the mechanisms responsible for it.
- The present research investigated the large-scale structures using various techniques. Due to the limitations of the PIV setup however, the temporal evolution of LSS could not be studied. For future, time-resolved PIV can be used in order to discuss the temporal correlation of LSS. The formation frequency of LSS can also be evaluated and compared with previous studies on single and twin jets.

Appendix A

Convergence test

The convergence test results regarding of the streamwise mean velocity, streamwise and transverse turbulence intensities and Reynolds shear stress for $S/d_e = 3.7$ are provided in Fig. A-1. As is evident from this figure, the selected total number of 7,500 pair of images were adequate enough to make the results independent of the sample size. Similar observation was deduced from the results of other spacing ratios.

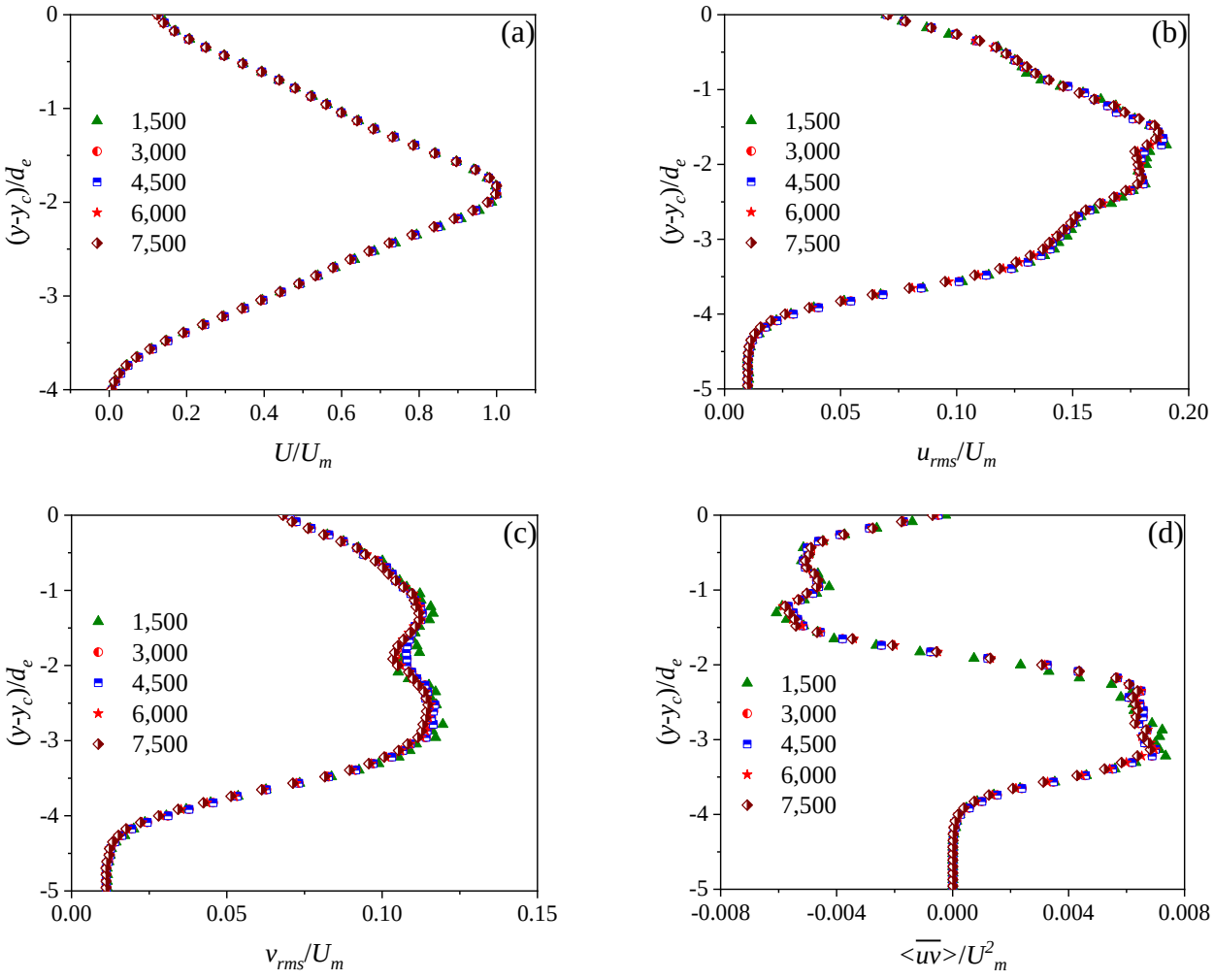

Fig. A-1. Convergence test results of (a) streamwise mean velocity, (b) streamwise turbulence intensity, (c) transverse turbulence intensity and (d) Reynolds shear stress for $S/d_e = 3.7$.

Spatial resolution test

As shown in Fig. A-2, the comparison between these two spatial resolutions shows that IA = 32 × 32 underestimates the results of streamwise mean velocity, streamwise and transverse turbulence intensities and Reynolds shear stress, by 3%, 6%, 6% and 7% respectively. This difference can be attributed to high existing shear between the mean flow and the ambient in the near-field region.

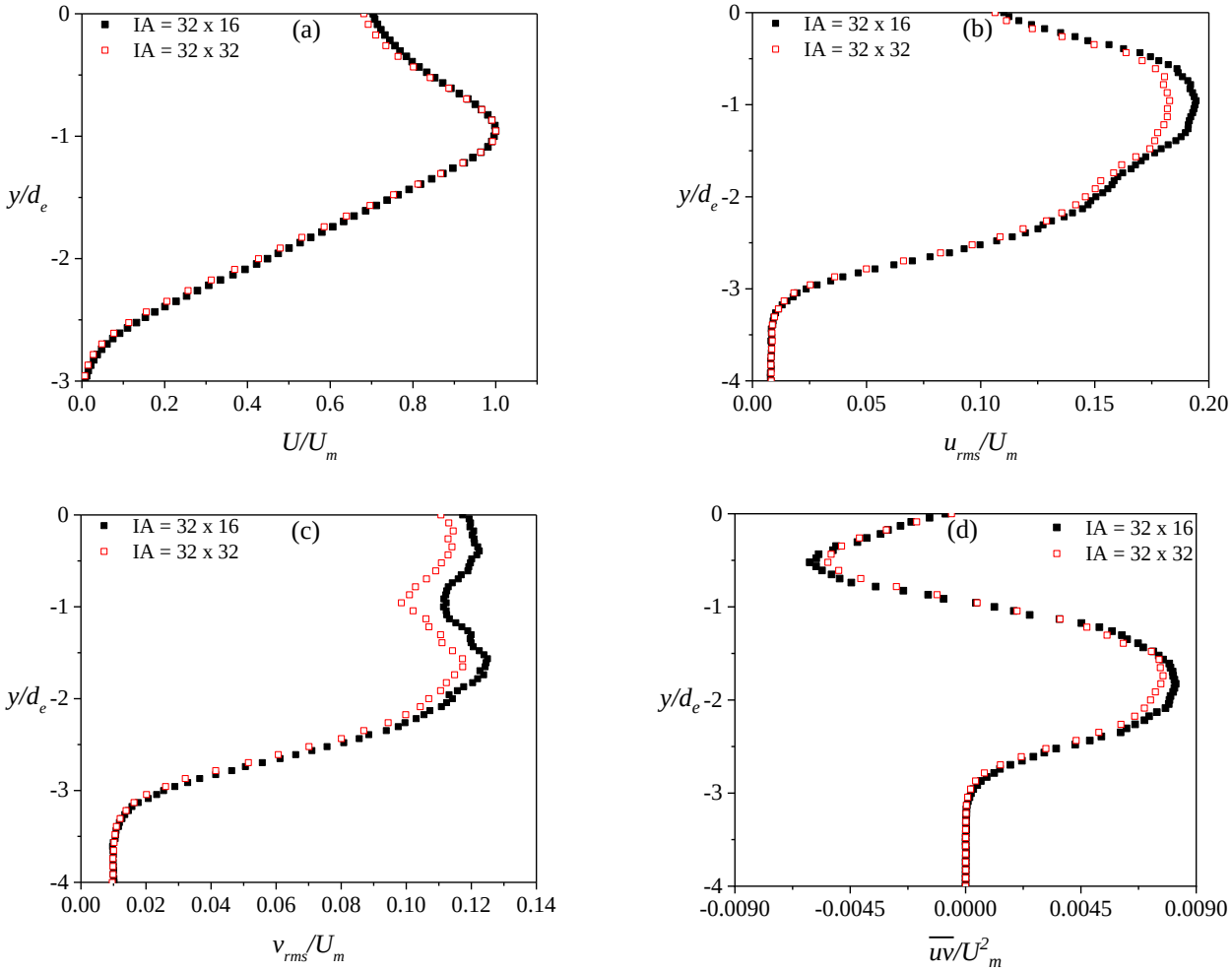

Fig. A-2. Spatial resolution test results of S/de = 1.8 at x/de = 5.0 for (a) streamwise mean velocity, (b) streamwise turbulence intensity, (c) transverse turbulence intensity and (d) Reynolds shear stress.

A similar comparison at $x/d_e = 9.0$ (end of the first measurement plane) which is shown in Fig. A-3, however, reveals that the results are now in good agreement. Hence, the spatial resolution of 32 × 16 was only applied for the first measurement plane.

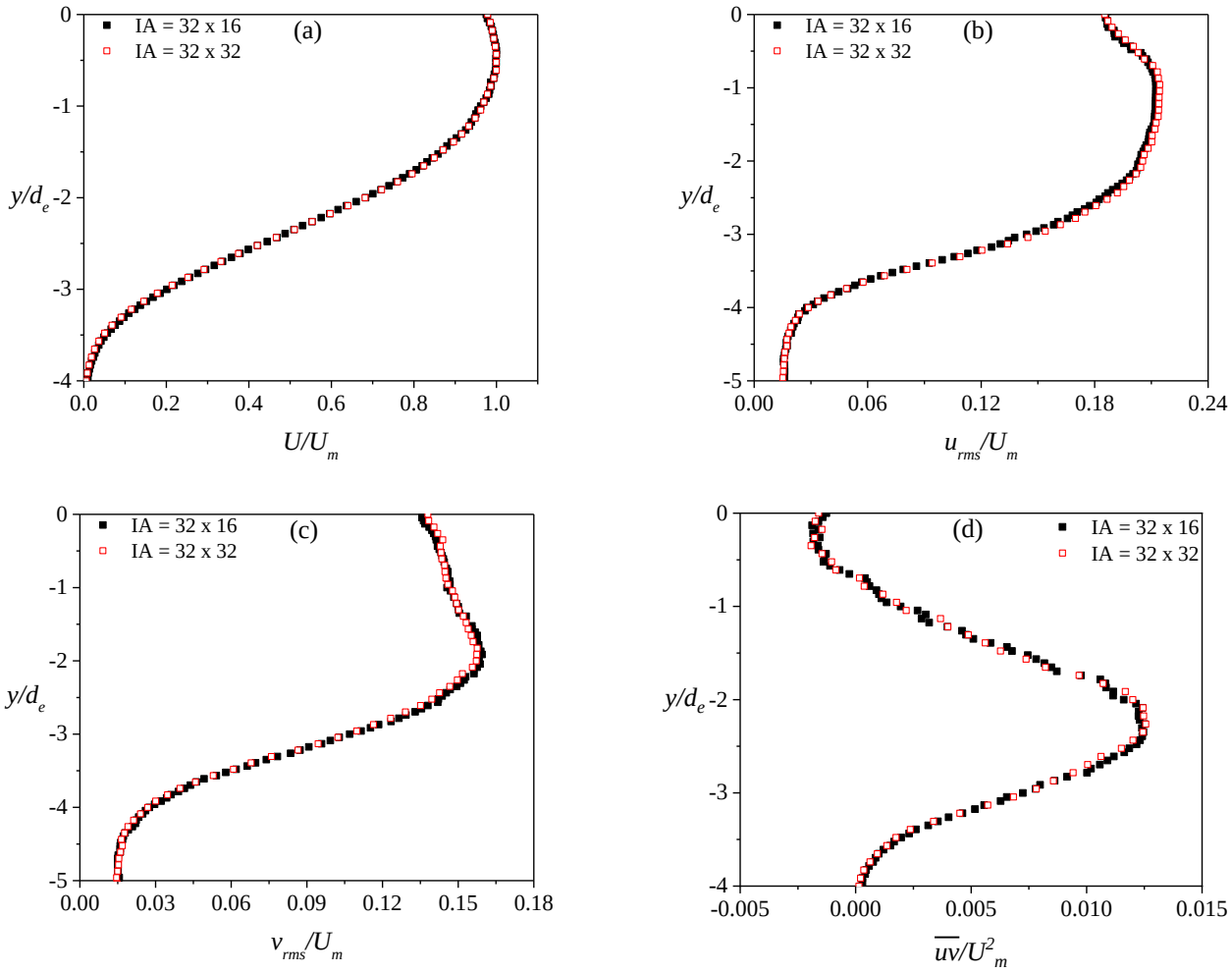

Fig. A-3. Spatial resolution test results of $S/d_e = 1.8$ at $x/d_e = 9.0$ for (a) streamwise mean velocity, (b) streamwise turbulence intensity, (c) transverse turbulence intensity and (d) Reynolds shear stress.

Appendix B

Uncertainty estimates

B.1. Biased error

In PIV, the instantaneous velocity at any point is obtained from the average fluid velocity for an IA and described in Eqn (B-1).

$$U_i = \frac{\Delta S \times L_0}{\Delta T \times L_i} \qquad \text{Eqn (B-1)}$$

In here, ΔS is particle displacement, ΔT is the time between laser pulses, L_0 is the length of the camera view in the plane object, and L_i is the width of the digital image. The bias limit of the velocity is then obtained by Eqn (B-2).

$$B_{U_i}^2 = \theta_{L_0}^2 B_{L_0}^2 + \theta_{L_i}^2 B_{L_i}^2 + \theta_{\Delta S}^2 B_{\Delta S}^2 + \theta_{\Delta T}^2 B_{\Delta T}^2 \qquad \text{Eqn (B-2)}$$

The sensitivity coefficients are defined as $\theta_X = \frac{\partial U_i}{\partial X}$, where $X = \Delta S$, ΔT, L_0 and L_i. The values of these parameters for S/d_e = 1.8 are quantified in Table B-1 for streamwise mean, U, and transverse, V, velocities. Values for B_{L_i}, $B_{\Delta S}$ and $B_{\Delta T}$ are provided from the manufacturer's specification while B_{L_0} was obtained during the calibration process.

Table 0-1. Values of biased error for streamwise and transverse mean velocities.

	Streamwise mean velocity				Transverse mean velocity			
Variable	Value	B_X	θ_X	$\theta_X^2 B_X^2$	Value	B_X	θ_X	$\theta_X^2 B_X^2$
L_0 (m)	1.00E-1	5.00E-4	1.10E+2	3.03E-3	1.00E-1	5.00E-4	1.60E+1	6.40E-5
L_i (pxl)	2.05E+3	5.00E-1	-5.4E-3	7.29E-6	2.05E+3	5.00E-1	-7.83E-4	1.53E-7
ΔS (pxl)	5.3E+0	1.27E-2	2.08E+0	6.98E-4	7.73E-1	1.27E-2	2.08E+0	6.98E-4
ΔT (s)	2.35E-5	1.00E-7	-4.68E+5	2.19E-3	2.35E-5	1.00E-7	-6.83E+4	4.66E-5
U_i (m/s)	1.65E+1	-	-	-	1.89	-	-	-
	Bias error ($\sqrt{\sum \theta_X^2 B_X^2}$)			7.70E-2	Bias error ($\sqrt{\sum \theta_X^2 B_X^2}$)			2.84E-2
	Bias error in % of U			0.47	Bias error in % of U			0.17

B.2. Precision error

The precision errors of streamwise mean, U, and transverse, V, velocities as well as turbulence intensities, (u_{rms} and v_{rms}), and Reynolds shear stress, $\overline{uv}$, are provided in Eqn (B-3), Eqn (B-4), Eqn (B-5) and Eqn (B-6) respectively [50].

$$\varepsilon_U = \frac{Z_c u_{rms}}{\sqrt{N} U} \qquad \text{Eqn (B-3)}$$

$$\varepsilon_V = \frac{Z_c v_{rms}}{\sqrt{N}|V|} \qquad \text{Eqn (B-4)}$$

$$\varepsilon_{u_{rms}} = \varepsilon_{v_{rms}} = \frac{Z_c}{\sqrt{2N}} \qquad \text{Eqn (B-5)}$$

$$\varepsilon_{<uv>} = \frac{Z_c}{\sqrt{N}} \qquad \text{Eqn (B-6)}$$

In here, Z_c is the confidence coefficient which is equal to 1.96 for a 95% confidence level and N is the sample size. Hence, based on the above equations, ε_U = 0.5%, ε_V = 3.0% $\varepsilon_{u_{rms}} = \varepsilon_{v_{rms}}$ = 1.6% and $\varepsilon_{\overline{uv}}$ = 2.3%, for the peak values of respectively the streamwise mean and transverse velocities, turbulence intensities and Reynolds shear stress.

B.3. Total error

The total uncertainty is given by the root-sum-square (RSS) of the bias and precision errors and is indicated in Eqn (B-7).

$$E = \sqrt{B_{u_i}^2 + \varepsilon_{u_i}^2} \qquad \text{Eqn (B-7)}$$

Hence, the measurement uncertainty at 95% confidence level for streamwise mean and transverse velocities are 0.7% and 3% respectively. Also, for turbulence intensities and Reynolds shear stress the measurement uncertainties are 1.6% and 2.3% respectively.

Appendix C

C.1. Two-point correlation results for S/d_e = 2.8, 5.5 and 7.3

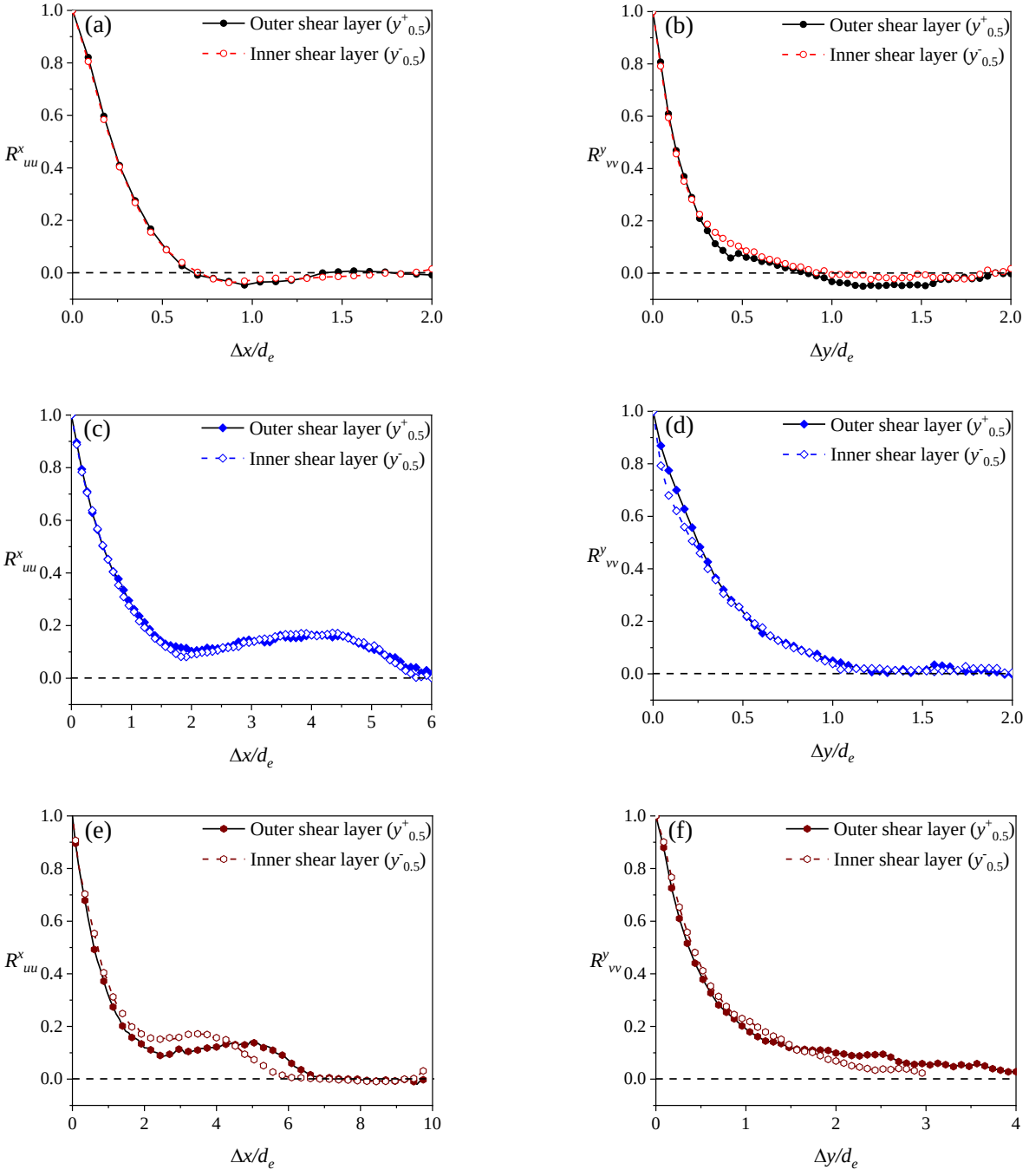

Fig. C-1. Profiles of $R^x_{uu}$and R^y_{vv} at 0.1MP location for (a) and (b), S/d_e = 2.8, (c) and (d), S/d_e = 5.5, and (e) and (f), S/d_e = 7.3.

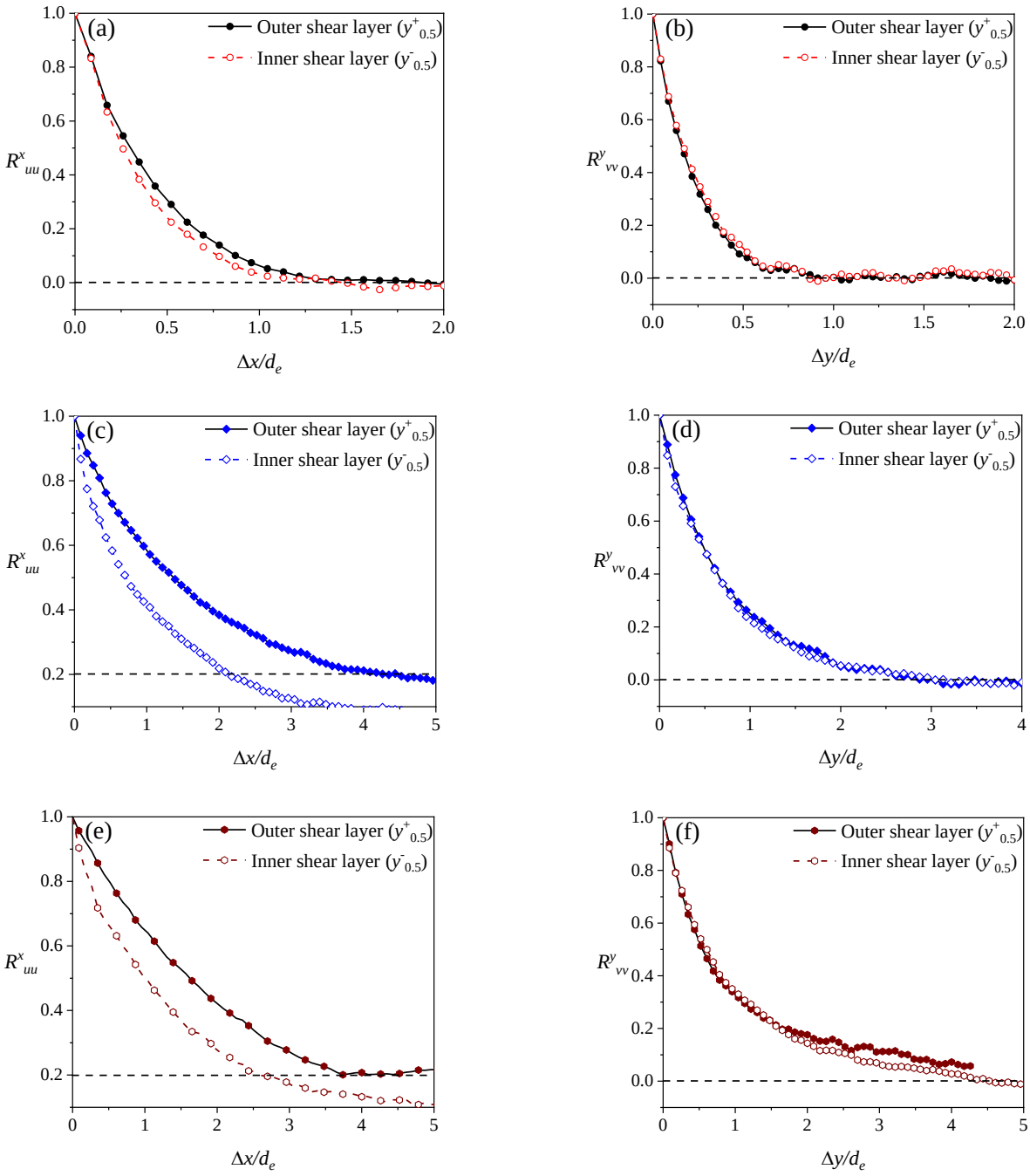

Fig. C-2. Profiles of R^x_{uu} and R^y_{vv} at LISHL for (a) and (b), S/d_e = 2.8, (c) and (d), S/d_e = 5.5, and (e) and (f), S/d_e = 7.3.

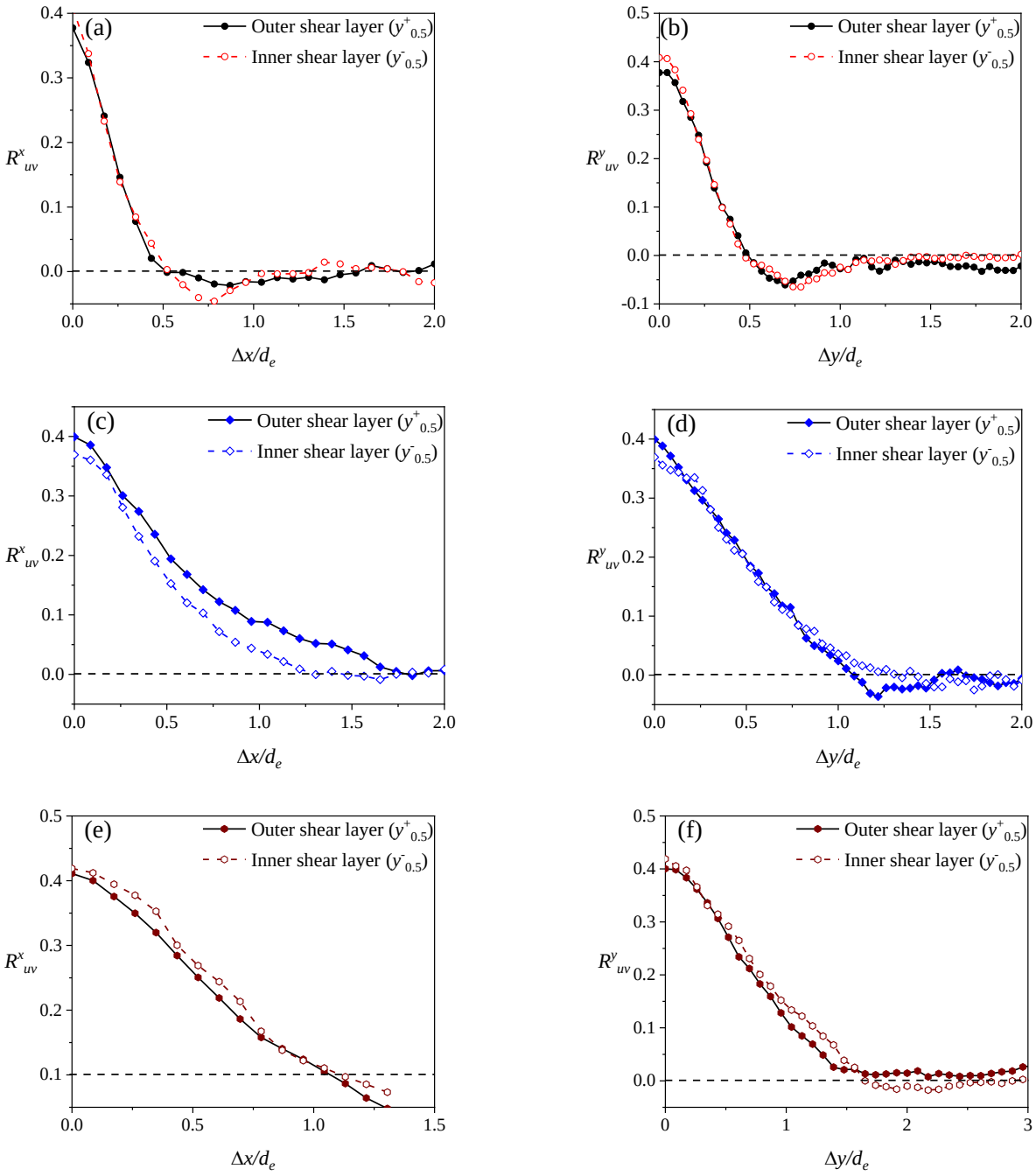

Fig. C-3. Profiles of $R^x_{uv}$and R^y_{uv} at 0.1MP location for (a) and (b), S/d_e = 2.8, (c) and (d), S/d_e = 5.5, and (e) and (f), S/d_e = 7.3.

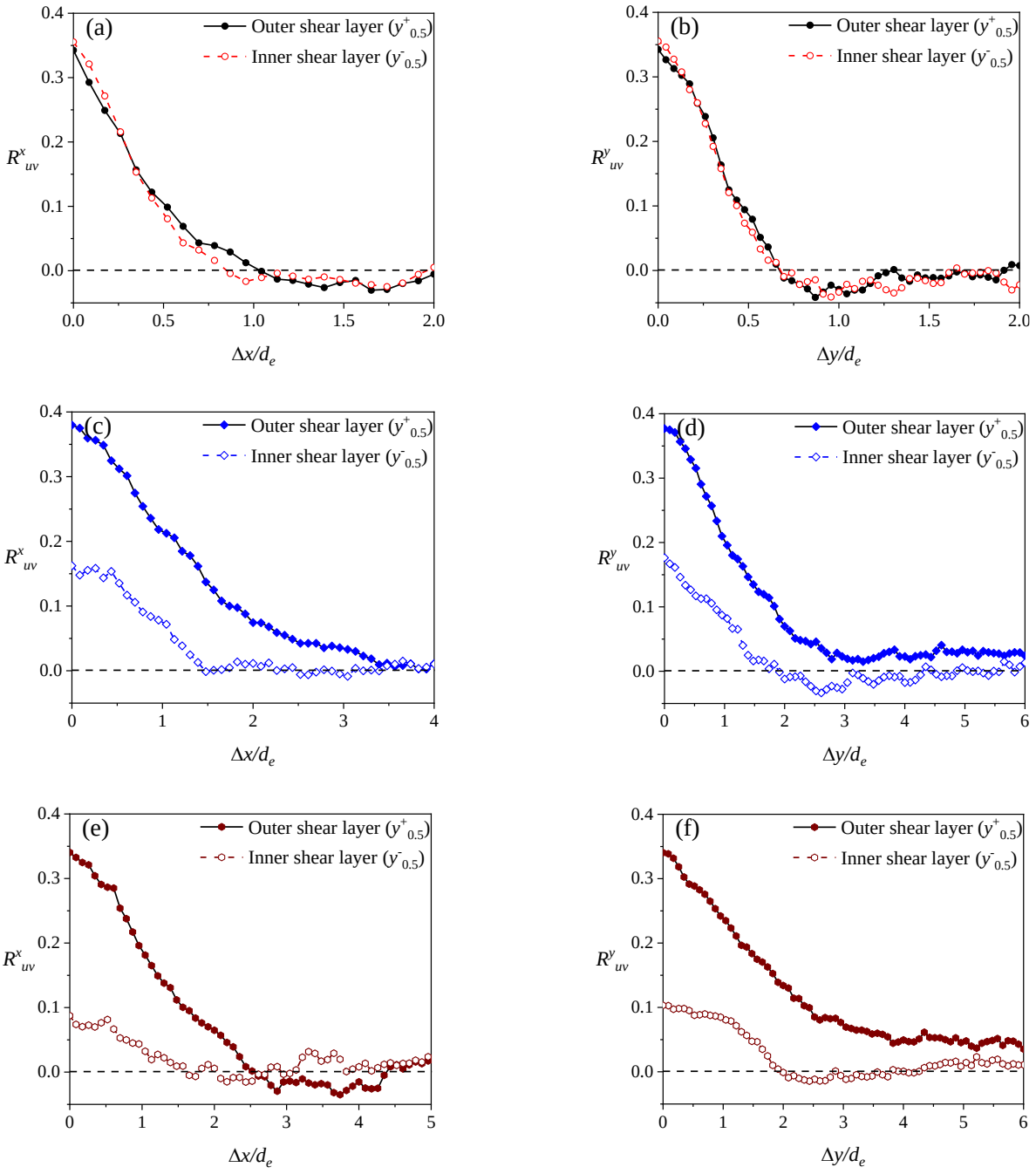

Fig. C-4. Profiles of $R^x_{uv}$and R^y_{uv} at LISHL for (a) and (b), S/d_e = 2.8, (c) and (d), S/d_e = 5.5, and (e) and (f), S/d_e = 7.3.

C.2. JPDF contours for S/d_e = 2.8, 5.5 and 7.3

C.2.1. S/d_e = 2.8

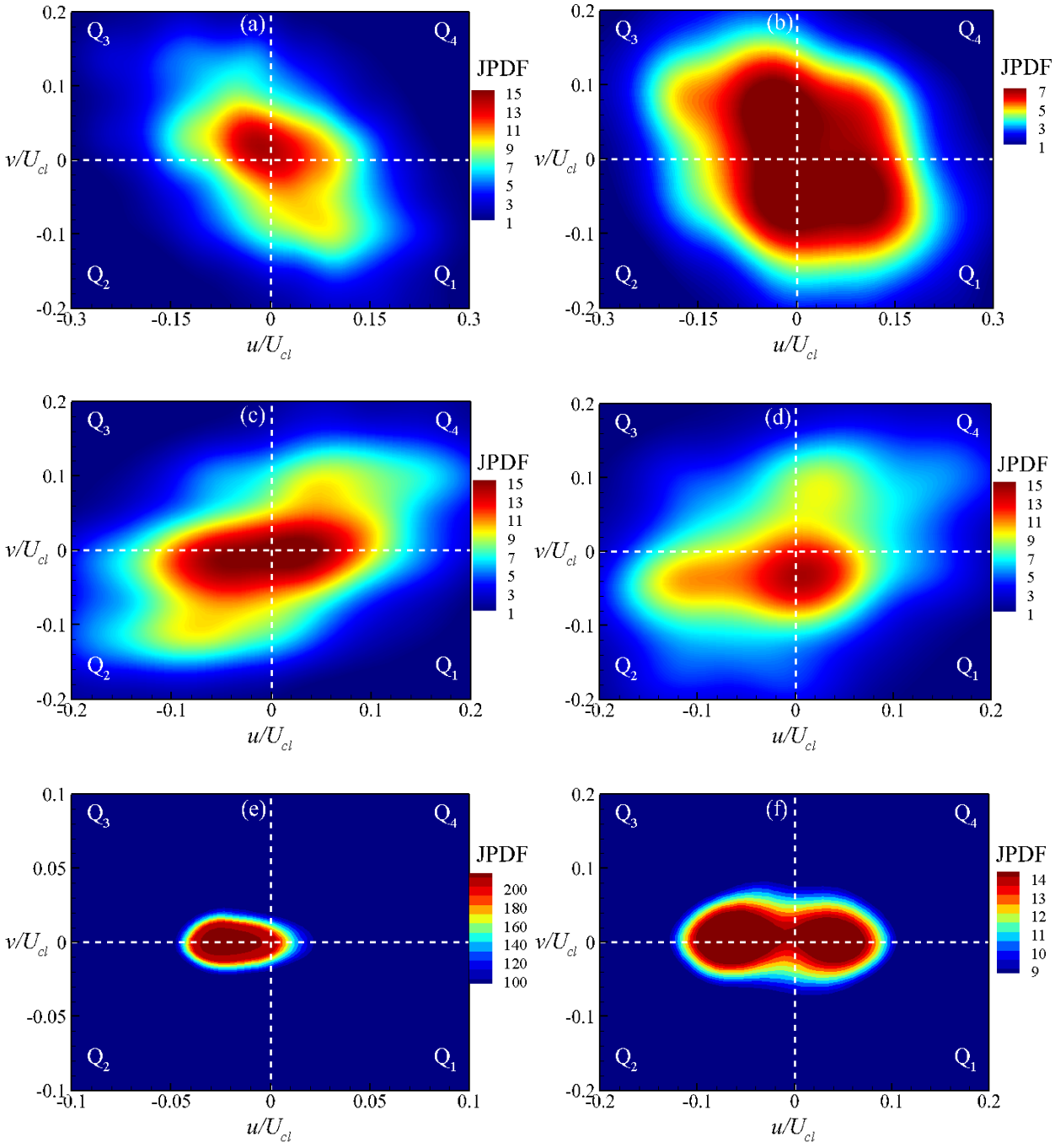

Fig. C-5. (a), (b), (c), JPDF contours at 0.1MP location respectively for outer shear layer, inner shear layer and symmetry line. (b), (d), (f), JPDF contours at LISHL respectively for outer shear layer, inner shear layer and symmetry line.

C.2.2. $S/d_e = 5.5$

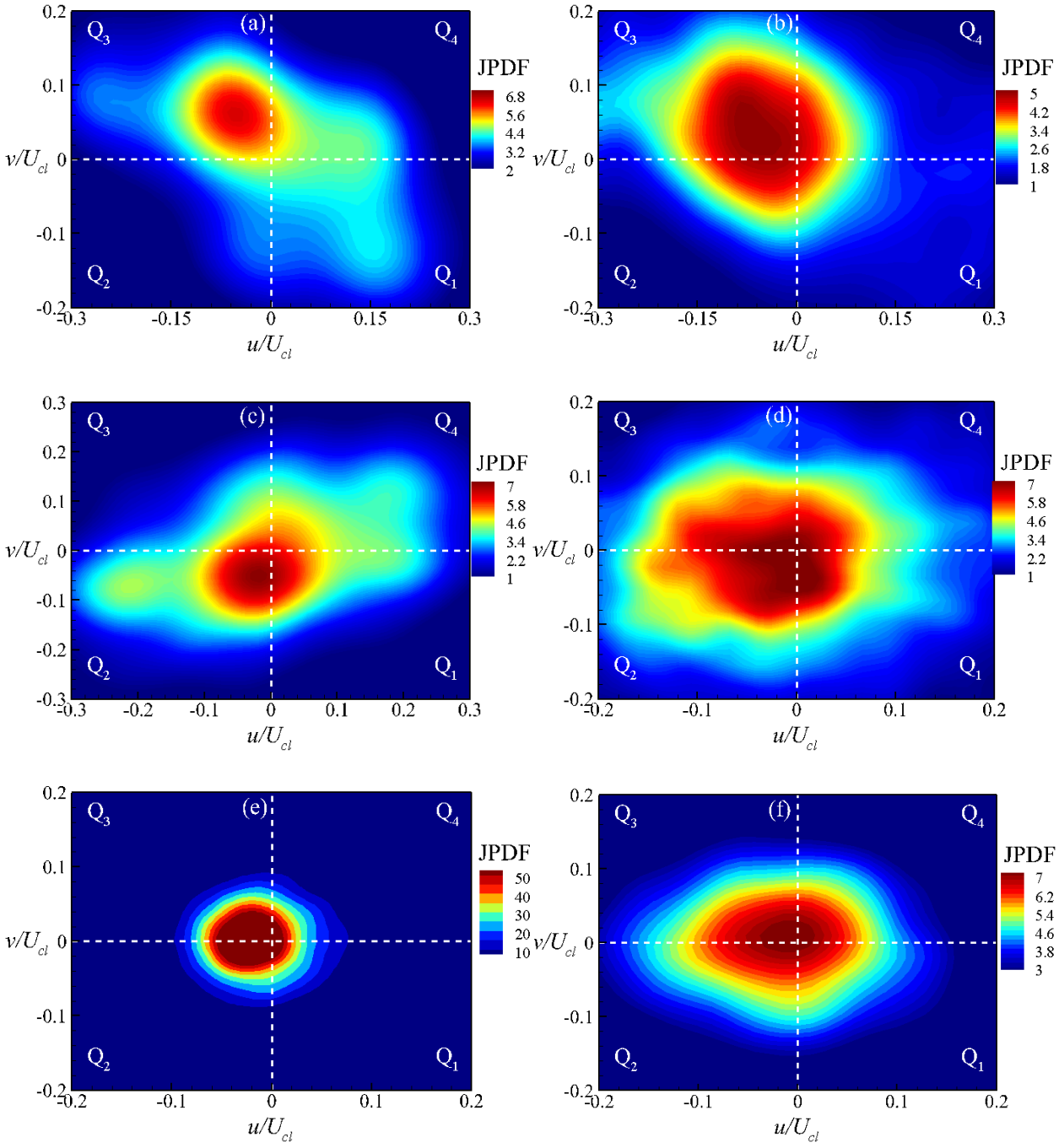

Fig. C-6. (a), (b), (c), JPDF contours at 0.1MP location respectively for outer shear layer, inner shear layer and symmetry line. (b), (d), (f), JPDF contours at LISHL respectively for outer shear layer, inner shear layer and symmetry line.

C.2.3. $S/d_e = 7.3$

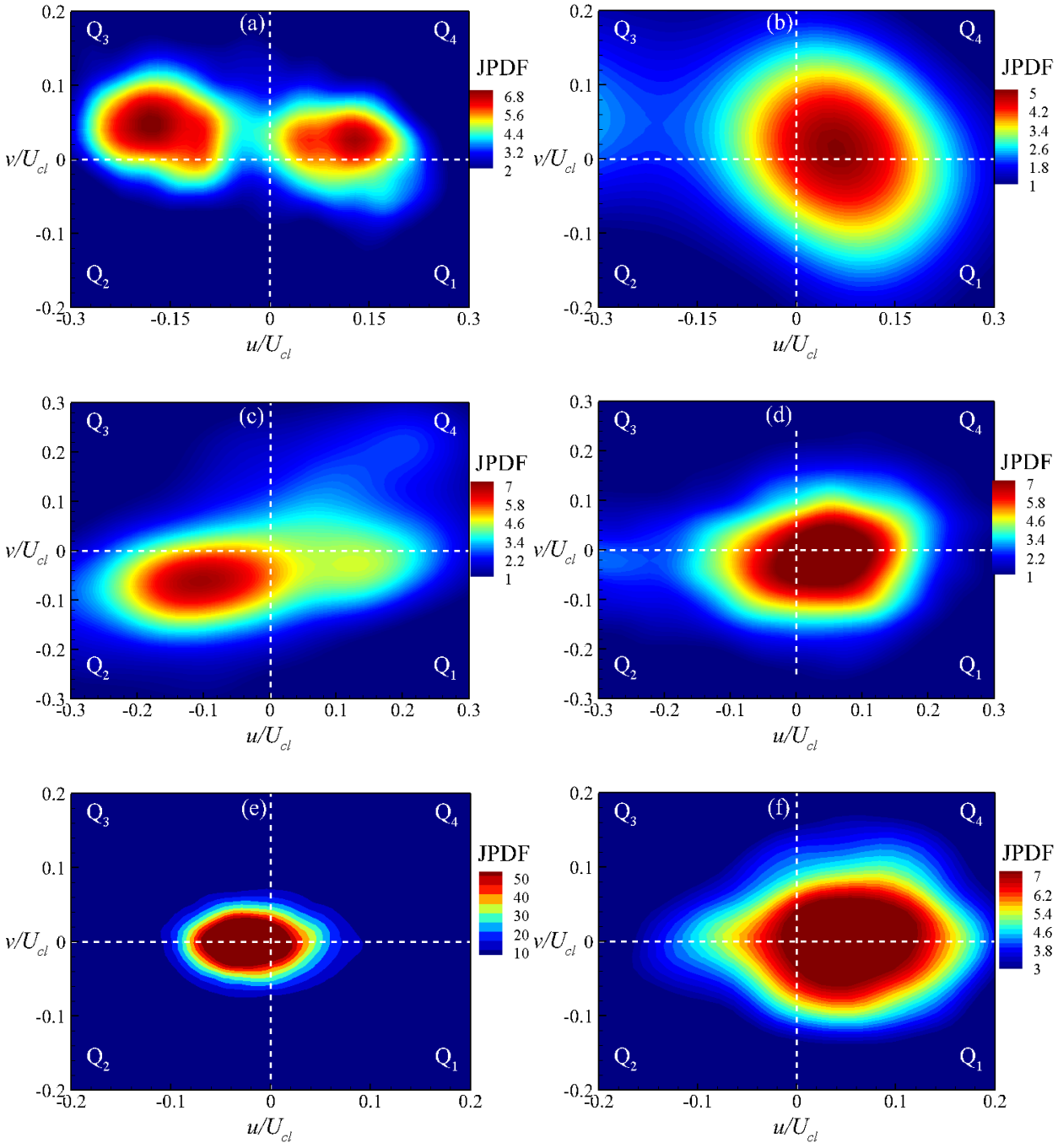

Fig. C-7. (a), (b), (c), JPDF contours at 0.1MP location respectively for outer shear layer, inner shear layer and symmetry line. (b), (d), (f), JPDF contours at LISHL respectively for outer shear layer, inner shear layer and symmetry line.

References

1. Tanaka, E.: The interference of two-dimensional parallel jets (1st report). Bull. JSME. 13, 272–280 (1970)

2. Durve, A., Patwardhan, A.W., Banarjee, I., Padmakumar, G., Vaidyanathan, G.: Numerical investigation of mixing in parallel jets. Nucl. Eng. Des. 242, 78–90 (2012). doi:10.1016/j.nucengdes.2011.10.051

3. Bunderson, N.E., Smith, B.L.: Passive mixing control of plane parallel jets. Exp. Fluids. 39, 66–74 (2005). doi:10.1007/s00348-005-0978-4

4. Miller, D.R., Comings, E.W.: Force-momentum fields in a dual-jet flow. J. Fluid Mech. 7, 237–256 (1960)

5. Okamoto, T., Yagita, M., Watanabe, A., Kawamura, K.: Interaction of twin turbulent circular jet. Bull. JSME. 28, 617–622 (1985). doi:10.1007/s10494-007-9078-2

6. Tanaka, E.: The interference of two-dimensional parallel jets (2nd Report, Experiments on the combined flow of dual jets. Bull. JSME JSME. 17, 920–927 (1974)

7. Anderson, E.A., Snyder, D.O., Christensen, J.: Experimental investigation of periodic behavior between parallel planar jets. AIAA J. (2002)

8. Spall, R.E., Anderson, E.A., Allen, J.: Momentum flux in plane, parallel jets. J. Fluids Eng. 126, 665 (2004). doi:10.1115/1.1778717

9. Hsu, C., Chiang, C., Hsiao, F., Huang, H.: Simulations on the spatial evolution of parallel jets by discrete vortex method. 1–10 (2009)

10. Mondal, T., Das, M.K., Guha, A.: Periodic vortex shedding phenomenon for various

separation distances between two plane turbulent parallel jets. Int. J. Heat Mass Transf. 99, 576–588 (2016). doi:10.1016/j.ijheatmasstransfer.2016.03.095

11. Ko, N.W.M., Lau, K.K.: Flow structures in initial region of two interacting parallel plane jets. Exp. Therm. Fluid Sci. 2, 431–449 (1989). doi:10.1016/0894-1777(89)90006-X

12. Nasr, A., Lai, J.C.S.: Two parallel plane jets: mean flow and effects of acoustic excitation. Exp. Fluids. 22, 251–260 (1997). doi:10.1007/s003480050044

13. Anderson, E.A., Spall, R.E.: Experimental and numerical investigation of two-dimensional parallel jets. J. Fluids Eng. 123, 401 (2001). doi:10.1115/1.1363701

14. Lee, S., Hassan, Y.A.: Experimental study of flow structures near the merging point of two parallel plane jets using PIV and POD. Int. J. Heat Mass Transf. 116, 871–888 (2018). doi:10.1016/j.ijheatmasstransfer.2017.09.047

15. Harima, T., Fujita, S., Osaka, H.: Mixing and diffusion processes of twin circular free jets with various nozzle spacing. In: Proceeding of World Conference on Experimental Heat Transfer, Fluid Mechanics, and Thermodynamics. pp. 1017–1022 (2001)

16. Harima, T., Fujita, S., Osaka, H.: Turbulent properties of twin circular free jets with various nozzle spacing. Eng. Turbul. Model. Exp. 6. 501–510 (2005). doi:10.1016/B978-008044544-1/50048-0

17. Zang, B., New, T.H.: On the wake-like vortical arrangement and behaviour associated with twin jets in close proximity. Exp. Therm. Fluid Sci. 69, 127–140 (2015). doi:10.1016/j.expthermflusci.2015.08.004

18. Maull, D.J., Young, R.A.: Vortex shedding from bluff bodies in a shear flow. J. Fluid Mech.

60, 401–409 (1973)

19. Miller, D. R., Comings, E.W.: Static pressure distribution in the free turbulent jet. J. Fluid Mech. 3, 1–16 (1957)

20. Elbanna, H., Gahin, S., Rashed, M.I.I.: Investigation of two plane parallel jets. AIAA J. 21, 986–991 (1982). doi:10.2514/3.8187

21. Gutmark, E., Wygnanski, I.: The planar turbulent jet. J. Fluid Mech. 73, 465–495 (1976). doi:10.1017/S0022112076001468

22. Lin, Y.E., Sheu, M.J.: Investigation of two plane parallel unventilated jets. Exp. Fluids. 10, 17–22 (1990)

23. Wang, H., Lee, S., Hassan, Y.A.: Particle image velocimetry measurements of the flow in the converging region of two parallel jets. Nucl. Eng. Des. (2015). doi:10.1016/j.nucengdes.2015.09.032

24. Bisoi, M., Das, M.K., Roy, S., Patel, D.K.: Turbulent statistics in flow field due to interaction of two plane parallel jets. Phys. Fluids. 29, (2017). doi:10.1063/1.5018306

25. Aleyasin, S.S., Tachie, M.F., Koupriyanov, M.: PIV measurements in the near and intermediate field regions of jets issuing from eight different nozzle geometries. Flow, Turbul. Combust. 1–23 (2017)

26. Aleyasin, S.S., Fathi, N., Tachie, M.F., Koupriyanov, M.: Comparison of turbulent jets issuing from various sharp contoured nozzles. FEDSM2017. 1–10 (2017)

27. Aleyasin, S.S., Fathi, N., Tachie, M.F., Vorobieff, P., Koupriyanov, M., Limited, P.I.: Experimental-numerical analysis of turbulent incompressible isothermal jets. In: ASME

2017 Fluids Engineering Division Summer Meeting. pp. 1–10 (2017)

28. Prasad, A.K.: Particle image velocimetry. Curr. Sci. 79, 51–60 (2000). doi:10.1007/978-3-540-72308-0

29. Mei, R., Adrian, R.J., Hanratty, T.J.: Particle dispersion in isotropic turbulence under Stokes drag and Basset force with gravitational settling. J. Fluid Mech. 225, 481--495 (1991)

30. Raffel, M., Willert, C.: Particle image velocimetry: A practical guide. Springer-Verlag. 7, 4 (1996)

31. Mi, J., Nathan, G.J.: Statistical properties of turbulent free jets issuing from nine differently-shaped nozzles. Flow, Turbul. Combust. 84, 583–606 (2010). doi:10.1007/s10494-009-9240-0

32. Hussain, F., Husain, H.S.: Elliptic jets. Part 1. Characteristics of unexcited and excited jets. J. Fluid Mech. 208, 257–320 (1989)

33. Gutmark, E., Ho, C.-M.: Visualization of a forced elliptic jet. AIAA J. 24, 684–685 (1986)

34. Quinn, W.R.: Measurements in the near flow field of an isosceles triangular turbulent free jet. Exp. Fluids. 39, 111–126 (2005). doi:10.1007/s00348-005-0988-2

35. Becker, H., Massaro, T.: Vortex evolution in a round jet. J. Fluid Mech. 31, 435–448 (1968)

36. Aleyasin, S.S., Tachie, M.F.: Statistical properties and structural analysis of three-dimensional twin round jets due to variation in Reynolds number. Int. J. Heat Fluid Flow. 76, 215–230 (2019). doi:10.1016/j.ijheatfluidflow.2018.12.001

37. Tay, G.F.K., Mishra, A., Kuhn, D.C.S., Tachie, M.F.: Free surface effects on the statistical properties of a submerged rectangular jet. Phys. Fluids. 025101, (2017).

doi:10.1063/1.4975155

38. Oskouie, R.N., Tachie, M.F., Wang, B.-C.: Effect of nozzle spacing on turbulent interaction of low-aspect-ratio twin rectangular jets. Flow, Turbul. Combust. 1--22 (2019)

39. Laban, A., Aleyasin, S.S., Tachie, M.F., Koupriyanov, M.: Experimental investigation of nozzle spacing effects on characteristics of round twin free jets. J. Fluids Eng. 141, (2018)

40. Aleyasin, S.S., Tachie, M.F., Koupriyanov, M.: Statistical properties of round , square and elliptic jets at low and moderate Reynolds numbers. J. Fluids Eng. 139, 1–41 (2017)

41. Zhou, J., Adrian, R.J., Balachandar, S., Kendall, T.: Mechanisms for generating coherent packets of hairpin vortices in channel flow. J. Fluid Mech. 387, 353–396 (1999)

42. Hutchins, N., Hambleton, W., Marusic, I.: Inclined cross-stream stereo particle image velocimetry measurements in turbulent boundary layers. J. Fluid Mech. 541, 21–54 (2005)

43. Tay, G.F., Kuhn, D.C., Tachie, M.F.: Surface roughness effects on the turbulence statistics in a low reynolds number channel flow. J. Turbul. 14, 121–146 (2013)

44. Bisset, D.K., Hunt, J.C., Rogers, M.M.: The turbulent/non-turbulent interface bounding a far wake. J. Fluid Mech. 451, 383--410 (2002)

45. Anand, R.K., Boersma, B.J., Agrawal, A.: Detection of turbulent/non-turbulent interface for an axisymmetric turbulent jet: Evaluation of known criteria and proposal of a new criterion. Exp. Fluids. 47, 995–1007 (2009). doi:10.1007/s00348-009-0695-5

46. Westerweel, J., Hofmann, T., Fukushima, C., Hunt, J.C.R.: The turbulent / non-turbulent interface at the outer boundary of a self-similar turbulent jet. 33, 873–878 (2002). doi:10.1007/s00348-002-0489-5

47. Westerweel, J., Fukushima, C., Pedersen, J.M., Hunt, J.C.R.: Momentum and scalar transport at the turbulent/non-turbulent interface of a jet. J. Fluid Mech. 631, 199–230 (2009). doi:10.1017/S0022112009006600

48. Ooi, M.K.A., Marusic, J.S.I.: Evolution of the turbulent / non-turbulent interface of an axisymmetric turbulent jet. (2013). doi:10.1007/s00348-012-1449-3

49. Ghasemi, A., Roussinova, V., Balachandar, R., Barron, R.M.: Reynolds number effects in the near-field of a turbulent square jet. Exp. Therm. Fluid Sci. 61, 249–258 (2015). doi:10.1016/j.expthermflusci.2014.10.025

50. Casarsa, L., Giannattasio, P.: Three-dimensional features of the turbulent flow through a planar sudden expansion. Phys. Fluids. 20, (2008). doi:10.1063/1.2832780